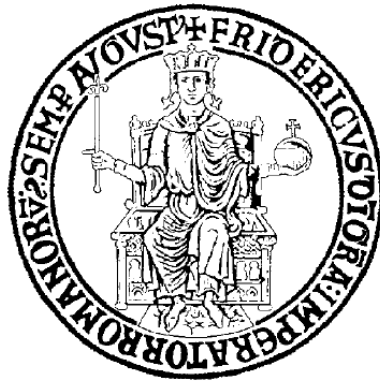


UNIVERSITA' DEGLI STUDI DI NAPOLI  
FEDERICO II



DEPARTMENT OF PHYSICS  
PHD IN FUNDAMENTAL AND APPLIED PHYSICS  
XXVI CYCLE

FIBER OPTICAL SENSORS  
FOR HIGH ENERGY PHYSICS

MARCO ESPOSITO

TUTORS

DR. SALVATORE BUONTEMPO

DR. MICHELE GIORDANO

MARCH 2014



## **ACKNOWLEDGEMENTS**

*A special Thanks to my Tutors, Salvatore e Michele for their support during these years  
and to the Coordinator of the PhD Courses, Prof. R. Velotta.*

*The author is also grateful to the Institute for Composite and Biomedical Materials, CNR IMCB,  
to the OptoSmart Team, to the CMS People Group,  
to the National Institute of Nuclear Physics, INFN NA,  
to the European Organization for Nuclear Research, CERN.*

---

# TABLE OF CONTENTS

TABLE OF CONTENTS.....	4
ABSTRACT.....	6
CHAPTER 1.....	8
INTRODUCTION TO THE OPTICAL FIBER SENSOR TECHNOLOGY FOR HIGH ENERGY PHYSICS APPLICATIONS.....	8
1.1. The Large Hadron Collider At CERN.....	8
1.2. The Compact Moun Solenoid (CMS) Experiment.....	16
1.2.1. CMS Detector Layout.....	18
1.2.2. The Tracker System.....	20
1.2.3. The Superconducting Solenoid Magnet.....	23
1.2.4. The Electromagnetic Calorimeter.....	24
1.2.5. The Hadronic Calorimeter.....	27
1.2.6. The Muon System.....	29
1.2.7. Drift Tubes.....	30
1.2.8. Cathode Strip Chambers.....	31
1.2.9. Resistive Plate chambers.....	31
1.3. Fiber Optical Sensors For High Energy Physics.....	32
1.4. Overview Of The Existing Fiber Optical Sensors (FOS) In CMS.....	35
1.4.1. Temperature FOS Installations in CMS.....	35
1.4.2. Strain FOS Installations in CMS.....	36
CHAPTER 2.....	39
FBG OPTICAL ANALYSIS.....	39
2.1. FBG Working Principle.....	39
2.2. Maxwell Equations For An Optical Dielectric Medium.....	41
2.2.1. Modulation Of The Refractive Index.....	44
2.2.2. Solution For The Transverse Component Of The Field.....	45
2.3. Amplitude Equations Of The Progressive And Back Travelling Waves.....	47
2.4. Solution For The Progressive And Back Travelling Wave Amplitudes.....	51
2.5. Reflectivity And Transmissivity Coefficients Of The Grating.....	53
2.5.1. Numerical Evaluation Of The Reflectivity For Different Gratings.....	57
CHAPTER 3.....	65
ACTIVE COATED FBG MECHANICAL ANALYSIS.....	65
3.1. Fiber Bragg Grating Wavelength Shift.....	65
3.2. Mechanical Behavior Of The Active Coated FBG.....	68
3.3. Constitutive Equation Of The Materials.....	72
3.4. Boundary Conditions.....	74
3.5. Stress Function.....	75
3.5.1. Factorization Of The Stress Function.....	79
3.5.2. Radial Solution.....	79
3.5.3. Stress Components.....	85
3.6. Determination of the Constants in the Stress Components.....	89
3.6.1. Fourier Series Expansion.....	92
3.6.2. Algebraic Solving System.....	95

## 5 TABLE OF CONTENTS

---

CHAPTER 4 .....	97
FIBER OPTICAL SENSORS FOR CRYOGENIC TEMPERATURE MONITORING IN LHC .....	97
4.1. Motivations.....	97
4.2. Design Choice Of The Active Coated FBG Thickness .....	99
4.2.1. Active Coated FBG Cryogenic Sensors Sensitivity.....	103
4.3. Samples Preparation.....	105
4.3.1. Coating Materials .....	106
4.3.2. Coating Methods.....	106
4.4. Experimental Set Up For Cryogenic Temperature Measurements At Cern .....	108
4.5. Experimental Results.....	109
4.6. Evaluation Of The Thermal Expansion Coefficient .....	113
4.6.1. Methodology.....	113
4.6.2. Correlated Fluctuation Analysis (CFA).....	115
4.7. Results And Discussion .....	116
4.8. Conclusions.....	120
CHAPTER 5 .....	123
FIBER OPTICAL RELATIVE HUMIDITY SENSORS FOR HIGH ENERGY PHYSICS APPLICATIONS.....	123
5.1. Motivations.....	123
5.2. Humidity Definition.....	124
5.3. Humidity Sensors Based On Optical Fiber Technology .....	126
5.4. Relative Humidity Sensors Based On Polyimide Coated FBG .....	127
5.5. Bragg Wavelength Shift Due To Relative Humidity Changes.....	129
5.5.1. Sensor Sensitivities .....	132
5.6. Mass Transport Phenomena .....	135
5.7. Radiation Hardness Capability Of The PI Coated FBG RH Sensors .....	137
5.7.1. Irradiation Tests On The Temperature FBG Sensors.....	139
5.7.2. Irradiation Tests On The PI Coated RH FBG Sensors.....	140
5.8. Preliminary Study On Epoxy Coated Relative Humidity FBG Sensors .....	141
5.8.1. Hygrothermal Properties Of Epoxy.....	141
5.8.2. Coating Method .....	142
5.8.3. Epoxy Coated FBG Sensitivity.....	143
5.9. Conclusions.....	144
CONCLUSIONS.....	146
BIBLIOGRAPHY.....	149

---

## ABSTRACT

High Energy Physics Experiments carried out at the Large Hadron Collider (LHC) of the European Organization for Nuclear Research (CERN) at Geneva, require manufacturing and operation of very complex devices, which demand solutions and challenging synergies to very complex and problematic conditions. These devices operating at CERN need an effective monitoring system to prevent damages which can be caused by many different factors, such as: very high or very low temperature, high magnetic fields and induced mechanical strain, irradiation, electromagnetic interferences, humidity and so on. Traditional sensing systems based on electronic sensor several time present serious drawbacks in such harsh environmental conditions, in particular for the presence of very intense electromagnetic fields generating high noise levels. Moreover the concomitant presence of very high level of irradiation imposes the Radiation Hardness Capability as one fundamental requirement for the sensors to be employed. Fiber Bragg Grating (FBG) optical sensors offer an immediate solution for all these issues: in particular their immunity to electromagnetic noise factor make them clearly preferable with respect to the traditional electronic sensors for High Energy Physics (HEP) applications. Compactness, intrinsic multiplexing (also many tens of sensors can be mounted on the a single optical fiber), long term stable and reliable behavior, multi-parameter sensitivity (commercial sensors detect Mechanical Strain and Temperature, prototypes presented in present thesis detect relative humidity and cryogenic temperatures), reduction of instrumentation and improvement of the workplace safety are further fundamental advantages of the FBGs to be taken in consideration in the future design choices for sensing network in the LHC accelerator and detectors.

In present thesis, the suitability of Active Coated FBG sensors for Cryogenic Temperature monitoring in the LHC infrastructures and for Relative Humidity measures in the Compact Muon Solenoid (CMS) experiment at CERN is demonstrated. Moreover the main results of a mathematical model specifically developed to manufacture and to analyze the Active Coated FBG mechanical behavior by correlating the FBG wavelength shift with the external forcing factors, will be presented. The obtained results have been published on an

---

## 7 ABSTRACT

---

international peer reviewed journal. Additional results on the relative humidity measurements are being published by the end of this year.

---

# **CHAPTER 1**

## **INTRODUCTION TO THE OPTICAL FIBER SENSOR TECHNOLOGY FOR HIGH ENERGY PHYSICS APPLICATIONS**

### **1.1. THE LARGE HADRON COLLIDER AT CERN**

The European Organization for Nuclear Research, CERN, was founded in 1954 and it's located near Geneva at the state border between France and Switzerland. At present it's the world's leading laboratory for particle physics. It was one of Europe's first joint ventures and now has 20 Member States. The LHC accelerator at CERN is one of the largest machine and the most powerful particle accelerator in the world. It's main objective is to discover the real nature of the whole matter and energy contained in the universe, such as dark matter and the dark energy.

---

In July 2012 the Large Hadron Collider has achieved its first major milestone: the existence of the Higgs Boson, the particle whose field allows all particles to have mass, and in the future it could deserve further relevant discoveries like the long researched Super Symmetric particles, as predicted by the Supersymmetric physical theory and perhaps the existence of further dimensions invisible to us, rolled up on themselves, over the 3 spatial we well-know, as predicted by some theoretical physical theories such as the String Theory.

The Large Hadron Collider, Figure 1, is constituted by a 27 km length circular ring at 100 m depth underground, constituted by two separate beam pipes with a very high vacuum level inside, where counter rotating beams of protons or heavy ions are accelerated almost to the speed of light and kept on the curved path by superconducting magnets, designed to allow particle collisions at the order of TeV energy scale.

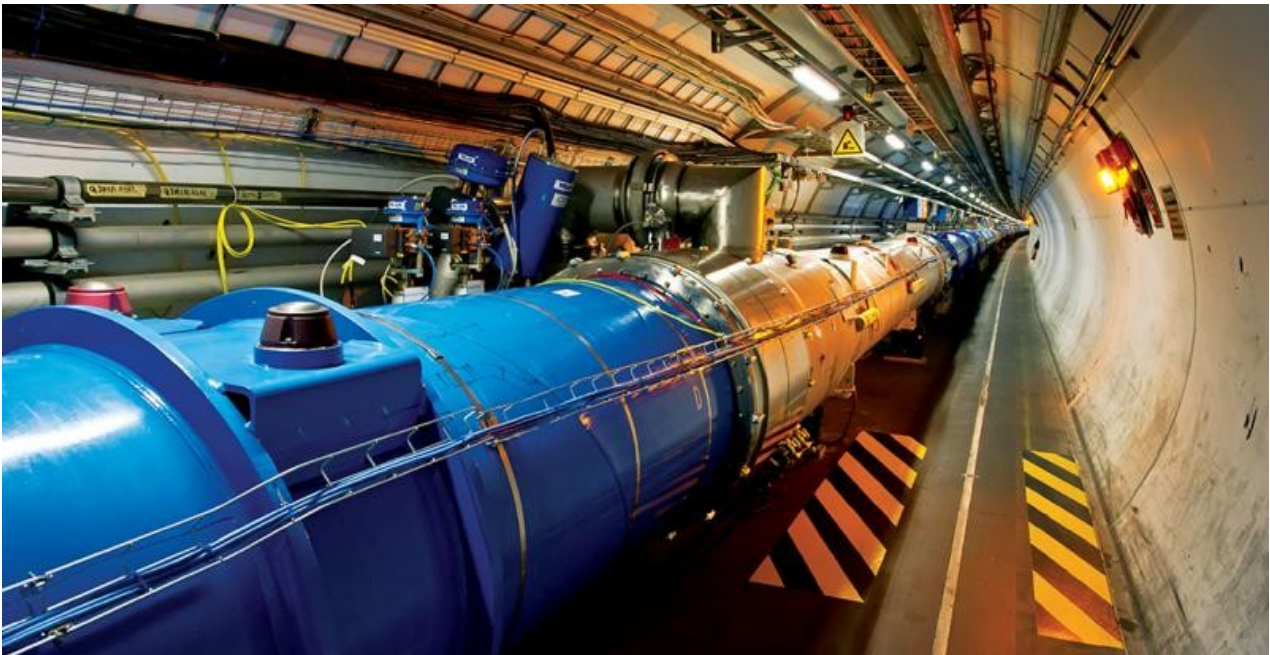


*Figure 1 –The Large Hadron Collider (Source: CERN [2])*

In LHC particles are accelerated through Radiofrequency (RF) cavities in which an oscillating electromagnetic field is generated. For this purpose, RF cavities are constituted by metallic chambers having a shape designed to induce resonance at specific frequencies: in LHC each RF cavity is tuned to oscillate at

---

400 MHz. After protons have reached target level of energy, if they are exactly in phase with the oscillating field, they won't be accelerated when they pass through the chambers. Conversely, protons with slightly different energies or whose arrival time in the RF Cavity are not exactly in phase with the field, being for example in delay or in advance, will be respectively accelerated or decelerated. For this reason, in LHC particles don't constitute a continuous stream, but they are spaced in bunches (up to 2808 in parallel)..

In LHC there are 16 RF cavities. Each cavity can achieve a maximum voltage of 2 MV, making 16 MV per beam. They are placed in four cylindrical refrigerators called cryomodules, which keep the RF cavities working in a superconducting state, without losing energy to electrical resistance.

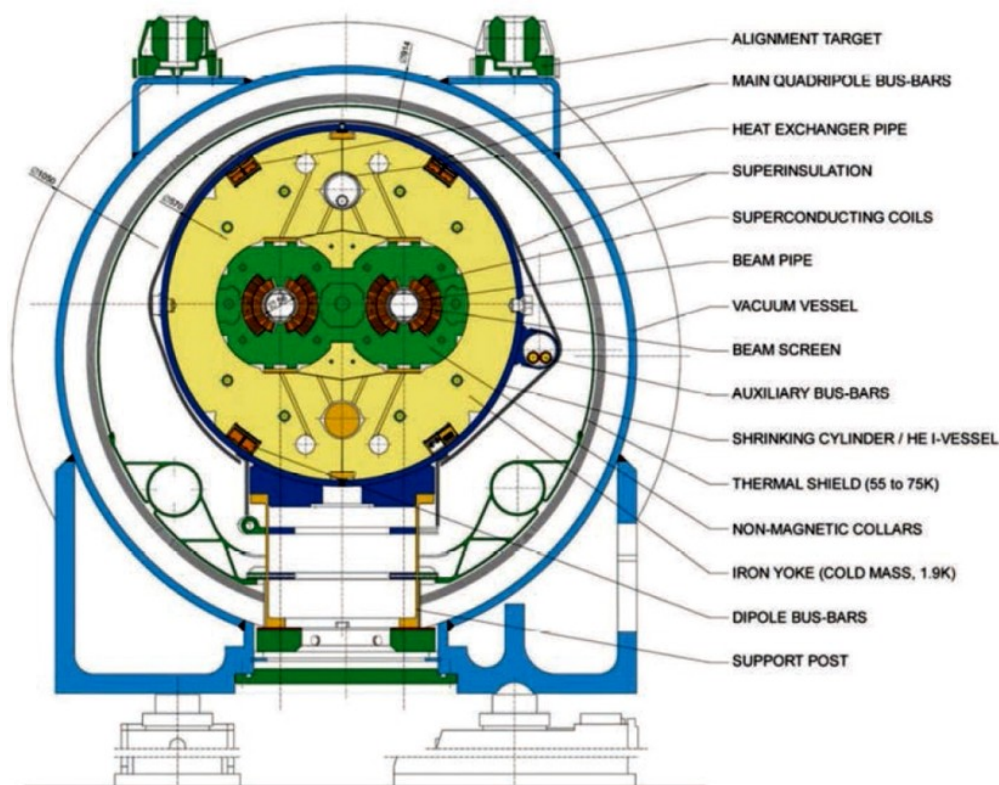


*Figure 2 – Structure of the LHC dipole magnets [3]*

The beams are directed around the accelerator by different kinds of magnets: in LHC are employed 1232 dipole magnets of 15 m length, (see Figure 2), to bend the beams and more than 392 quadrupole magnets 5–7 m long, (see Figure 3), for focusing the beams and increase the probability of collisions.

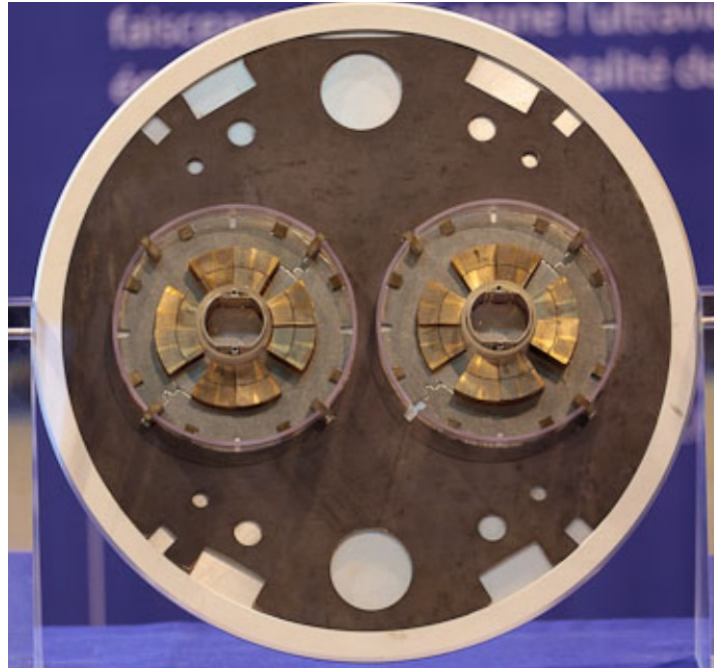


*Figure 3 – Cross section of the LHC quadrupole magnets in LHC*

As for the RF cavities, magnets used in the Large Hadron Collider need extreme cooling conditions to preserve the internal superconductivity highly crucial for their performances. The magnets coils, built with NbTi based superconductors, are cooled through a distribution system of Liquid Helium (superfluid) which allows them to reach an operative temperature of 1.9 K, about  $-271.3^{\circ}\text{C}$ . At these Temperatures, current can be conducted almost without resistance (superconducting state) at about 12000A in NbTi, generating the intense needed magnetic field, which can reach a value of 8 Telsa, about 150 thousand times the magnetic field on the earth surface. To maintain efficiently the magnets at these cryogenic temperatures, an high lever of the vacuum as a thermal insulator is needed: indeed the vacuum allows to reduce very significantly the quantity of heat coming from the surrounding environment at room-temperature into the cryogenic parts at 1.9 K and to spend a lower amount of energy to keep the cryomagnets cold. In the cryomagnets insulating system, the vacuum level is equivalent to  $10^{-6}$  mbar; with a total of 104 kilometers of piping under vacuum and with an impressive array of vacuum technologies employed, the LHC operational vacuum system and it is among the largest and complex in the world [2]. The insulating vacuum system is made by 50 km of

---

pipings, with a combined volume of over 15 000 cubic meters. The remaining 54 km of pipes under vacuum are instead needed for the beam pipes, through which the LHC's two beams travel. The pressure in these pipes is drastically lower, in the order of  $10^{-10}$  to  $10^{-11}$  mbar ( $10^{-13}$  atmospheres), a vacuum more rarefied than the interplanetary void. Ultra-high vacuum in the pipes includes 48 km of arc sections, kept at 1.9 K, and 6 km of straight sections, where beam-control systems and the colliding regions for the experiments are located, kept instead at room temperature. LHC is also one of the most hot place in the galaxy: indeed the beam interaction points where collisions take place reaches a temperature 100,000 times higher than that of the heart of the Sun. In LHC collisions results are observed and recorded by large size instruments called detectors. At present the main research activity at CERN is in the recording of events generated by proton-proton collisions or proton-target collisions in four main interaction points where detectors are placed: ATLAS (A Toroidal Lhc ApparatuS), ALICE(A Large Ion Collider Experiment), CMS (Compact Muon Solenoid) and LHCb (LHC-beauty).

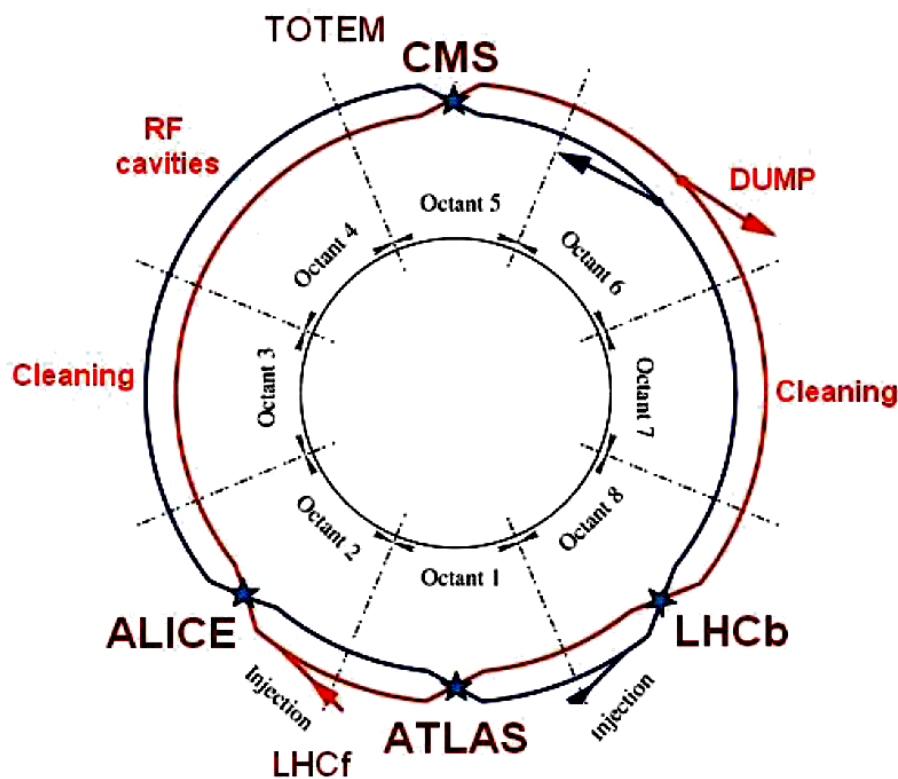


Figure 4 - The LHC beam structure [4]

Figure 4 shows a schematic view of the LHC accelerator and main detectors. The Figure 5 shows the scheme of the LHC beam acceleration complex evidencing the chain to accelerate proton up to the LHC injection energy of 450 GeV. A series of accelerators work together to push particles up to speeds very close to the to light one. The accelerator complex at CERN is a succession of machines that accelerate particles to increasingly higher energies. It consists in a chain in which each machine boosts the energy of a beam of particles before injecting the beam into the next one in the sequence [2][4]. The proton source is a simple of hydrogen gas container. The protons are produced at 92 keV through an electric field used to strip hydrogen atoms of their electrons; the protons are then introduced in the Linear Accelerator (LINAC2); the LINAC2, the first accelerator in the chain, accelerates the protons to the energy of 50 MeV. Protons are then injected into the Proton Synchrotron Booster (PSB), where they reach 1.4 GeV; subsequently protons are accelerated up to 25 GeV through the Proton Synchrotron (PS) coming out packed in bunches separated by 25 nanoseconds each. Protons are then sent to the Super Proton Synchrotron (SPS) where they are accelerated up to the LHC injection energy of 450 GeV and transferred to the two beam pipes of the LHC.

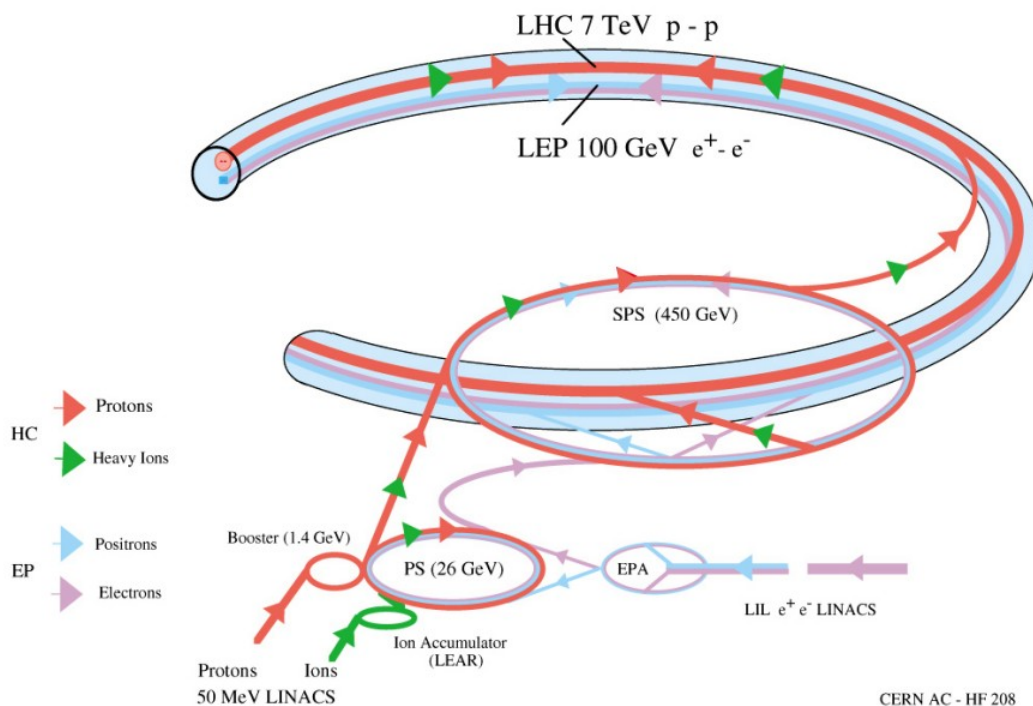


Figure 5 – Schematic view of the LHC accelerator complex [4]

Finally the LHC accelerates the particle bunches up to the energy required for physics (7TeV for each beam, allowing the energy of 14 TeV by design in the interaction points). The protons are bunched together into 2808 bunches, 115 billion protons in each bunch, so that interactions between the two beams will take place at discrete intervals never shorter than 25 nanoseconds (ns) [7].

As well known from the Einstein Special Relativity Theory, the particle Energy is given by:

$$E = \gamma m_0 c^2 \tag{Eq. 1}$$

Where  $m_0$  is the invariant particle mass, viewed in the center of momentum particle reference system (in which it appears rest), while  $\gamma$  is the Lorentz factor:

$$\gamma = \frac{1}{\sqrt{1 - \beta^2}} = \cosh \varphi \quad \beta = \frac{v}{c} \tag{Eq. 2}$$

with  $\beta$  relative speed factor. The  $\varphi$  parameter is defined as rapidity. The Table 1 summarizes the energies of a proton particle after each acceleration stage and the corresponding  $\gamma$  and  $\beta$  values.

<i>Accelerator</i>	<i>Energy</i>	<i>Lorentz Factor <math>\gamma</math></i>	<i><math>\beta</math></i>
<i>LINAC2</i>	<i>50 MeV</i>	<i>1.05</i>	<i>0.31409151</i>
<i>Proton Synchrotron Booster</i>	<i>1.4 GeV</i>	<i>2.49</i>	<i>0.91599153</i>
<i>Proton Synchrotron</i>	<i>25 GeV</i>	<i>27.65</i>	<i>0.99934590</i>
<i>Super Proton Synchrotron</i>	<i>450 GeV</i>	<i>480.74</i>	<i>0.99999784</i>
<i>LHC</i>	<i>7000 GeV</i>	<i>7463.69</i>	<i>0.99999999</i>

*Table 1- Energy, Lorentz factor  $\gamma$  and relative speed factor  $\beta$  after each acceleration stage for a proton*

The accelerator complex also includes the Antiproton Decelerator and the Online Isotope Mass Separator (ISOLDE) facility, and feeds the CERN Neutrinos to Gran Sasso (CNGS) project and the Compact Linear Collider test area, as well as the neutron time-of-flight facility (nTOF). Protons are not the only particles accelerated in the LHC. Lead ions for the LHC start from a source of vaporized lead and enter Linac 3 before

---

being collected and accelerated in the Low Energy Ion Ring (LEIR) [2]. They then follow the same route to maximum energy as the protons. The CERN Control Centre combines control rooms for the laboratory's accelerators, the cryogenic distribution system and the technical infrastructure. It holds 39 operation stations for four different areas – the LHC, the SPS, the PS complex and the technical infrastructure [2].

The main parameters of interest for physics at the LHC are the center of mass energy and the instantaneous luminosity  $L(t)$ . The luminosity relates the cross section  $\sigma$  of a given process with the number of events  $N$  generated in the collisions per time unit:

$$\frac{dN}{dt} = L(t)\sigma \quad \text{Eq. 3}$$

The design luminosity for ATLAS and CMS experiments is  $L = 10^{-34} \text{ cm}^{-2}$ . Conversely, the other two experiments located at the interaction points of LHC, ALICE and LHCb, have a lower design instantaneous luminosity, namely  $L = 10^{-32} \text{ cm}^{-2}$  for LHCb and  $L = 10^{-29} \text{ cm}^{-2}$  for ALICE [4]. It is noteworthy that the CMS and ATLAS luminosity is the highest ever achieved counting pre-LHC hadron colliding machines.

The CMS and ATLAS design luminosity corresponds roughly to  $15\text{pb}^{-1}$  of luminosity per hour, and  $100\text{fb}^{-1}$  (inverse femtobarn) per year – approximately 1000 trillion proton–proton collisions at 14TeV energy counting approximately an effective operating time of the machine of 250 days with 12 hours of data capturing.

In conclusion LHC is a surprising record machine: it's the largest in the world with a structure 27 km long, weighing 38,000 tons. LHC is the coolest place in the interstellar space but also the hottest spot of the galaxy. Much of this machine is kept at a temperature of  $-271.3 \text{ }^\circ\text{C}$  while the points where collisions take place reach a peak temperature 100,000 times higher than that of the heart of the Sun. Once the maximum energy will be reached the protons in the LHC will travel at a speed only  $1 \cdot 10^{-6} \%$  lower than the speed of light; at that speed each proton carries 11000 full turns of the ring every second and the proton beams will cross each other 40 million times per second with a number of collisions in the system up to 40 proton-

---

proton collisions every 25 nanoseconds or about 1 billion collisions per second; finally LHC is also the largest factory in the world of information: each year, the data produced by the LHC experiments produce the equivalent of one hundred thousand DVDs.

## **1.2. THE COMPACT MUON SOLENOID (CMS) EXPERIMENT**

The Compact Muon Solenoid experiment, Figure 6, is one of the four main experiments at the LHC. It's a general-purpose experiment, since its research program includes most of the physics at the LHC, from the Standard Model measurements to the Higgs and new physics researches.

The name CMS derives from the superconducting compact solenoid which generates an internal magnetic field of 3.8 Tesla needed for both the internal and the external to solenoid detectors. The internal to solenoid detector system is composed by Tracker, Electromagnetic Calorimeter (ECAL) and Hadronic Calorimeter (HCAL). The external to solenoid detector system is constituted by the Muon System: it's composed by Drift Tubes, Cathode Strip Chambers and Resistive Plate Chambers. Together they ensure excellent muon triggering and identification.

---

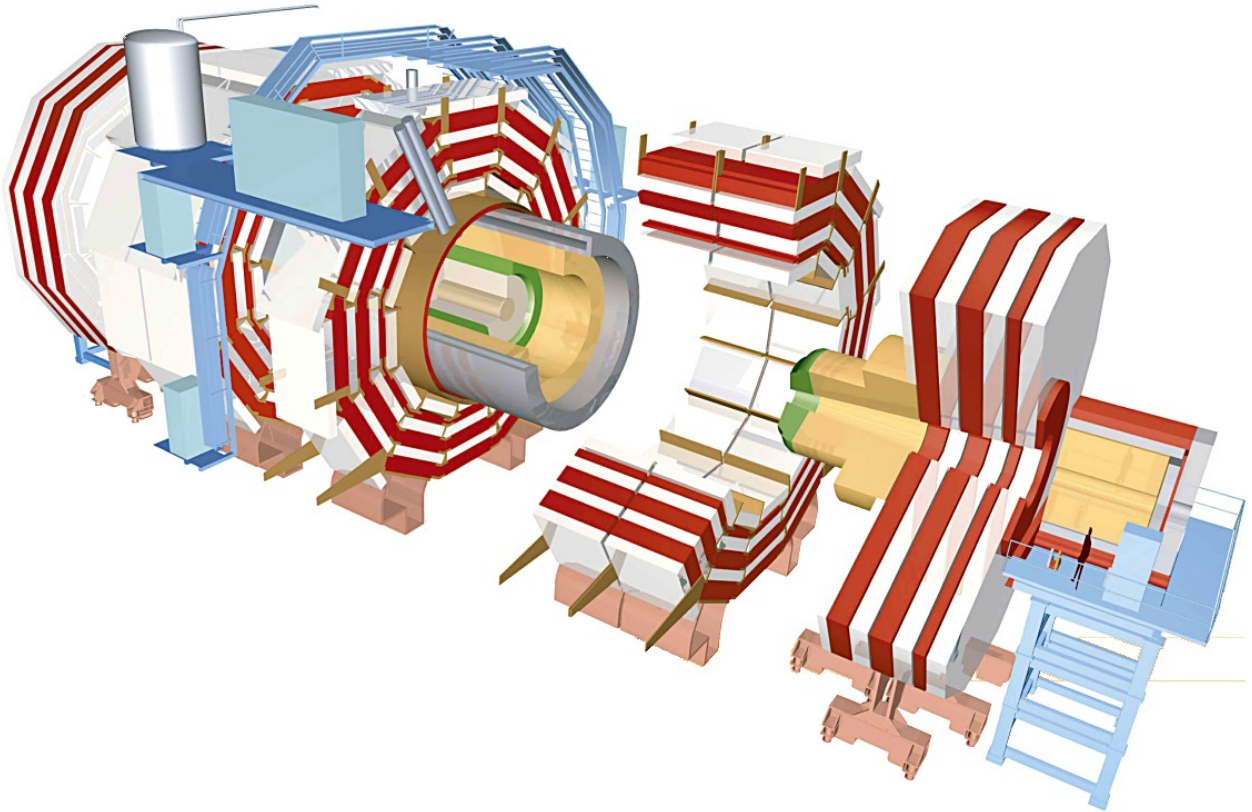


*Figure 6 – The Compact Muon Solenoid Experiment [9]*

The total proton-proton cross-section at  $\sqrt{s} = 14$  TeV is expected to be roughly 100 mb. At design luminosity the general-purpose detectors will therefore observe an event rate of approximately  $10^9$  inelastic events/s. As described in [4], this leads to a series of unprecedented experimental challenges that any detector at LHC has to deal with. They are:

- Rate reduction - The huge event rate has to face physical limitations in the bandwidth at which data can be transferred to the storage facilities: a manageable event rate that can be passed to the storage and subsequent analysis is about 100 events/s, meaning that a reduction of order  $10^7$  has to be operated by the selection process (trigger). The bunch crossing interval of 25 ns implies that it is not possible to transfer this to any offline software to perform such reduction, therefore it has to be performed online with electronics triggering systems. The bunch crossing timing is therefore crucial to design the CMS triggering system.

---

- Pile up events - At the design luminosity, a mean up to 40 inelastic collisions will be superimposed on the event of interest. This implies that around 1000 charged particles will emerge from the interaction region every 25 ns. The products of an interaction under study may be confused with those from other interactions in the same bunch crossing. This problem clearly becomes more severe when the response time of a detector element and its electronic signal is longer than 25 ns. The effect of this pile-up can be reduced by using high-granularity detectors with good time resolution, resulting in low occupancy. This requires a large number of detector channels. The resulting millions of detector electronic channels require very good synchronization.
- Radiation robustness - The high rates have the important consequence that detectors have to sustain a severe amount of radiation, and have to maintain good performances over the course of several years of data taking. This problem affects especially detectors which are closer to the interaction point (any system aiming to measure the vertex at interaction point or the tracks) and the ones at lower angles with respect to the beam pipe.

### **1.2.1. CMS DETECTOR LAYOUT**

The CMS detector, Figure 7, has cylindrical symmetry with respect to the beam axis. It is constituted by several layers of detectors centered on the interaction point. Each detector is divided in a central barrel region and two endcaps covering the extreme regions along the beam direction. Starting from the most internal position toward the most external one, the CMS detector is composed by:

- The Pixel detector: silicon pixel detector used for accurate measurement of the vertex.
  - The Silicon Strip Tracker: a silicon strip detector, which is used for accurate track reconstruction.
  - The Electromagnetic Calorimeter (ECAL): an homogeneous lead tungstate electromagnetic calorimeter, for accurate electron and photon energy measurement which also contributes to measure the electromagnetic fraction of jets energy.
-

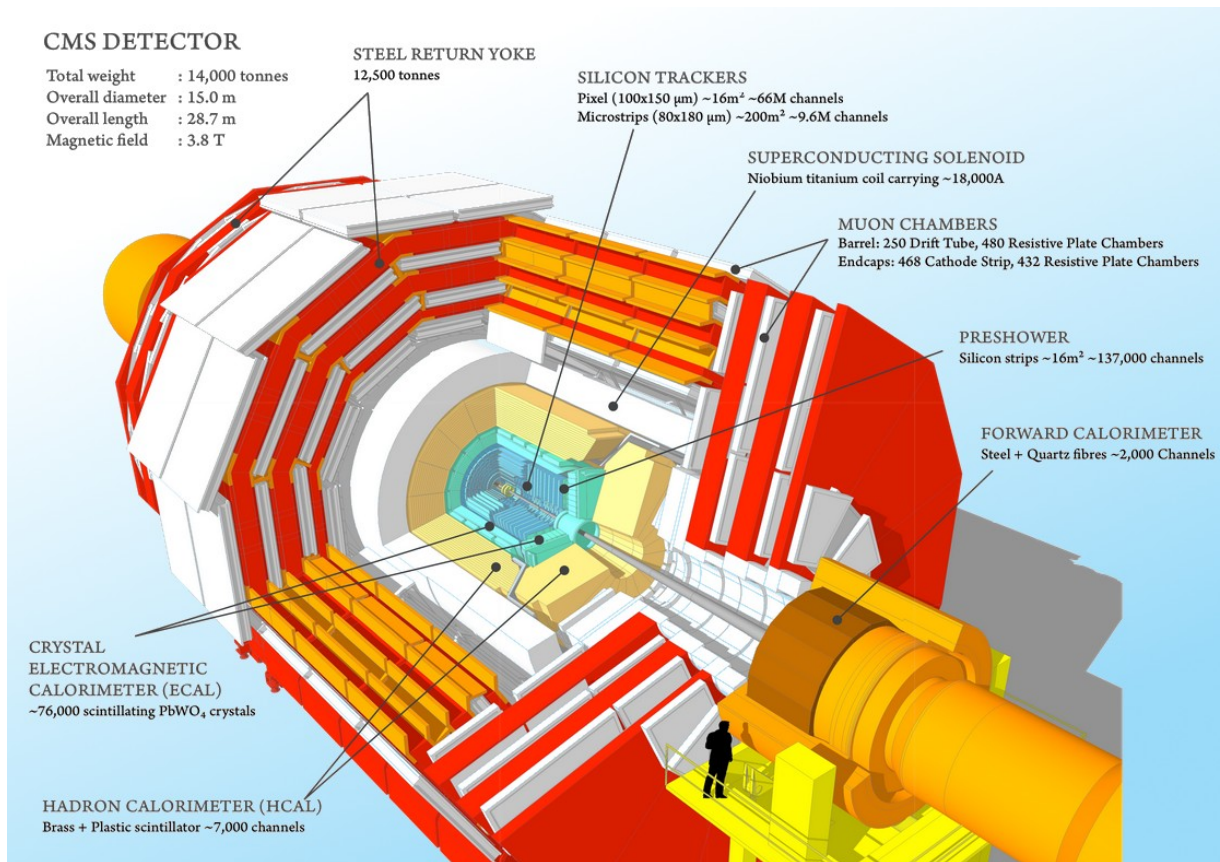


Figure 7 – CMS Detector Layout[9]

- The Hadronic Calorimeter (HCAL): a sampling calorimeter with brass and plastic scintillators for energy measurements of jets.
- The Superconducting Solenoid: the coil generating an internal constant magnetic field of 3.8 Tesla in the direction of the beam axis.
- The Muon system: constituted of gas detectors for muon identification and triggering: Drift Tube detectors and Resistive Plate Chambers in the barrel region, Cathode Strip Chambers and Resistive Plate Chambers in the endcap region.
- The return yoke: interlaced with the Muon System is the return yoke to sustain the structure and studied so to allow magnetic field lines of the solenoid
- The Forward Hadron Calorimeter: a Cherenkov-Based calorimeter for the very forward region covering.

CMS detector is designed to detect a wide range of particles and phenomena produced in high-energy collisions in the LHC. As shown in Figure 8, different layers of detectors stop different kind of particles and measure their energy and momentum, and use this to reconstruct the collision event at the center of the detector.

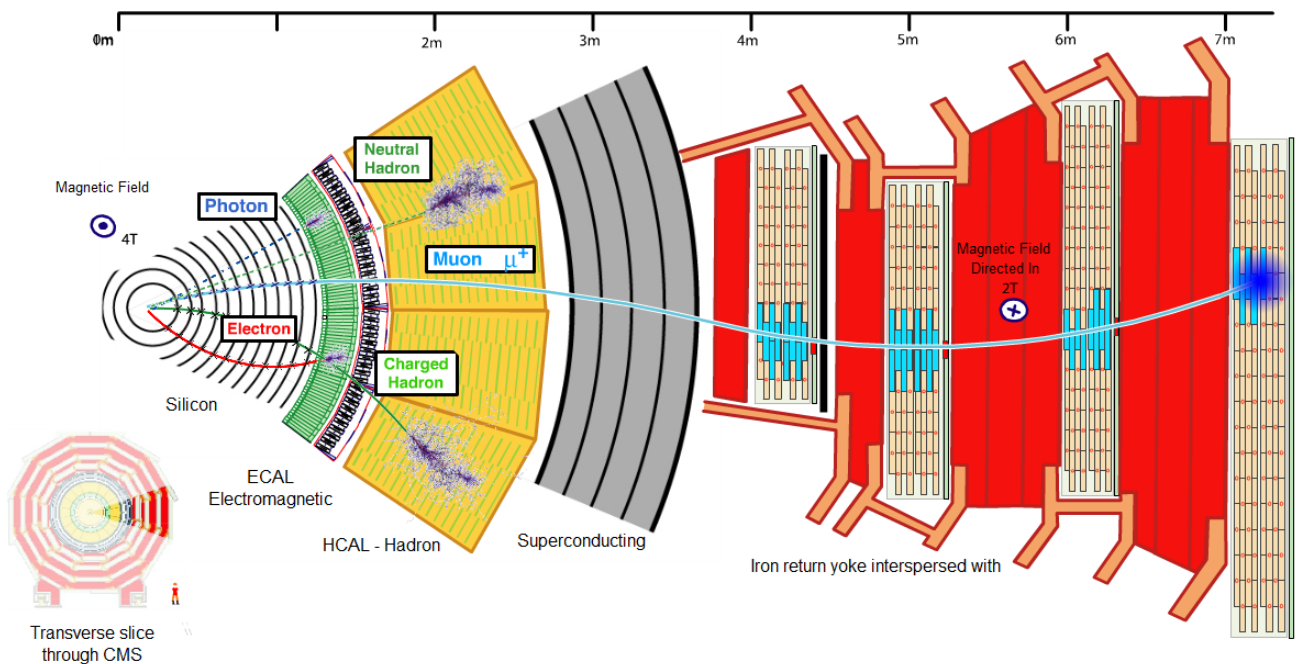
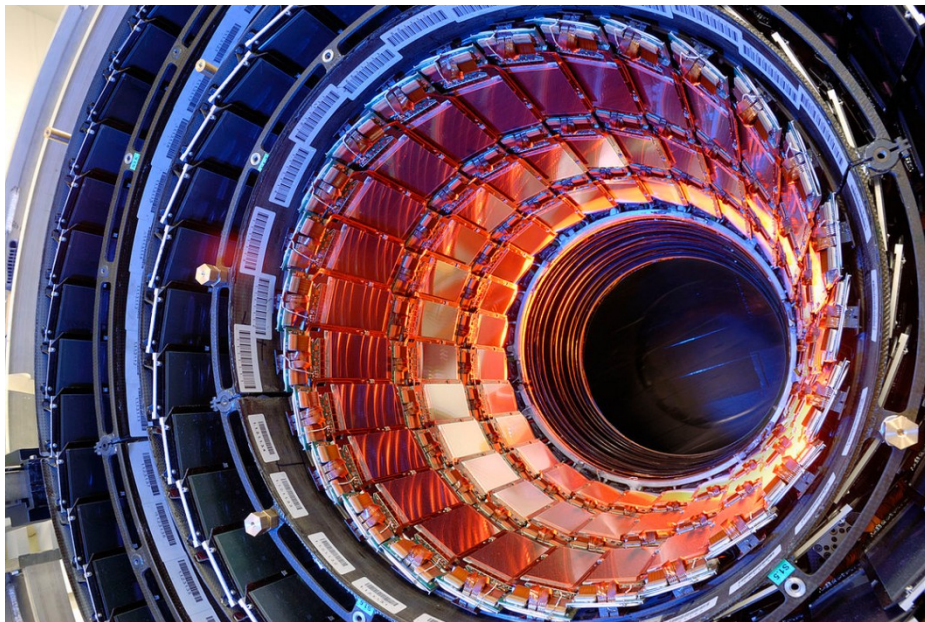


Figure 8 – Different particles detection in CMS [9]

### 1.2.2. THE TRACKER SYSTEM

Momentum of particles is crucial to reconstruct the events around the collision point. The momentum of the particles moving through the magnetic field of 3.8 Tesla generated by the CMS solenoid can be easily calculated from the observed curvature of the charged particle paths, with a weakly curved path indicating an high particle momentum. The precise reconstruction of the particle paths is carried out by finding their angular positions as function of the distance from the center. The tracker can reconstruct the paths of high-energy muons, electrons and hadrons as well as see tracks coming from the decay of very short-lived particles such as beauty or b quarks that will be used to study the differences between matter and antimatter.



*Figure 9 – The silicon strips detectors in the CMS Tracker before being assembled [9]*

The tracker is designed to disturb the particles as less as it's possible, by reconstructing their paths using a few measurement points with a very high spatial resolution, lower than  $15\ \mu\text{m}$ . As particles travel through the tracker the pixels and microstrips produce tiny electric signals that are detected and amplified. The tracker employs 75 million separate electronic read-out channels with more than 6000 connections per square centimeter. Being the most inner layer of the detector the materials are carefully chosen to resist to the very high level of radiation.

About 1000 particles are crossing the tracker region each 25 ns. This impressive particle rate sets the requirements for the tracking system [4]:

- High granularity in order to discriminate even adjacent trajectories and make ambiguities easily removable at reconstruction level.
  - Fast response time, in order to deal with the high bunch crossings frequencies.
  - Radiation robustness: the intense particle flux causes damage to the detectors over time, so it was crucial to design a tracking system which could operate under LHC conditions and remain efficient over the entire CMS lifetime (at least 3 run periods of data taking, each 3 year long).
-

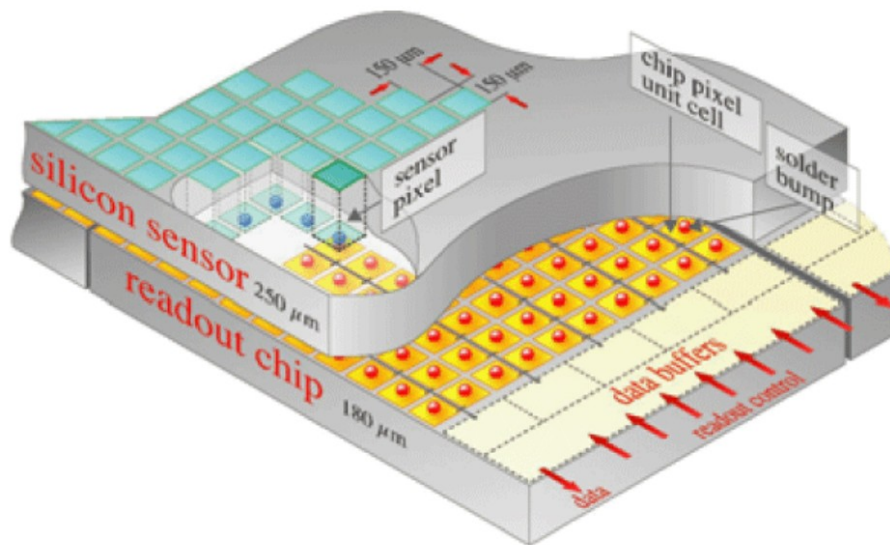


Figure 10 – The Silicon Pixel detector in the CMS Tracker System[9]

The CMS inner tracking system is made by a pixel detector for the inner region and a silicon strip tracker for the outer region. The pixel detector Figure 10, contains 65 million pixels, divided through the two pixel endcaps disks (FPix) orthogonal to the beam axis with 18 million pixels on a surface of  $0.28 \text{ m}^2$  and the barrel layer (BPix) containing 48 million pixels on  $0.78 \text{ m}^2$ . They allow to track the paths of particles with extreme accuracy. Being the closest detector to the beam pipe, with the three cylindrical layers (BPix) of hybrid pixel detectors at radii of 4.4, 7.3 and 10.2 cm from the beam, it plays a crucial role in reconstructing the tracks of particles with very short live after collision. For the same reason the rate of particles received at 8cm from the beam axis is higher than  $10 \text{ million/cm}^2\text{s}$ , and since there are 65 million channels, even if each tile generates less than around 50 microwatts, the pixels are mounted on cooling tubes to avoid damage for heating. Each layer of the detector is split into several little silicon sensors,  $150\mu\text{m}$  by  $150\mu\text{m}$ : when a charged particle passes through it allows electrons to be ejected from the silicon atoms, creating electron-hole pairs, so that an electric current can collect these charges on the surface as a small electric signal, amplified by a silicon chip.

After the pixels detectors, particles encounter ten layers of silicon strip detectors having an extension of 130 centimeters radius. The silicon strip detector consist of 4 barrel layers (TIB) and two endcaps (TID), each

composed of three small discs. In the TIB/TID zone the strips are 320  $\mu\text{m}$  thick, and the strip pitch is 80  $\mu\text{m}$  on layers 1 and 2 and 120  $\mu\text{m}$  on layers 3 and 4 in the TIB, resulting in a single point resolution of 23  $\mu\text{m}$  and 35  $\mu\text{m}$ , respectively. In the TID the mean pitch varies between 100  $\mu\text{m}$  and 141  $\mu\text{m}$ . The outer barrel (TOB) consists of six concentric layers with strips 500  $\mu\text{m}$  thick. Finally two endcaps (TEC) close off the tracker. Each TEC consists of 9 disks, carrying up to 7 rings of silicon micro-strip detectors (320  $\mu\text{m}$  thick on the inner 4 rings, 500  $\mu\text{m}$  thick on rings 5-7) with radial strips of 97  $\mu\text{m}$  to 184  $\mu\text{m}$  average pitch. The silicon strip detectors in the tracker contains 15,200 highly sensitive modules with a total of 10 million detector strips read by 80,000 microelectronic chips.

Silicon sensors have fast response and good spatial resolution. The working principle of the silicon detectors is the same on which the pixels are based: when a charged particle passes through the material, it knocks electron from atoms and within the applied electric field, these produce a very small pulse of current lasting a few nanoseconds. The tracker and its electronics are designed to resist to radiation, and for this purpose they are kept at  $-20^{\circ}\text{C}$ , to avoid any damage could perpetuate.

The charge on each microstrip is read out and amplified by an Analogue Pipeline Voltage (APV25) chip, housed with electronics needed to provide timing information to match hits with collisions. The APV25 processes the signals before sending them to a laser where they are converted into infrared pulses and subsequently transmitted over a 100m fiber optical cable for analysis in a radiation-free environment. The tracker uses 40,000 fiber optical links providing a low power lightweight signal transmission. The LHC bunch crossing at design luminosity results in a hit rate density of 1 MHz/  $\text{mm}^2$  at a radius of 4 cm, 60 kHz/ $\text{mm}^2$  at a radius of 22 cm and 3 kHz/ $\text{mm}^2$  at a radius of 115 cm.

### **1.2.3. THE SUPERCONDUCTING SOLENOID MAGNET**

The solenoid is a coil of superconducting wire that creates a 4T magnetic field. In CMS the solenoid has an overall length of 13m and a diameter of 7m. It is the largest magnet of its type ever constructed and it allows

---

the tracker and calorimeter detectors to be placed inside the coil, resulting in a detector that is, overall, compact, compared to detectors of similar weight.

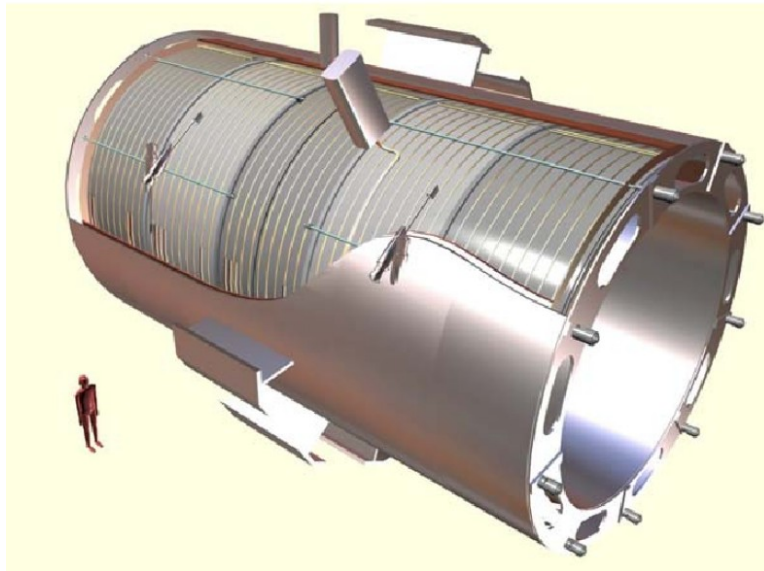


*Figure 11 – CAD reconstruction of the CMS solenoid [4]*

The CMS superconducting magnet for CMS has been designed to generate a 4-Tesla field in a free bore of 6-m diameter and 12.5-m length with a stored energy of 2.6 GJ at full current. The return yoke returns the flux so that the field lines close outside the magnet and the magnetic field is intense and constant enough to ensure momentum measurement of particles in the outer CMS Muon System. The return yokes consists of iron, weights 10 000-tons and it comprises 5 wheels and 6 disks divided in the two endcaps. The magnet was fully and successfully tested and commissioned in the hall above CMS (SX5) during autumn 2006 before being laid down in the experimental cavern [4].

#### **1.2.4. THE ELECTROMAGNETIC CALORIMETER**

Electrons and photons are detected in CMS using the electromagnetic calorimeter (ECAL, see Figure 12). It's composed mainly by Lead tungstate ( $\text{PbWO}_4$ ) which is a well known scintillating material. It presents a density of  $8.3 \text{ g/cm}^3$  and the oxygen in this structure makes its crystals highly transparent, as the Figure 13

---

clearly shows. Scintillation of this mineral occurs since, due to the particle irradiation, excited electrons of the atoms first reach an higher energy level, and then return on their own lower energy level by emitting photons and producing therefore light in proportion to impinging the particle energy. The produced scintillation light results in photons of well-defined wavelength: in the ECAL photons are received by photodetectors for conversion in electrical signal, to be subsequently amplified and sent for analysis.

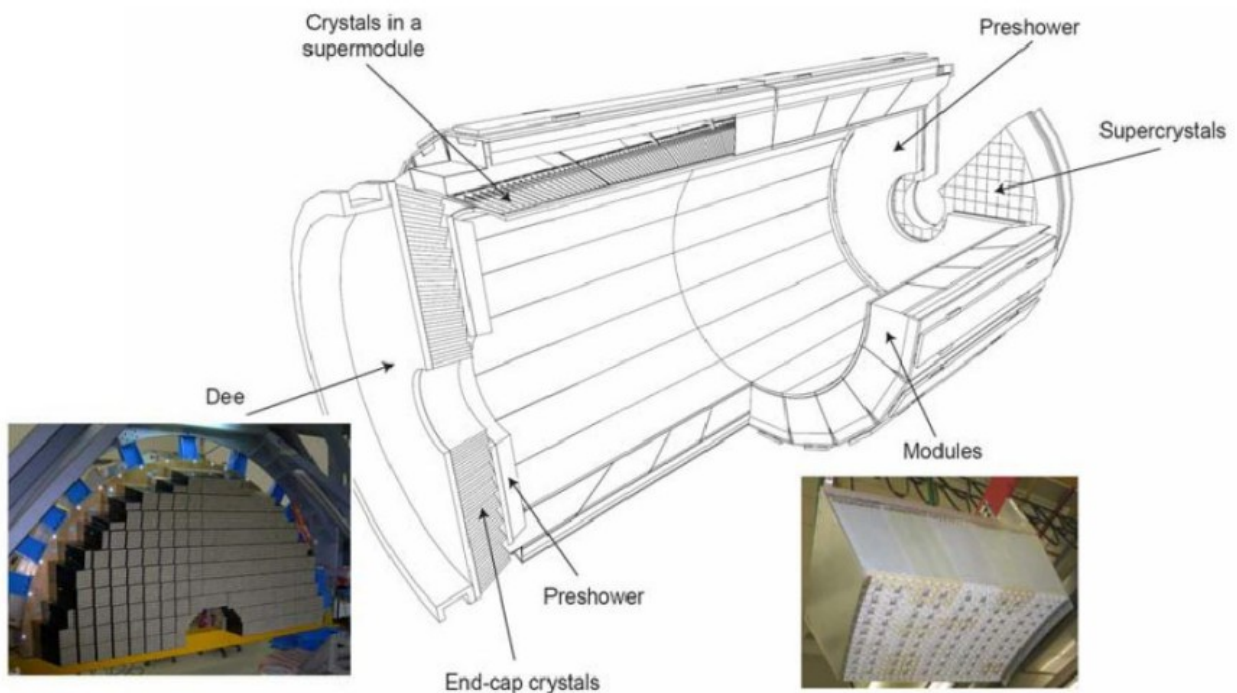


*Figure 12 – The CMS Electromagnetic Calorimeter[4]*

The ECAL is made up of a barrel section and two endcaps to form a layer between the tracker and the HCAL. The cylindrical barrel consists of 61,200 crystals formed into 36 supermodules, containing about 1700 crystals. The flat ECAL endcaps are made up of almost 15,000 further crystals. Since the yield of light depends strongly on temperature, the whole crystal volume is maintained within  $0.1^{\circ}\text{C}$ . For extra spatial precision, the ECAL also contains Preshower detectors placed in front of the endcaps. Groups of crystals were then assembled side-by-side in glass-fibre or carbon-fibre pockets to form larger structures known as supercrystals, modules and supermodules.

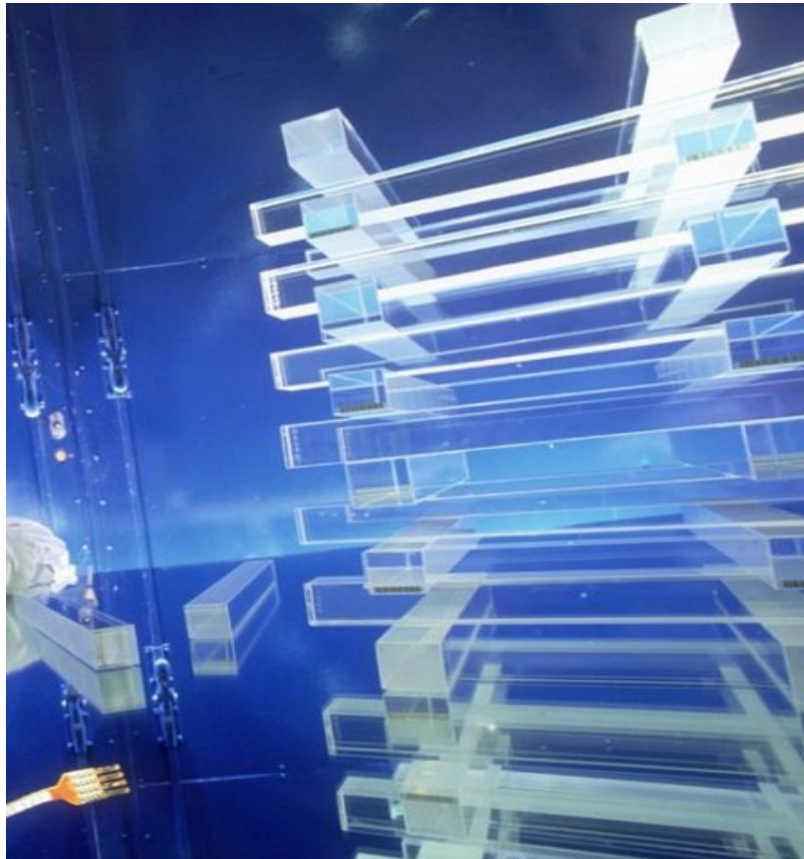


*Figure 13 – Lead Tungstate ( $PbWO_4$ ) Crystals used in the ECAL of CMS [9]*

The employed photodetectors operate within a strong magnetic field and since they are subjected to a very high radiation level, they must be necessarily radiation hard; for the ECAL barrel, Avalanche Photodiodes (APDs) are employed while for the ECAL endcaps vacuum phototriodes (VPTs) have been installed.

Avalanche Photodiodes (APDs) are Photodiodes in semiconducting silicon with a strong electric field applied to them. When a scintillation photon hit an electron out of an atom, the electron is accelerated in the electric field, acquiring enough kinetic energy to cause further knocking of other bound electrons, which reach the conduction band and then generate an avalanche of electrons. APDs produce a very high current in a short time, fundamental feature since lead tungstate crystals provide a relatively low emission light for each incident particle

---

In the endcaps regions, since the radiation is too high to use silicon photodiodes, vacuum phototriodes (VPTs) are employed for the crystals. A VPT is a Photomultiplier (PMT) with a single dynode. In fact the VPT contains three electrodes within a vacuum: a photocathode, a single dynode and the anode. When incident photons strike the photocathode material, electrons are emitted as a consequence of the photoelectric effect. These electrons are then directed by the focusing electrode toward the dynode, where electrons are multiplied by the process of secondary emission. Finally they are collected by the anode. A large current is therefore created from the initial tiny amount of scintillation light. The current is then transformed into a digital signal and sent for the next readout level.

### **1.2.5. THE HADRONIC CALORIMETER**

The Hadron Calorimeter (HCAL, Figure 14) is designed to study a wide range of high-energy processes, resulting in a variety of final state topology involving hadronic jets, neutrinos or also exotic particles manifesting through missing energy in the transverse plane. Indeed, as these particles decay, they may produce new particles that do not leave record of their presence in any part of the CMS detector. It is therefore crucial to have a precise measurement of jets energy and ensure the detector is hermetic in order to reduce the uncertainty on transverse energy lost.

The HCAL is a sampling calorimeter: it finds the particle's position, energy and arrival time using alternating layers of absorber and fluorescent scintillating materials by producing a rapid light pulse when the particle passes through. Optical fibers collect up this light and feed it into readout boxes where photodetectors amplify the signal.

The HCAL present a large radial extension of about one meter in order to detect and measure the cascades of particles produced when an hadron hits its dense absorber material, called showers.

---

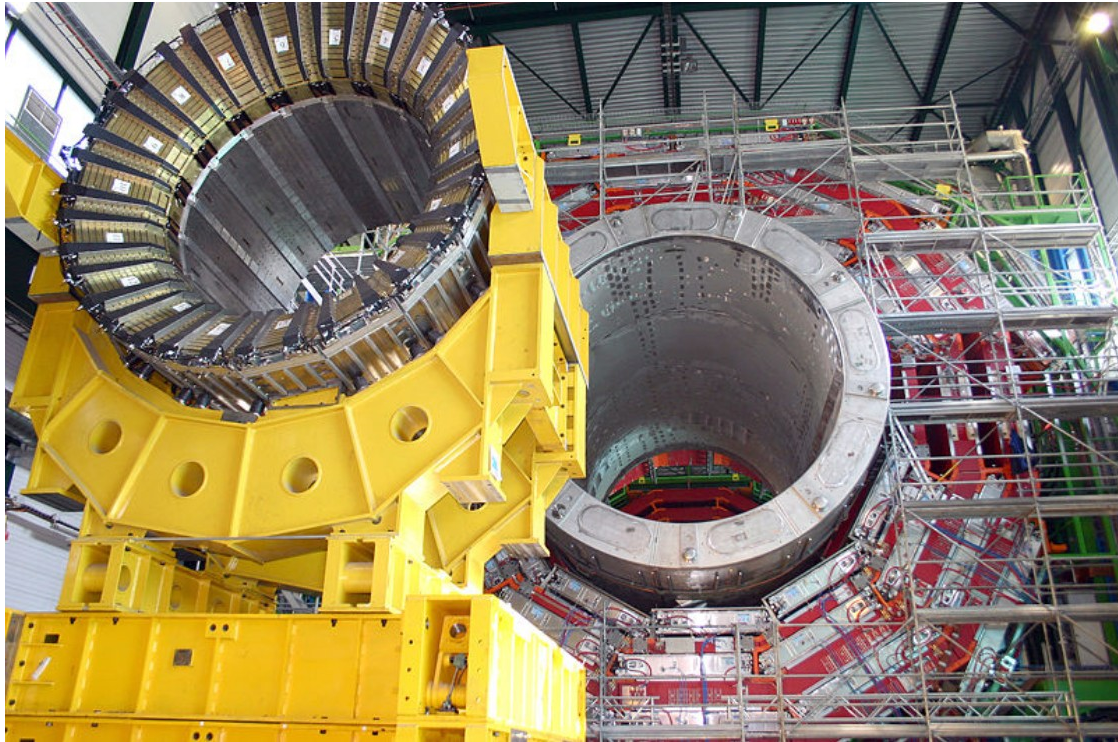


*Figure 14 – Assembling of the Hadronic Calorimeter (on the left) [9]*

For this purpose, the HCAL is divided into barrel (HB and HO), endcap (HE) and forward (HF) sections, Figure 15. In HB there are 36 barrel wedges, made out of flat brass absorber plates (70%Cu, 30%Zn) aligned parallel to the beam axis.

The HE region is divided into 36 endcap wedges and it corresponds to 13.2% of the solid angle and contains about 34% of the particles produced in the final state. Since HCAL calorimeter is located in the ends of the CMS magnet, the use of a non-magnetic material for the absorber was needed: the C26000 cartridge brass has been employed. The geometry of plates is staggered so that no projective dead is present.

The outer barrel (HO), sit outside the coil, ensuring no energy leaks out the back of the HB undetected. Finally, the two hadronic forward calorimeters (HF) are positioned at both ends of CMS. The HF is divided azimuthally in 36 modular wedges and it uses a Cherenkov-based, radiation-hard technology.

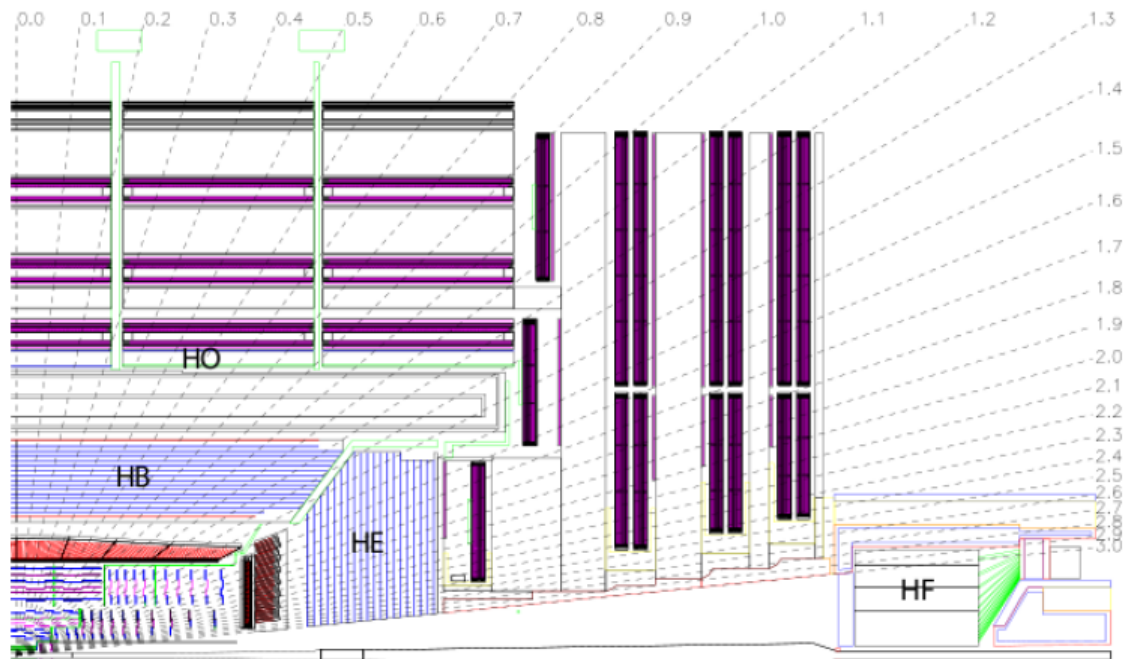


Figure 15 – Hadronic Calorimeters in CMS[4]

The HF has to experience very high particle radiation: into the forward calorimeters 760 GeV energy per proton-proton collision are on average deposited, while only 100 GeV for the rest of the detector. For such harsh conditions, the detector is therefore housed in a hermetic radiation shielding which consists of 45 layers of 40 cm thick steel, 40 cm of concrete, and 5 cm of polyethylene. A large plug structure in the back of the detector provides additional shielding.

### 1.2.6. THE MUON SYSTEM

Muons are charged particles 200 times heavier than electrons and positrons. They are produced in the decay of several potential new particles; for example, one of the clearest signature of the Higgs Boson is represented by its decay into four muons. CMS Moun System (MS) provides excellent muon identification, triggering and momentum reconstruction.

Muons are not stopped by any of CMS's calorimeters, therefore they can penetrate several meters of iron without interacting. For this reason the MS chambers are placed at the very edge of the experiment, where muons are the only particles which can produce a signal.

In the MS, a particle path is measured by fitting a curve through the multiple layers of each one of the four muon stations of the MS. By combining data with the measurements from the tracker detectors, a precise path followed by the particle can be reconstructed. The CMS magnet is very powerful in order to bend even the paths of very high-energy particle as muons and calculate their momentum.

The Muon System has a cylindrical barrel section around the superconducting solenoid and 2 planar endcap regions. Its durability is less influenced by radiation rate with respect to other detectors. In total there are 1400 muon chambers: 250 drift tubes (DTs) and 540 cathode strip chambers (CSCs) track the particles' positions and provide a trigger, while 1506 resistive plate chambers (RPCs) form a redundant trigger system, which quickly decides to keep the acquired muon data or not. The barrel drift tube chambers, with standard rectangular drift cells, are divided into 4 stations located among the layers of iron yoke plates.

DT can unambiguously identify muons bunch crossing identification. In the CMS endcap cathode strip chambers (CSC) were preferred due to their fast response time. Furthermore Resistive Plate Chambers (RPC) were added in both the barrel and endcap regions of the CMS Muon System: they have a fast response and excellent time resolution.

### **1.2.7. DRIFT TUBES**

Muon positions in the barrel region of the detector are measured by the Drift Tube (DT) system. Each tube has a width of 4 cm and contains a stretched wire within a gas volume. When a muon or any other charged particle passes through the volume it removes electrons from the atoms of the gas. The electrons then are conducted by the electric field towards the positively-charged wire.

---

By registering the position along the wire where hit occur and by calculating the muon original distance from the DTs wire, the two coordinates for the muon position are obtained.

Each DT chamber has a surface with dimensions of 2m x 2.5m, and is made by three groups of four aluminum layers. Each of them contains up to 60 tubes: the middle group measures the coordinate along the direction of the beam while the two outside groups measure the coordinates perpendicular to the first. The transverse dimension of the cell, which is also the a maximum drift path, is 21 mm. This corresponds to a maximum drift time of 380 ns in a gas mixture of 85% Ar + 15% CO<sub>2</sub>

### **1.2.8. CATHODE STRIP CHAMBERS**

Cathode strip chambers (CSC) are used in the endcap disks. They are made of arrays of positively-charged anode wires crossed with negatively-charged copper cathode strips within a gas volume. When muons pass through the chamber, they hit electrons of the gas atoms creating subsequently an avalanche of electrons. A charge pulse in the strips is then induced by positive ions generated, which move away from the wire towards the copper cathode at right angles to the wire direction. A CSC chamber in CMS is comprised of 6 anode wire planes interleaved among 7 cathode panels. The wires run azimuthally, allowing precise measurement of the track's radial coordinate. Strips run instead along the radius, therefore perpendicularly to the wires direction, allowing to obtain the two position coordinates for each particle passing through.

Since the wires are very close each other, the CSCs are fast detectors with both a good spatial and time resolution. Six layers contained in each CSC module allow accurate identification of muons, in order to match their paths to those detected by the tracker.

### **1.2.9. RESISTIVE PLATE CHAMBERS**

Resistive plate chambers (RPC), Figure 16, provide an additional muon trigger system with those of the DTs and CSCs. RPCs are fast gaseous detectors that consist of two parallel plates, a positively-charged anode

---

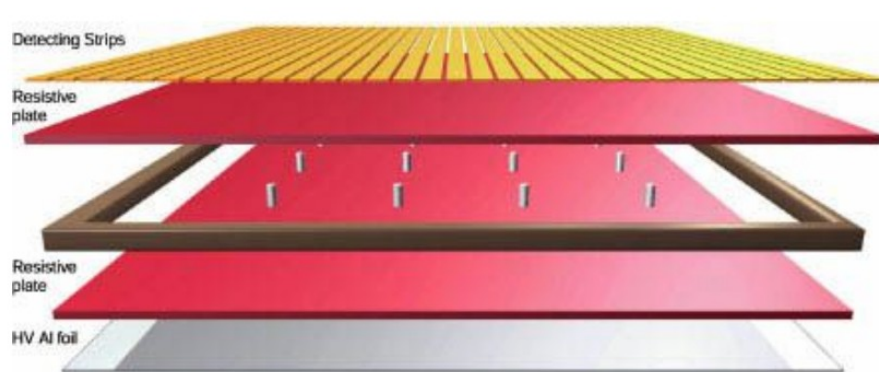


Figure 16 – Resistive Plate Chamber layers [9]

and a negatively-charged cathode, separated by the gas volume. Both the plates are made by High Pressure Laminated (HPL) material with a very high resistivity ( $10^{10}$  ohm cm).

When a muon passes through the chamber, electrons are knocked out of from the gas atoms. These electrons hit other atoms causing an avalanche of electrons. Since the electrodes are transparent to the electrons, after a short but precise timing, the external metal strips collect the electrons allowing a precise measure of the muon momentum by the pattern of the hit strips. It this way RPCs combine adequate spatial resolution with a time resolution comparable to that of scintillators (about one nanosecond)

Barrel RPCs are disposed in 6 and roughly cylindrical coaxial layers, revolving around the beam axis. They are arranged in four stations, as for the DTs, and each station is subdivided in 5 wheels along the z axis. The RPCs Endcap are arranged in 4 disks supported by the iron yoke. The chambers overlap in  $\phi$  to avoid dead space. Each endcap RPC chamber consists of a double-gap structure enclosed in a flat trapezoidal shaped box made of 2 aluminum honeycomb panels of 6 mm thickness each.

### 1.3. FIBER OPTICAL SENSORS FOR HIGH ENERGY PHYSICS

High Energy Physics Experiment require manufacturing of very complex machines, which impose to find solution to really hard design challenges. Such kind of machines need anyway also an efficient monitoring system to prevent the damage which can be caused by different factors, such as too high or too low

temperature, excessive stress and strain due the intense magnetic field, irradiation, condensation of humidity inside the electronic equipment and so on; traditional sensing system based on electrical sensor present serious drawback in the High Energy Physics environmental conditions, in particular for the presence of very intense electromagnetic fields, which generate high noise levels, with also the concomitant presence of a very high level of irradiation, for which elevated Radiation Hardness Capability are a fundamental requests. Fiber optical sensor offer an immediate solution for this kind of problems: in particular their immunity toward electromagnetic noise factor make them clearly preferable with respect traditional sensors for this kind of applications. Furthermore they present many differ kind of advantages:

- Compactness and low weight
- Intrinsic multiplexing (many sensors can be mounted on the a single optical fiber, reducing the needing of several electric wires)
- Reduction of instrumentation and improvement of the workplace safety
- Intrinsic safety due the passive operation
- Lower cost of the devices for the data acquisition
- Good Radiation Hardness Capability
- Noise immunity (especially respect to the electromagnetic fields) which allow to avoid frequent recalibrations
- Reduced needing of services
- Low attenuation of the optical signal, also on long distances
- Suitability for many different kinds of measures (Temperature with commercial sensors and Humidity, Cryogenic T with prototypes discussed in present thesis)
- Water and corrosion resistance
- Linear and fast response in a wide range of operative conditions

The evident advantage with respect to traditional electronic sensor represented in the last decades a strong impulse to the research in this field of photonic, in particular for application of fiber optic technology to the

---

communication and sensing devices. In the High energy Physics, however, it's well known that the high nuclear radiation have effects on both electronic and photonic components, since radiation alters materials characteristics modifies the performances of components, and in the worst case components are subject to irreversible damage causing failures and system malfunctions, with financial repercussions and some time serious consequences for safety, as well explained in [6].

However the actual manufacturing technologies of optical fibers allow to fabricate fiber with a very low level of sensitivity to radiation: it's well known, indeed, that radiation induce attenuation on the optical signal (Radiation Induce Attenuation, RIA); the SMF28 optical fiber has been indeed chosen for this characteristic, crucial in the High Energy Physics field of application. In particular, as discussed in the following sections, it has been selected in CMS experiment also for data transfer.

Fiber Bragg Grating Sensors (FBG) represent one of the most important devices for photonic sensing device. As discussed deeply in the Chapter 2, a Bragg grating is a periodic modulation of the refractive index of the medium, presenting a peak in the reflected spectrum in correspondence of a particular, Bragg wavelength, which is mainly dependent by the period of perturbation of the refractive index and by the effective refraction index. FBGs represent a versatile photonic component that can be applied in both optical communication and sensing systems for many kind of measure, even if at present their major field of commercial application is for Strain and Temperature. Depending on the grating type and on the grating fabrication, it has been demonstrated they can be employed without problems also in the High Energy Physics environmental conditions.

The absorbed dose in the most critical region of CMS silicon tracker detector, having its inner region at only few cm from the interaction point where particle collision takes place, is about of  $10^3$  kGy in 10 years. LHC proton-proton beam collisions are planned with a rate of 3 year data taking period (called RUN) and 2 years technical stop period (called Long ShutDown - LS). LHC completed in 2012 its first run period (RUN1) and it is at present in LS1 period, being completed at the end of 2014. In RUN1 period a dose of about 80kGy

---

was accumulated in the most critical region of CMS tracker. In RUN2 and RUN3 periods (2015-17 and 2020-22 respectively) doses of 250 kGy and 750kGy are expected.

## **1.4. OVERVIEW OF THE EXISTING FIBER OPTICAL SENSORS (FOS) IN CMS**

### **1.4.1. TEMPERATURE FOS INSTALLATIONS IN CMS**

The temperature monitoring in CMS is crucial to control the operative conditions the CMS detectors and their components, mainly for those equipments whose working performance are affected by the thermal conditions or must operate strictly inside a precise range of temperature. In the last years classical electrical sensors based on thermocouples (PT100) have been widely employed for this purpose in CMS. The main drawbacks reside inside the complexity of the cabling network needed, relevant for an high number of sensor required, since each PT100 must be connected at least through 2 electrical wires to transmit signal. Moreover the intense magnetic field represent a strong source of noise and instabilities, and their radiation hardness capability limited the regions where they could be installed.

Fiber Optical Sensor technology in CMS overcame these issues, reducing drastically the amount of installed wires; an excellent agreement was demonstrated between Temperature recorded by FBG sensors and by classical PT100 thermocouples with a resolution in the range of  $\pm 0.2^{\circ}\text{C}$  [6]. The intrinsic independence of their performances by the electromagnetic field as been demonstrated also with their use in HEP detectors, by the absolute absence of induced noise. From 2009, when first installation was made for temperature monitoring of the tracker volume on both positive and negative sides of the CMS Tracker, several further hundred of Temperature FBG sensors have been installed in CMS.

At present FBG Temperature sensors are installed inside the Experimental Cavern (60 sensors) to monitor environment conditions, on the Tracker Bulk Head on both sides (20 sensors), on Pixel Luminosity Telescope (PLT) (2 sensors), on the RPC End Cap Disks (432 sensors) to monitor T for each of 72 detector chambers, through 2 arrays installed on each endcap disk as presented in the Figure 17.

---

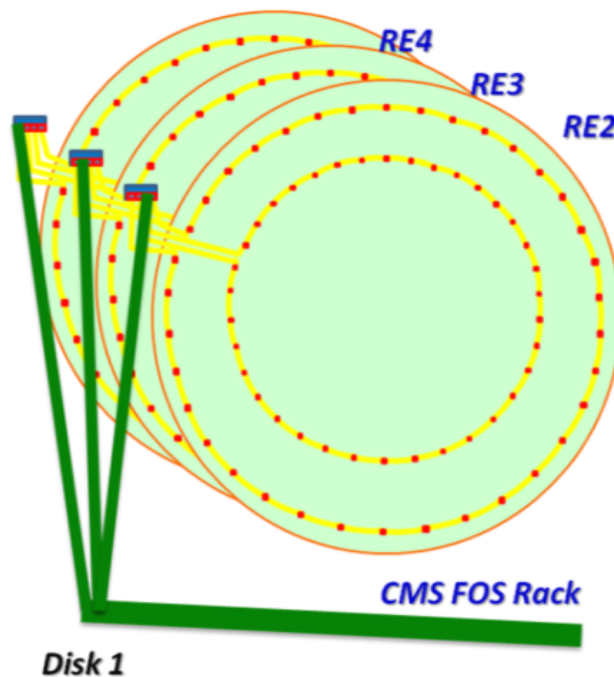


Figure 17 –Installation Layout of the Temperature FBG Sensors on the End Cap Disks

#### 1.4.2. STRAIN FOS INSTALLATIONS IN CMS

Also Strain monitoring in CMS plays a crucial role in order to protect from damage the installed equipment in CMS. Indeed monitoring mechanical deformations is fundamental to guarantee the stability and compensate/correct possible misalignment of different sub-detectors induced by the high magnetic forces. Indeed considering the very large amount of iron structures in CMS subjected to the magnetic actions generated by the solenoid, it's easy to understand the importance of structural monitoring.

The first installed strain FOS sensor in 2009 regarded the very forward part of the detector in the negative side of the experimental area [6]. As shown the Figure 18, in the region corresponding to the Forward Hadronic Calorimeter (HF) 4 metal supports called RAISERS hold up the platform where the beam pipe is placed together with an additional CSM calorimeter detector called CASTOR. Since both HF and CASTOR are very close (few mm) to the beam-pipe of the LHC, any motion or deformation in this region caused by

the intense 4T magnetic field generated by CMS solenoid, could cause serious damages to the beam pipe. By consequence a complete strain monitoring of the Raisers was crucial.



*Figure 18 – Raiser (Yellow structures) supporting the Castor (Orange) and the Platform (Green) Central LHC Beam Pipe (Yellow)*

In 2009 18 strain FOS sensors were therefore installed in the HF region negative side, 10 strain FBGs plus 2 for the temperature compensations on the 4 reinforcement beams on the corners of the RAISER. 4 strain + 1 T, under the metallic platform as presented in the Figure 18. 4 strain + 1 T sensor were installed in the CASTOR detector support. Their data were recorded during the CMS B field cycles, proving that induced deformation on the Raisers were not invasive for the HF and Castor position with respect to beam pipe. At present further FBGs are being installed in CMS to monitor deformations induced by B field on the YE4 Shielding Disk (36 sensors), (see Figure 19), and to monitor the Temperature and strain distribution by high

---

radiation hardness FBGs along the new beam pipe, presenting a reduced diameter to allow the installation of a further layer in the Silicon Tracker (see Figure 20).

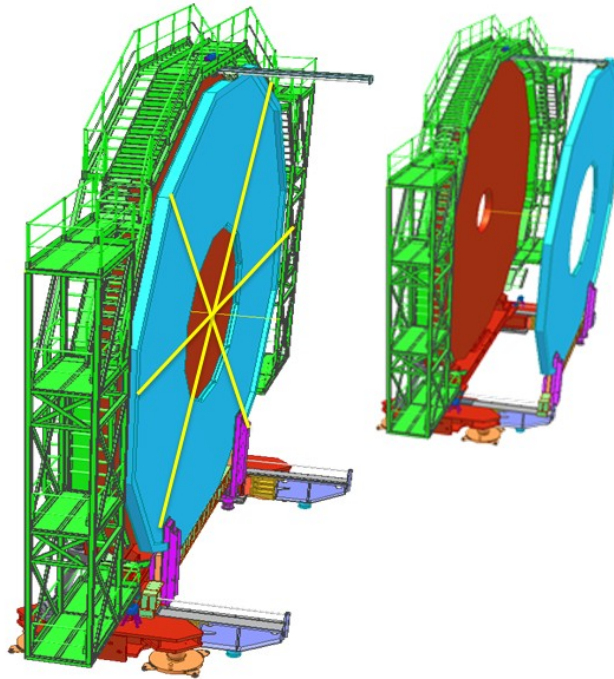


*Figure 19 –YE4 Shielding Disk where FBG Strain Sensors have been installed*

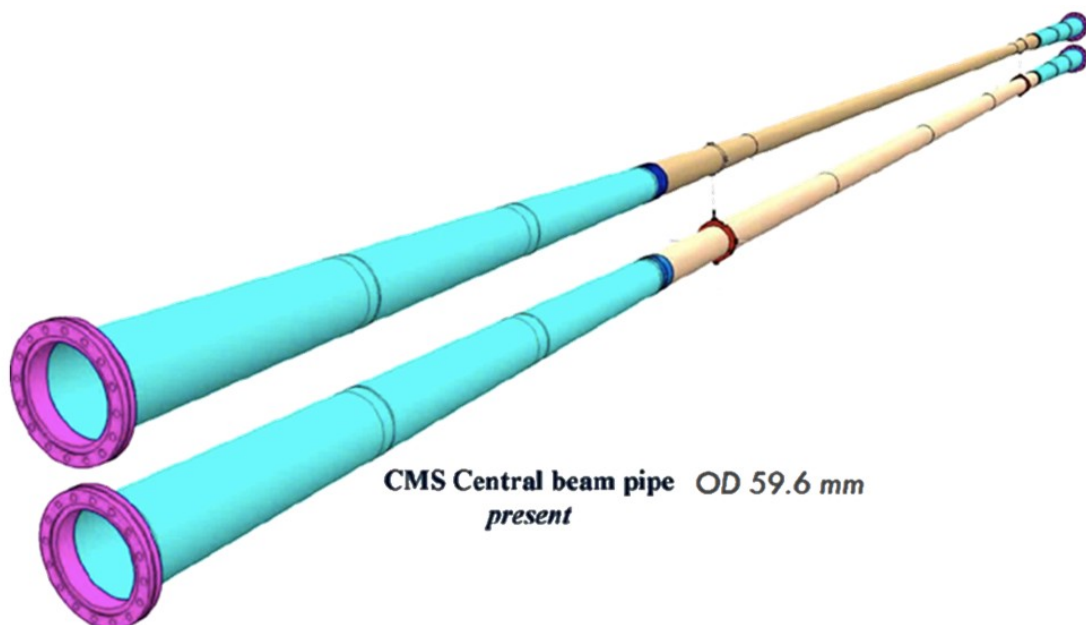


*Figure 20 –Comparison between the current and the new Central Beam Pipe monitored by FOS*

---

# CHAPTER 2

## FBG OPTICAL ANALYSIS

### 2.1. FBG WORKING PRINCIPLE

A Bragg grating is a periodic modulation of the refractive index of the medium and it can be schematically represented by grooves in the next Figure 21, where the period of the grating is  $\Lambda$  while the effective refractive index is  $n$ . When a wave encounters a groove, it is partially reflected and partially transmitted; therefore, in order to get the reflected wave is in phase with the wave reflected by the neighbor groove, the optical path must be equal to a whole number of wavelengths: considering that a wave must travel forward and then it must be back reflected, the total optical path is given by  $2n\Lambda$ . Therefore, in order to get the waves in phase, it must be

$$2n\Lambda = m\lambda$$

Eq. 4

---

with  $m$  an integer. The equation Eq. 4 represents a case of the well-known Bragg law; here we can assume  $m=1$  and then:

$$\lambda = 2n\Lambda \tag{Eq. 5}$$

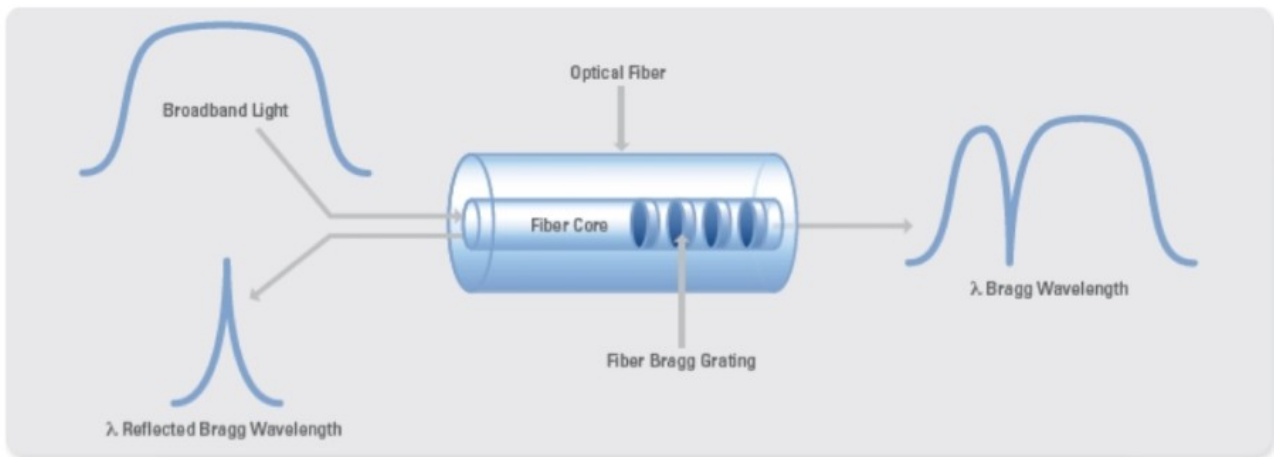


*Figure 21 – Fiber Bragg Grating*

A simplified mathematical dissertation of the optical of the FBG can be carried out by considering only a single mode and taking into account the coupling between the forward and the reflected waves; in this way and it's possible to evaluate the coefficients of reflection and transmission of the grating knowing the FBG characteristics such as the grating length, the grating period, the effective refractive index and the amplitude of the refractive index perturbation. For a such kind of analysis, as for example well described in [11], it's necessary to consider the Maxwell equations for a waveguide formed by a dielectric medium: of course in this case the dielectric is represented by the optical fiber with the refractive index modulated.

## 2.2. MAXWELL EQUATIONS FOR AN OPTICAL DIELECTRIC MEDIUM

The Maxwell's equations for a dielectric medium can be written as:

$$\begin{cases} \nabla \times \vec{E} = -\mu \frac{\partial \vec{H}}{\partial t} \\ \nabla \times \vec{H} = \varepsilon \frac{\partial \vec{E}}{\partial t} \end{cases} \quad \text{Eq. 6}$$

In which  $\mu$  and  $\varepsilon$  represent respectively the magnetic permeability and the dielectric constant of the medium.

In the domain of phasors, the electric and magnetic field can be factorized in a position-dependent term and a time-dependent term, and they can be written as:

$$\begin{cases} \vec{E} = \vec{E}(x, y, z)e^{i\omega t} \\ \vec{H} = \vec{H}(x, y, z)e^{i\omega t} \end{cases} \quad \text{Eq. 7}$$

Since the rotor acts on the only spatial term, replacing the Eq. 7 in the Maxwell equations Eq. 6 we obtain:

$$\begin{cases} (\nabla \times \vec{E})e^{i\omega t} = -i\omega\mu\vec{H}e^{i\omega t} \\ (\nabla \times \vec{H})e^{i\omega t} = +i\omega\varepsilon\vec{E}e^{i\omega t} \end{cases} \quad \text{Eq. 8}$$

Eliminating the function  $e^{i\omega t}$ , the above equations can be written as:

$$\begin{cases} \nabla \times \vec{E} = -i\omega\mu\vec{H} \\ \nabla \times \vec{H} = +i\omega\varepsilon\vec{E} \end{cases} \quad \text{Eq. 9}$$

By applying the operator of the rotor to both the members in the first equation, one obtains:

$$\begin{cases} \nabla \times (\nabla \times \vec{E}) = \nabla \times (-i\omega\mu\vec{H}) \\ \nabla \times \vec{H} = +i\omega\varepsilon\vec{E} \end{cases} \quad \text{Eq. 10}$$

$$\begin{cases} \nabla \times (\nabla \times \vec{E}) = -i\omega\mu\nabla \times \vec{H} \\ \nabla \times \vec{H} = +i\omega\varepsilon\vec{E} \end{cases} \quad \text{Eq. 11}$$

---

since the rotor of the rotor is given by:

$$\nabla \times (\nabla \times \vec{E}) = \nabla (\nabla \cdot \vec{E}) - \nabla^2 \vec{E} \quad \text{Eq. 12}$$

by substituting into the first one of the Eq. 11, one has:

$$\begin{cases} \nabla (\nabla \cdot \vec{E}) - \nabla^2 \vec{E} = -i\omega\mu(i\omega\varepsilon\vec{E}) \\ \nabla \times \vec{H} = +i\omega\varepsilon\vec{E} \end{cases} \quad \text{Eq. 13}$$

$$\begin{cases} \nabla (\nabla \cdot \vec{E}) - \nabla^2 \vec{E} = -i^2\omega^2\mu\varepsilon\vec{E} \\ \nabla \times \vec{H} = +i\omega\varepsilon\vec{E} \end{cases} \quad \text{Eq. 14}$$

$$\begin{cases} \nabla (\nabla \cdot \vec{E}) - \nabla^2 \vec{E} = \omega^2\mu\varepsilon\vec{E} \\ \nabla \times \vec{H} = +i\omega\varepsilon\vec{E} \end{cases} \quad \text{Eq. 15}$$

from the second equation one gets:

$$\vec{E} = \frac{\nabla \times \vec{H}}{i\omega\varepsilon} \quad \text{Eq. 16}$$

which, replaced in the gradient of the divergence, allows to write:

$$\nabla (\nabla \cdot \vec{E}) = \nabla \left( \frac{\nabla \cdot \nabla \times \vec{H}}{i\omega\varepsilon} \right) \quad \text{Eq. 17}$$

since, as well known, the divergence of a rotor is always identically zero, from the first equation we get:

$$\nabla (\nabla \cdot \vec{E}) - \nabla^2 \vec{E} = \omega^2\mu\varepsilon\vec{E} \quad \text{Eq. 18}$$

$$0 - \nabla^2 \vec{E} = \omega^2\mu\varepsilon\vec{E} \quad \text{Eq. 19}$$

$$\nabla^2 \vec{E} + \omega^2\mu\varepsilon\vec{E} = 0 \quad \text{Eq. 20}$$

If we define:

$$k^2 = \omega^2 \mu \epsilon \quad \text{Eq. 21}$$

since the index of refraction of a medium is given by the square root of the product of the relative permeability for the relative dielectric constant of the medium:

$$n = \sqrt{\mu_r \epsilon_r} \quad \text{Eq. 22}$$

With:

$$\begin{cases} \mu = \mu_0 \mu_r \\ \epsilon = \epsilon_0 \epsilon_r \end{cases} \quad \text{Eq. 23}$$

And the speed of the light in the vacuum given by:

$$c = \frac{1}{\sqrt{\mu_0 \epsilon_0}} \quad \text{Eq. 24}$$

we have that:

$$k^2 = \frac{\omega^2 n^2}{c^2} \quad \text{Eq. 25}$$

We can observe that the vectorial equation Eq. 20 is equivalent to a system of 3 Helmholtz equations for each of the three components of the electric field:

$$\begin{cases} \nabla^2 E_x + k^2 E_x = 0 \\ \nabla^2 E_y + k^2 E_y = 0 \\ \nabla^2 E_z + k^2 E_z = 0 \end{cases} \quad \text{Eq. 26}$$

---

### 2.2.1. MODULATION OF THE REFRACTIVE INDEX

Now we can assume that  $z$  is the axis of the FBG and that the refractive index of the grating varies periodically along the axis, according to the equation:

$$n = n_{xy}(x, y) + \Delta n_z(z) \tag{Eq. 27}$$

where  $n_{xy}(x, y)$  represents the variation of the refractive index in the transverse plane while  $\Delta n_z(z)$  represents the perturbation in the direction of the axis of the gratings. Here it's however worth to evidence that several kinds of Bragg gratings exist, each of them characterized by a different perturbative function  $\Delta n_z(z)$ . In the subsequent Figure 22 some types of gratings are shown with the relative diagram of the perturbation of refractive index along the axis:

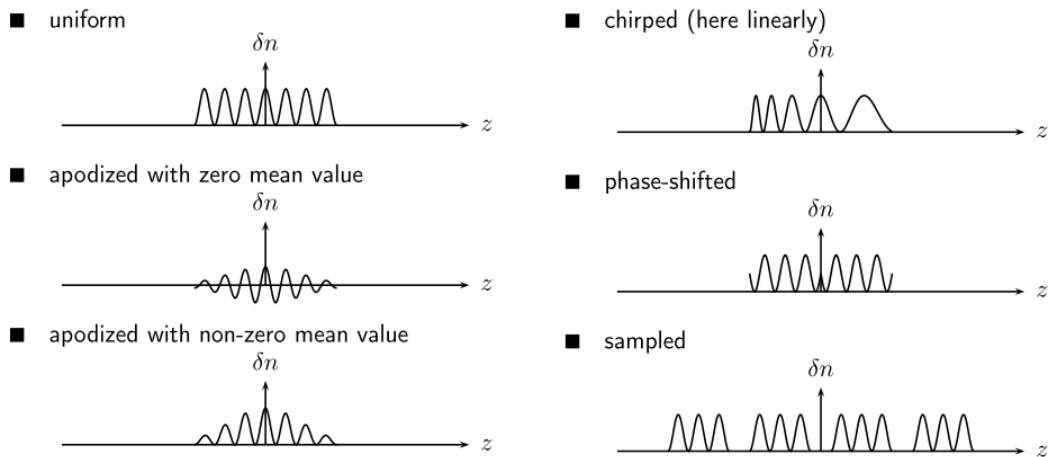


Figure 22 – Typical Fiber Bragg Grating refractive index axial variation [10]

in the case where the sinusoidal perturbation is the expression of the refractive index can be written as:

$$n = n_{xy}(x, y) + \Delta n \cos(kz) \tag{Eq. 28}$$

$$\text{with } k = \frac{2\pi}{\Lambda} \quad \text{Eq. 29}$$

Where  $\Lambda$  is thus the period of the grating and  $\Delta n$  the amplitude of the perturbation. For a sinusoidal perturbation, the equations of the electromagnetic field can be solved analytically; the wave equation of propagation of the transverse field, for example in relation to the y component, can be written as:

$$\nabla^2 E_y + \frac{(n\omega)^2}{c^2} E_y = 0 \quad \text{Eq. 30}$$

$$\nabla^2 E_y + [n_{xy} + \Delta n \cos(kz)]^2 \omega^2 c^{-2} E_y = 0 \quad \text{Eq. 31}$$

$$\nabla^2 E_y + [n_{xy}^2 + 2 n_{xy} \Delta n \cos(kz) + \Delta n^2 \cos^2(kz)] \omega^2 c^{-2} E_y = 0 \quad \text{Eq. 32}$$

By defining:

$$k_0^2 = \omega^2 c^{-2} \quad \text{Eq. 33}$$

and ignoring the contribution of the square of the periodic variation of the refractive index, the Eq. 32 can be simplified as it follows:

$$\nabla^2 E_y + [n_{xy}^2 + 2 n_{xy} \Delta n \cos(kz)] k_0^2 E_y = 0 \quad \text{Eq. 34}$$

### 2.2.2. SOLUTION FOR THE TRANSVERSE COMPONENT OF THE FIELD

By expressing the transverse component of the electric field as a product of two terms, functions respectively of the only axial coordinate z and of the only transverse coordinates x , y, one has:

$$E_y = \epsilon(z) E(x, y) \quad \text{Eq. 35}$$

---

Therefore, it results:

$$\nabla^2 E_y = \frac{\partial^2}{\partial x^2} E_y + \frac{\partial^2}{\partial y^2} E_y + \frac{\partial^2}{\partial z^2} E_y \quad \text{Eq. 36}$$

$$\nabla^2 E_y = \frac{\partial^2}{\partial x^2} [\epsilon(z)E(x, y)] + \frac{\partial^2}{\partial y^2} [\epsilon(z)E(x, y)] + \frac{\partial^2}{\partial z^2} [\epsilon(z)E(x, y)] \quad \text{Eq. 37}$$

$$\nabla^2 E_y = \epsilon(z) \frac{\partial^2}{\partial x^2} E(x, y) + \epsilon(z) \frac{\partial^2}{\partial y^2} E(x, y) + E(x, y) \frac{\partial^2}{\partial z^2} \epsilon(z) \quad \text{Eq. 38}$$

And by assuming:

$$\nabla_{xy}^2 = \frac{\partial^2}{\partial x^2} + \frac{\partial^2}{\partial y^2} \quad \text{Eq. 39}$$

One can also write:

$$\nabla^2 E_y = \epsilon(z) \nabla_{xy}^2 E(x, y) + E(x, y) \frac{\partial^2}{\partial z^2} \epsilon(z) \quad \text{Eq. 40}$$

$$\epsilon(z) \nabla_{xy}^2 E(x, y) + E(x, y) \frac{\partial^2}{\partial z^2} \epsilon(z) + [n_{xy}^2 + 2 n_{xy} \Delta n \cos(kz)] k_0^2 \epsilon(z) E(x, y) = 0 \quad \text{Eq. 41}$$

By assuming that the solution is given by the sum of a progressive wave and of back travelling wave with wave number  $\beta$ , it results:

$$\epsilon(z) = F(z)e^{-i\beta z} + B(z)e^{+i\beta z} \quad \text{Eq. 42}$$

with:

$$\beta = \frac{2\pi n}{\lambda} \quad \text{Eq. 43}$$

$$\epsilon(z) = F(z)e^{-i\beta z} + B(z)e^{-i(\beta-k)z} \quad \text{Eq. 44}$$

in the last relation the condition  $k \approx 2\beta$  was used; this condition is valid if the Bragg equation, Eq. 4, is verified; in this case in fact one has:

$$k \approx 2\beta \Rightarrow \frac{2\pi}{\Lambda} = 2 \frac{2\pi n}{\lambda} \Rightarrow \lambda = 2\Lambda n \quad \text{Eq. 45}$$

### 2.3. AMPLITUDE EQUATIONS OF THE PROGRESSIVE AND BACK TRAVELLING WAVES

By substituting the equation Eq. 44 into Eq. 41, one obtains:

$$\begin{aligned} & [F(z)e^{-i\beta z} + B(z)e^{-i(\beta-k)z}] \nabla_{xy}^2 E(x, y) + E(x, y) \frac{\partial^2}{\partial z^2} [F(z)e^{-i\beta z} + B(z)e^{-i(\beta-k)z}] + \\ & + [n_{xy}^2 + 2 n_{xy} \Delta n \cos(kz)] k_0^2 [F(z)e^{-i\beta z} + B(z)e^{-i(\beta-k)z}] E(x, y) = 0 \end{aligned} \quad \text{Eq. 46}$$

From which, by explaining the derivatives calculated with respect coordinated z, we get:

$$\begin{aligned} & [F(z)e^{-i\beta z} + B(z)e^{-i(\beta-k)z}] \nabla_{xy}^2 E + E \left( \frac{d^2 F}{dz^2} - 2i\beta \frac{dF}{dz} - F\beta^2 \right) e^{-i\beta z} + \\ & + E \left( \frac{d^2 B}{dz^2} - 2i(\beta - k) \frac{dB}{dz} - B(\beta - k)^2 \right) e^{-i(\beta-k)z} + \\ & + [n_{xy}^2 + 2 n_{xy} \Delta n \cos(kz)] k_0^2 [F(z)e^{-i\beta z} + B(z)e^{-i(\beta-k)z}] E = 0 \end{aligned} \quad \text{Eq. 47}$$

which can be re arranged as it follows:

$$\begin{aligned} & [F(z)e^{-i\beta z} + B(z)e^{-i(\beta-k)z}] (\nabla_{xy}^2 E + n_{xy}^2 k_0^2 E) + \left( \frac{d^2 F}{dz^2} - 2i\beta \frac{dF}{dz} - F\beta^2 \right) e^{-i\beta z} + \\ & + \epsilon \left( \frac{d^2 B}{dz^2} - 2i(\beta - k) \frac{dB}{dz} - B(\beta - k)^2 \right) e^{-i(\beta-k)z} + \\ & + 2 n_{xy} \Delta n \cos(kz) k_0^2 [F(z)e^{-i\beta z} + B(z)e^{-i(\beta-k)z}] \epsilon = 0 \end{aligned} \quad \text{Eq. 48}$$

In order to evaluate the term  $(\nabla_{xy}^2 E + n_{xy}^2 k_0^2 E)$ , one can use the solution of the unperturbed equation and it results:

$$\nabla_{xy}^2 E(x, y) + [n_{xy}^2(x, y)k_0^2 - \beta^2]E(x, y) = 0 \quad \text{Eq. 49}$$

and then:

$$\nabla_{xy}^2 E(x, y) + n_{xy}^2(x, y)k_0^2 E(x, y) = \beta^2 E(x, y) \quad \text{Eq. 50}$$

substituting the Eq. 50 in the Eq. 48, neglecting the contribution of the second derivatives of F and B and assuming  $n = n_{xy}$ , one has:

$$\begin{aligned} & [F(z)e^{-i\beta z} + B(z)e^{-i(\beta-k)z}]\beta^2 E(x, y) + E(x, y) \left( -2i\beta \frac{dF}{dz} - F\beta^2 \right) e^{-i\beta z} + \\ & + E(x, y) \left( -2i(\beta - k) \frac{dB}{dz} - B(\beta - k)^2 \right) e^{-i(\beta-k)z} + \\ & + 2 n \Delta n \cos(kz) k_0^2 [F e^{-i\beta z} + B e^{-i(\beta-k)z}] E(x, y) = 0 \end{aligned} \quad \text{Eq. 51}$$

simplifying E (x,y) we get:

$$\begin{aligned} & [F(z)e^{-i\beta z} + B(z)e^{-i(\beta-k)z}]\beta^2 + \left( -2i\beta \frac{dF}{dz} - F\beta^2 \right) e^{-i\beta z} + \\ & + \left( -2i(\beta - k) \frac{dB}{dz} - B(\beta - k)^2 \right) e^{-i(\beta-k)z} + \\ & + 2 n \Delta n \cos(kz) k_0^2 [F e^{-i\beta z} + B e^{-i(\beta-k)z}] = 0 \end{aligned} \quad \text{Eq. 52}$$

By considering that  $\cos(kz)$  can be written as :

$$\cos(kz) = \frac{e^{-ikz} + e^{+ikz}}{2} \quad \text{Eq. 53}$$

It results:

$$\cos(kz) [Fe^{-i\beta z} + Be^{-i(\beta-k)z}] = \frac{e^{-ikz} + e^{+ikz}}{2} [Fe^{-i\beta z} + Be^{-i(\beta-k)z}] \quad \text{Eq. 54}$$

$$\cos(kz) [Fe^{-i\beta z} + Be^{-i(\beta-k)z}] = \frac{Fe^{-i(\beta+k)z} + Fe^{-i(\beta-k)z}}{2} + \frac{Be^{-i(\beta-2k)z} + Be^{-i\beta z}}{2} \quad \text{Eq. 55}$$

From the last equality one can note the two additional terms in  $e^{-i(\beta+k)z}$  and  $e^{-i(\beta-2k)z}$  which are not present in the solution previously assumed; these terms anyway can be neglected because they are out of phase; by replacing Eq. 55 in the Eq. 52, one gets:

$$\begin{aligned} & \left( -2i\beta \frac{dF}{dz} - F\beta^2 + F\beta^2 \right) e^{-i\beta z} + \left( -2i(\beta - k) \frac{dB}{dz} - B(\beta - k)^2 + B\beta^2 \right) e^{-i(\beta-k)z} + \\ & + 2n\Delta nk_0^2 \frac{Fe^{-i(\beta-k)z} + Be^{-i\beta z}}{2} = 0 \end{aligned} \quad \text{Eq. 56}$$

by grouping the terms in  $e^{-i\beta z}$ , the terms in  $e^{-i(\beta-k)z}$ , one obtains:

$$\begin{aligned} & \left( -2i\beta \frac{dF}{dz} + n\Delta nk_0^2 B \right) e^{-i\beta z} + \\ & + \left( -2i(\beta - k) \frac{dB}{dz} - B[(\beta - k)^2 - \beta^2] + n\Delta nk_0^2 F \right) e^{-i(\beta-k)z} = 0 \end{aligned} \quad \text{Eq. 57}$$

Then, by defining:

$$\Delta\beta = \beta - \frac{k}{2} \quad \text{Eq. 58}$$

It results that the Bragg condition is exactly verified only when  $\Delta\beta = 0$ ; in any case we can write:

$$(\beta - k)^2 - \beta^2 = (\beta + \beta - \beta - k)^2 - \beta^2 \quad \text{Eq. 59}$$

$$(\beta - k)^2 - \beta^2 = (2\Delta\beta - \beta)^2 - \beta^2 \approx -4\beta\Delta\beta \quad \text{Eq. 60}$$

Substituting in the Eq. 57 we have:

$$\left(-2i\beta \frac{dF}{dz} + n\Delta nk_0^2 B\right) e^{-i\beta z} + \left(-2i(\beta - k) \frac{dB}{dz} + 4\beta\Delta\beta B + n\Delta nk_0^2 F\right) e^{-i(\beta-k)z} = 0 \quad \text{Eq. 61}$$

And, being:

$$(\beta - k) \approx -\beta \quad \text{Eq. 62}$$

It results:

$$\left(-2i\beta \frac{dF}{dz} + n\Delta nk_0^2 B\right) e^{-i\beta z} + \left(2i\beta \frac{dB}{dz} + 4\beta\Delta\beta B + n\Delta nk_0^2 F\right) e^{-i(\beta-k)z} = 0 \quad \text{Eq. 63}$$

by dividing for  $2i\beta$ , one has:

$$\left(-\frac{dF}{dz} - i\frac{n\Delta nk_0^2}{2\beta} B\right) e^{-i\beta z} + \left(\frac{dB}{dz} - i2\Delta\beta B - i\frac{n\Delta nk_0^2}{2\beta} F\right) e^{-i(\beta-k)z} = 0 \quad \text{Eq. 64}$$

Since the Eq. 64 must be verified for every  $z$ , it must be:

$$\begin{cases} -\frac{dF}{dz} - i\frac{n\Delta nk_0^2}{2\beta} B = 0 \\ +\frac{dB}{dz} + i\frac{n\Delta nk_0^2}{2\beta} F - i2\Delta\beta B = 0 \end{cases} \quad \text{Eq. 65}$$

$$\begin{cases} \frac{dF}{dz} + i \frac{n\Delta n k_0^2}{2\beta} B = 0 \\ \frac{dB}{dz} - i \frac{n\Delta n k_0^2}{2\beta} F - i2\Delta\beta B = 0 \end{cases} \quad \text{Eq. 66}$$

Defining also:

$$\kappa = -\frac{n\Delta n k_0^2}{2\beta}; \quad \sigma = -\Delta\beta \quad \text{Eq. 67}$$

we have:

$$\begin{cases} \frac{dF}{dz} - i\kappa B = 0 \\ \frac{dB}{dz} + i\kappa F + i2\sigma B = 0 \end{cases} \quad \text{Eq. 68}$$

## 2.4. SOLUTION FOR THE PROGRESSIVE AND BACK TRAVELLING WAVE AMPLITUDES

This system of differential equations Eq. 68, can be solved analytically; if we define:

$$\begin{cases} F_0 = F(0) \\ B_0 = B(0) \end{cases} \quad \text{Eq. 69}$$

One gets:

$$\begin{cases} F(z) = \left( \frac{F_0\kappa + B_0\sigma}{2\kappa} - \frac{B_0\sigma}{2\kappa} \right) (e^{(\alpha z - i\sigma z)} + e^{(-\alpha z - i\sigma z)}) + \\ \quad + \left( i \frac{B_0\alpha}{2\kappa} + \frac{F_0\kappa + B_0\sigma}{2\kappa} \left( \frac{i\sigma}{\alpha} \right) \right) (e^{(\alpha z - i\sigma z)} - e^{(-\alpha z - i\sigma z)}) \\ B(z) = \frac{iF_0\kappa + B_0i\sigma + B_0\alpha}{2\alpha} e^{(-\alpha z - i\sigma z)} - \frac{iF_0\kappa + B_0i\sigma + B_0\alpha}{2\alpha} e^{(\alpha z - i\sigma z)} \end{cases} \quad \text{Eq. 70}$$

with:

$$\alpha = \sqrt{\kappa^2 - \sigma^2} \quad \text{Eq. 71}$$

By grouping the  $e^{-i\sigma z}$  term one has:

$$\begin{cases} F(z) = e^{-i\sigma z} \left[ \left( \frac{F_0\kappa + B_0\sigma}{2\kappa} - \frac{B_0\sigma}{2\kappa} \right) (e^{(\alpha z)} + e^{(-\alpha z)}) + \left( i \frac{B_0\alpha}{2\kappa} + \frac{F_0\kappa + B_0\sigma}{2\kappa} \left( \frac{i\sigma}{\alpha} \right) \right) (e^{(\alpha z)} - e^{(-\alpha z)}) \right] \\ B(z) = e^{-i\sigma z} \left[ \frac{B_0\alpha}{2\alpha} (e^{(\alpha z)} + e^{(-\alpha z)}) + \frac{iF_0\kappa + B_0i\sigma}{2\alpha} (e^{(-\alpha z)} - e^{(\alpha z)}) \right] \end{cases} \quad \text{Eq. 72}$$

Introducing the hyperbolic functions we can therefore also write:

$$\begin{cases} F(z) = e^{-i\sigma z} \left[ \left( \frac{F_0\kappa + B_0\sigma}{\kappa} - \frac{B_0\sigma}{\kappa} \right) \cosh(\alpha z) + \left( i \frac{B_0\alpha}{\kappa} + \frac{F_0\kappa + B_0\sigma}{\kappa} \left( \frac{i\sigma}{\alpha} \right) \right) \sinh(\alpha z) \right] \\ B(z) = e^{-i\sigma z} \left[ B_0 \cosh(\alpha z) - \frac{F_0\kappa + B_0\sigma}{\alpha} i \sinh(\alpha z) \right] \end{cases} \quad \text{Eq. 73}$$

By simplifying the expressions in parentheses, and being :

$$\alpha^2 = \kappa^2 - \sigma^2 \quad \text{Eq. 74}$$

One gets:

$$\begin{cases} F(z) = e^{-i\sigma z} \left[ F_0 \cosh(\alpha z) + \left( \frac{B_0\alpha^2 + F_0\kappa\sigma + B_0\sigma^2}{\kappa\alpha} \right) i \sinh(\alpha z) \right] \\ B(z) = e^{-i\sigma z} \left[ B_0 \cosh(\alpha z) - \frac{F_0\kappa + B_0\sigma}{\alpha} i \sinh(\alpha z) \right] \end{cases} \quad \text{Eq. 75}$$

$$\begin{cases} F(z) = e^{-i\sigma z} \left[ F_0 \cosh(\alpha z) + \left( \frac{B_0\kappa^2 - B_0\sigma^2 + F_0\kappa\sigma + B_0\sigma^2}{\kappa\alpha} \right) i \sinh(\alpha z) \right] \\ B(z) = e^{-i\sigma z} \left[ B_0 \cosh(\alpha z) - \frac{F_0\kappa + B_0\sigma}{\alpha} i \sinh(\alpha z) \right] \end{cases} \quad \text{Eq. 76}$$

in this way, the expressions of F and B can be written in a more compact manner as:

$$\begin{cases} F(z) = e^{-i\sigma z} \left[ F_0 \cosh(\alpha z) + \frac{B_0 \kappa + F_0 \sigma}{\alpha} i \sinh(\alpha z) \right] \\ B(z) = e^{-i\sigma z} \left[ B_0 \cosh(\alpha z) - \frac{F_0 \kappa + B_0 \sigma}{\alpha} i \sinh(\alpha z) \right] \end{cases} \quad \text{Eq. 77}$$

## 2.5. REFLECTIVITY AND TRANSMISSIVITY COEFFICIENTS OF THE GRATING

If the length of the grating is  $L$ , it must also be:

$$\begin{cases} F(0) = F_0 = 1 \\ B(L) = 0 \end{cases} \quad \text{Eq. 78}$$

Furthermore, by defining:

$$\begin{cases} \tau = F(L) \\ \rho = B(0) \end{cases} \quad \text{Eq. 79}$$

the reflectivity coefficient  $R$  and the transmissivity coefficient  $T$  of the grating are given by:

$$\begin{cases} T = |\tau^2| = \tau \tau^* \\ R = |\rho^2| = \rho \rho^* \end{cases} \quad \text{Eq. 80}$$

Calculating  $F$  and  $B$  in  $z = L$ , we obtain:

$$\begin{cases} F(L) = e^{-i\sigma L} \left[ F_0 \cosh(\alpha L) + \frac{B_0 \kappa + F_0 \sigma}{\alpha} i \sinh(\alpha L) \right] \\ B(L) = e^{-i\sigma L} \left[ B_0 \cosh(\alpha L) - \frac{F_0 \kappa + B_0 \sigma}{\alpha} i \sinh(\alpha L) \right] \end{cases} \quad \text{Eq. 81}$$

$$\begin{cases} F(L) = e^{-i\sigma L} \left[ \cosh(\alpha L) + \frac{B_0 \kappa + \sigma}{\alpha} i \sinh(\alpha L) \right] \\ B(L) = e^{-i\sigma L} \left[ B_0 \cosh(\alpha L) - \frac{\kappa + B_0 \sigma}{\alpha} i \sinh(\alpha L) \right] \end{cases} \quad \text{Eq. 82}$$

Having to be  $B(L) = 0$  we have:

$$\begin{cases} F(L) = e^{-i\sigma L} \left[ \cosh(\alpha L) + \frac{B_0 \kappa + \sigma}{\alpha} i \sinh(\alpha L) \right] \\ B_0 \cosh(\alpha L) - \frac{\kappa + B_0 \sigma}{\alpha} i \sinh(\alpha L) = 0 \end{cases} \quad \text{Eq. 83}$$

By solving the second equation with respect to  $B_0$ , one has:

$$\begin{cases} F(L) = e^{-i\sigma L} \left[ \cosh(\alpha L) + \frac{B_0 \kappa + \sigma}{\alpha} i \sinh(\alpha L) \right] \\ B_0 = -\frac{\kappa \sinh(\alpha L)}{\sigma \sinh(\alpha L) + i\alpha \cosh(\alpha L)} \end{cases} \quad \text{Eq. 84}$$

Substituting the expression of  $B_0$  in the first equality we have:

$$\begin{cases} F(L) = e^{-i\sigma L} \left[ \cosh(\alpha L) - \frac{\kappa \sinh(\alpha L)}{\sigma \sinh(\alpha L) + i\alpha \cosh(\alpha L)} \frac{\kappa}{\alpha} i \sinh(\alpha L) + \frac{\sigma}{\alpha} i \sinh(\alpha L) \right] \\ B_0 = -\frac{\kappa \sinh(\alpha L)}{\sigma \sinh(\alpha L) + i\alpha \cosh(\alpha L)} \end{cases} \quad \text{Eq. 85}$$

$$\begin{cases} F(L) = e^{-i\sigma L} \left[ \frac{-\frac{\kappa^2}{\alpha^2} \sinh^2(\alpha L)}{\cosh(\alpha L) - \frac{i\sigma}{\alpha} \sinh(\alpha L)} + \cosh(\alpha L) + \frac{\sigma}{\alpha} i \sinh(\alpha L) \right] \\ B_0 = -\frac{\kappa \sinh(\alpha L)}{\sigma \sinh(\alpha L) + i\alpha \cosh(\alpha L)} \end{cases} \quad \text{Eq. 86}$$

$$\begin{cases} F(L) = e^{-i\sigma L} \left[ \frac{\cosh^2(\alpha L) + \frac{\sigma^2 - \kappa^2}{\alpha^2} \sinh^2(\alpha L)}{\cosh(\alpha L) - \frac{i\sigma}{\alpha} \sinh(\alpha L)} \right] \\ B_0 = -\frac{\kappa \sinh(\alpha L)}{\sigma \sinh(\alpha L) + i\alpha \cosh(\alpha L)} \end{cases} \quad \text{Eq. 87}$$

Furthermore, since:

$$\kappa^2 - \sigma^2 = \alpha^2; \quad \cosh^2(\alpha L) - \sinh^2(\alpha L) = 1 \quad \text{Eq. 88}$$

One has:

---


$$\begin{cases} \tau = F(L) = e^{-i\sigma L} \left[ \frac{\alpha}{\alpha \cosh(\alpha L) - i\sigma \sinh(\alpha L)} \right] \\ \rho = B_0 = -\frac{\kappa \sinh(\alpha L)}{\sigma \sinh(\alpha L) + i\alpha \cosh(\alpha L)} \end{cases} \quad \text{Eq. 89}$$

And then:

$$\begin{cases} T = \tau\tau^* = \left( e^{-i\sigma L} \frac{\alpha}{\alpha \cosh(\alpha L) - i\sigma \sinh(\alpha L)} \right) \left( e^{+i\sigma L} \frac{\alpha}{\alpha \cosh(\alpha L) + i\sigma \sinh(\alpha L)} \right) \\ R = \rho\rho^* = \left( -\frac{\kappa \sinh(\alpha L)}{\sigma \sinh(\alpha L) + i\alpha \cosh(\alpha L)} \right) \left( -\frac{\kappa \sinh(\alpha L)}{\sigma \sinh(\alpha L) - i\alpha \cosh(\alpha L)} \right) \end{cases} \quad \text{Eq. 90}$$

$$\begin{cases} T = \frac{\alpha^2}{\alpha^2 \cosh(\alpha L) + \sigma^2 \sinh(\alpha L)} \\ R = \frac{\kappa^2 \sinh^2(\alpha L)}{\alpha^2 \cosh^2(\alpha L) + \sigma^2 \sinh^2(\alpha L)} \end{cases} \quad \text{Eq. 91}$$

The most common form for R and T in literature can be obtained substituting the expression of  $\alpha^2$ :

$$\begin{cases} T = \frac{\alpha^2}{(\kappa^2 - \sigma^2) \cosh(\alpha L) + \sigma^2 \sinh(\alpha L)} \\ R = \frac{\kappa^2 \sinh^2(\alpha L)}{(\kappa^2 - \sigma^2) \cosh^2(\alpha L) + \sigma^2 \sinh^2(\alpha L)} \end{cases} \quad \text{Eq. 92}$$

$$\begin{cases} T = \frac{\alpha^2}{\kappa^2 \cosh(\alpha L) - \sigma^2} \\ R = \frac{\kappa^2 \sinh^2(\alpha L)}{\kappa^2 \cosh^2(\alpha L) - \sigma^2} \end{cases} \quad \text{Eq. 93}$$

Obviously it is easy to verify that  $R + T = 1$ :

$$T + R = \frac{\alpha^2}{\kappa^2 \cosh(\alpha L) - \sigma^2} + \frac{\kappa^2 \sinh^2(\alpha L)}{\kappa^2 \cosh^2(\alpha L) - \sigma^2} \quad \text{Eq. 94}$$


---

$$T + R = \frac{(\kappa^2 - \sigma^2) + \kappa^2 \sinh^2(\alpha L)}{\kappa^2 \cosh^2(\alpha L) - \sigma^2} = \frac{\kappa^2 [1 - \sinh^2(\alpha L)] - \sigma^2}{\kappa^2 \cosh^2(\alpha L) - \sigma^2}$$

Eq. 95

$$T + R = \frac{\kappa^2 \cosh^2(\alpha L) - \sigma^2}{\kappa^2 \cosh^2(\alpha L) - \sigma^2} = 1$$

If  $v$  is the speed of propagation, as well known it results:

$$v = \lambda \nu$$

Eq. 96

$$\frac{c}{n} = \lambda \frac{\omega}{2\pi}$$

Eq. 97

and therefore:

$$\omega = \frac{2\pi c}{\lambda n}$$

Eq. 98

Moreover, given that:

$$\alpha^2 = \kappa^2 - \sigma^2; \quad \kappa = -\frac{n\Delta n k_0^2}{2\beta}; \quad \sigma = -\Delta\beta = \frac{k}{2} - \beta$$

Eq. 99

With:

$$k_0^2 = \frac{\omega^2}{c^2}; \quad \beta = \frac{2\pi n}{\lambda}$$

Eq. 100

We obtain that by expressing  $\kappa$  and  $\sigma$  as a function of the wavelength, one has:

$$\kappa = -\frac{\Delta n \pi}{\lambda n^2}; \quad \sigma = \frac{\pi}{\Lambda} - \frac{2\pi n}{\lambda}$$

Eq. 101

and then also:

$$\kappa^2 = \frac{\Delta n^2 \pi^2}{\lambda^2 n^4}; \quad \sigma^2 = \left( \frac{\pi}{\Lambda} - \frac{2\pi n}{\lambda} \right)^2; \quad \alpha = \frac{\pi}{\lambda} \sqrt{\frac{\Delta n^2}{n^4} - \frac{(\lambda - 2n\Lambda)^2}{\Lambda^2}}$$

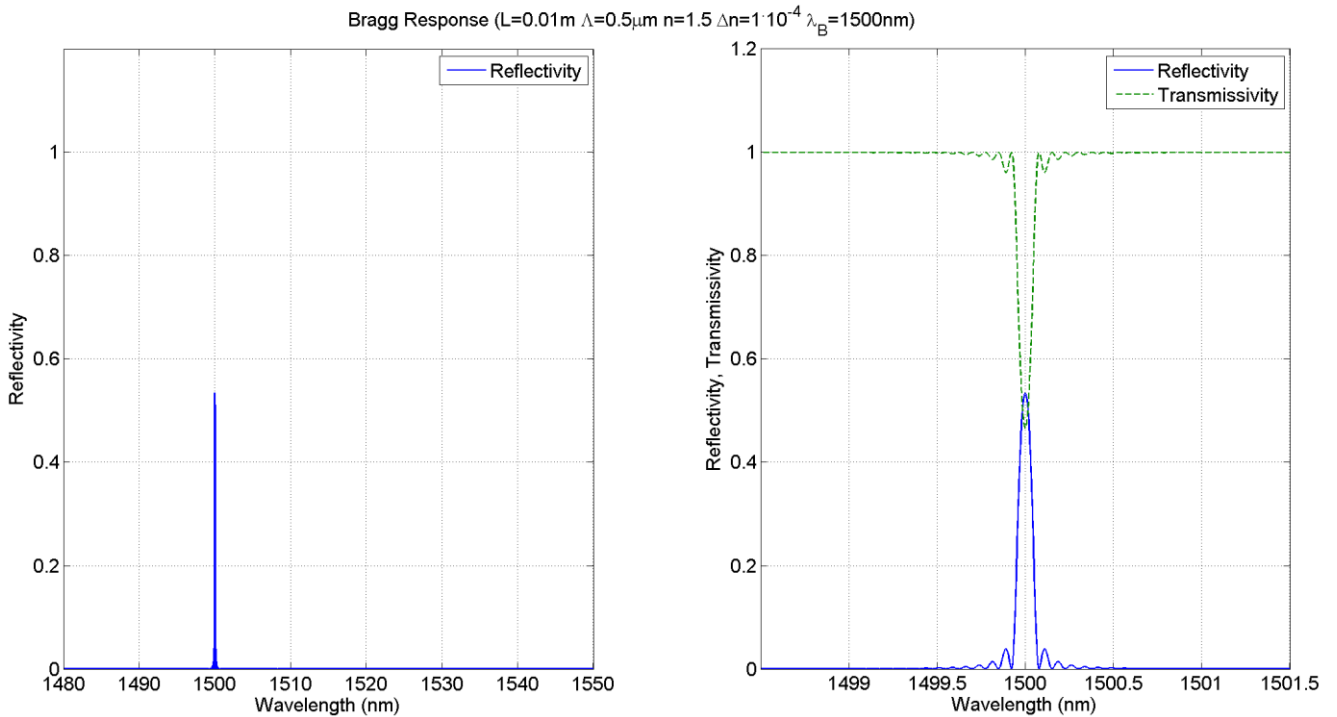
Eq. 102

### 2.5.1. NUMERICAL EVALUATION OF THE REFLECTIVITY FOR DIFFERENT GRATINGS

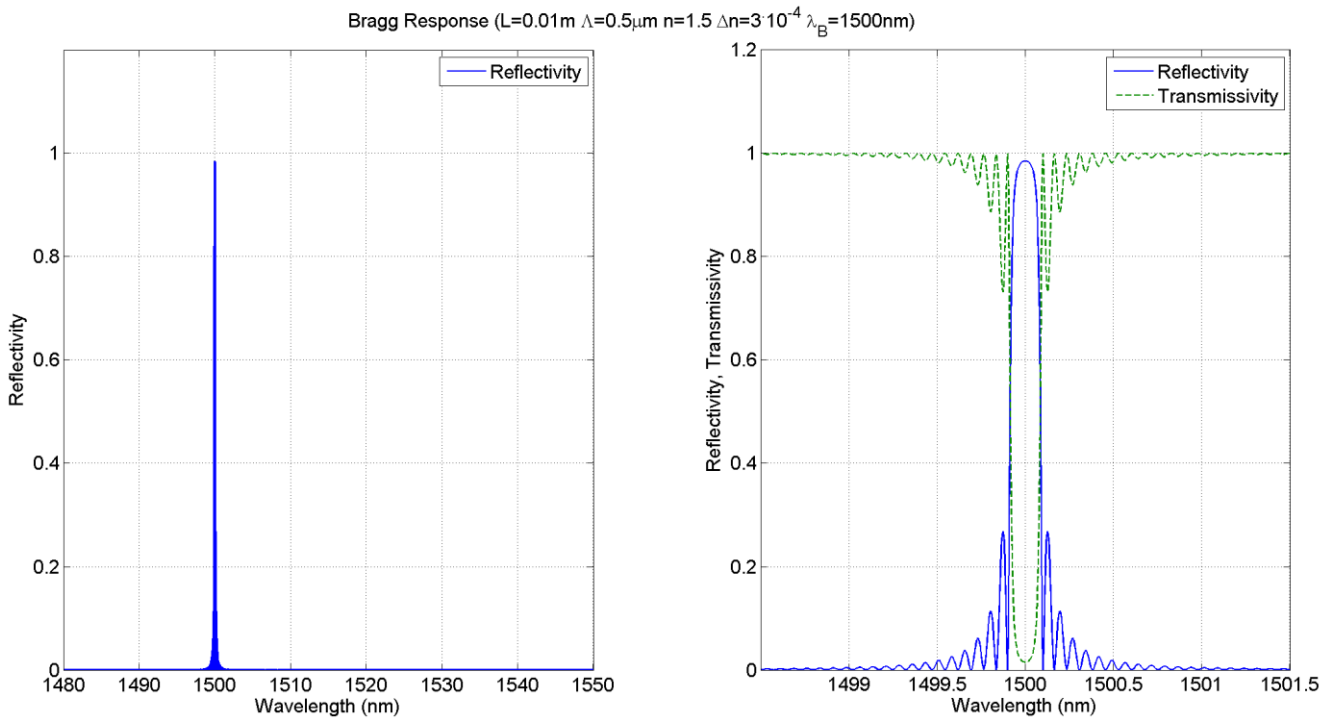
By substituting the Eq. 102 in the Eq. 93, the coefficients R and T can be easily evaluated as function of the wavelength  $\lambda$ ; the calculated R and T are plotted in the left side graphs of the Figure 23 for different values of  $\Delta n$ , where the right side graphs show instead a wavelength zoom for R and T; in the Figure 24 they are plotted instead for different values of the grating length L; in both the Figure 23 and the Figure 24 the Bragg wavelength  $\lambda_B$  is 1500 nm, since n and  $\Lambda$  have been taken respectively 1.5 and 0.5 $\mu\text{m}$ :

$$\lambda_B = 2n\Lambda = 2 * 1.5 * 0.5\mu\text{m} = 1500 \text{ nm} \quad \text{Eq. 103}$$

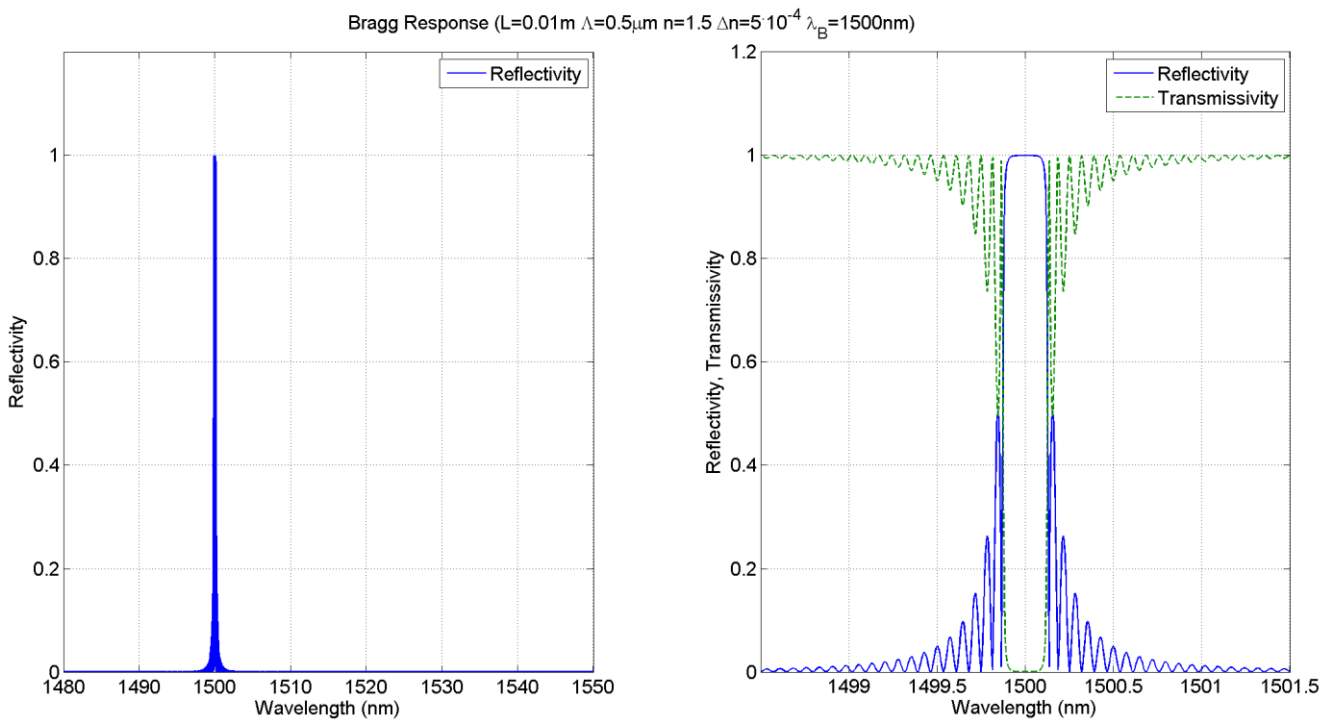
From the figures it's possible to see the main wavelength reflectivity peak, and the multiple secondary reflectivity peaks in the calculated spectrum. This kind of response is observed, with very good approximation, also in a real FBG reflectivity spectrum.



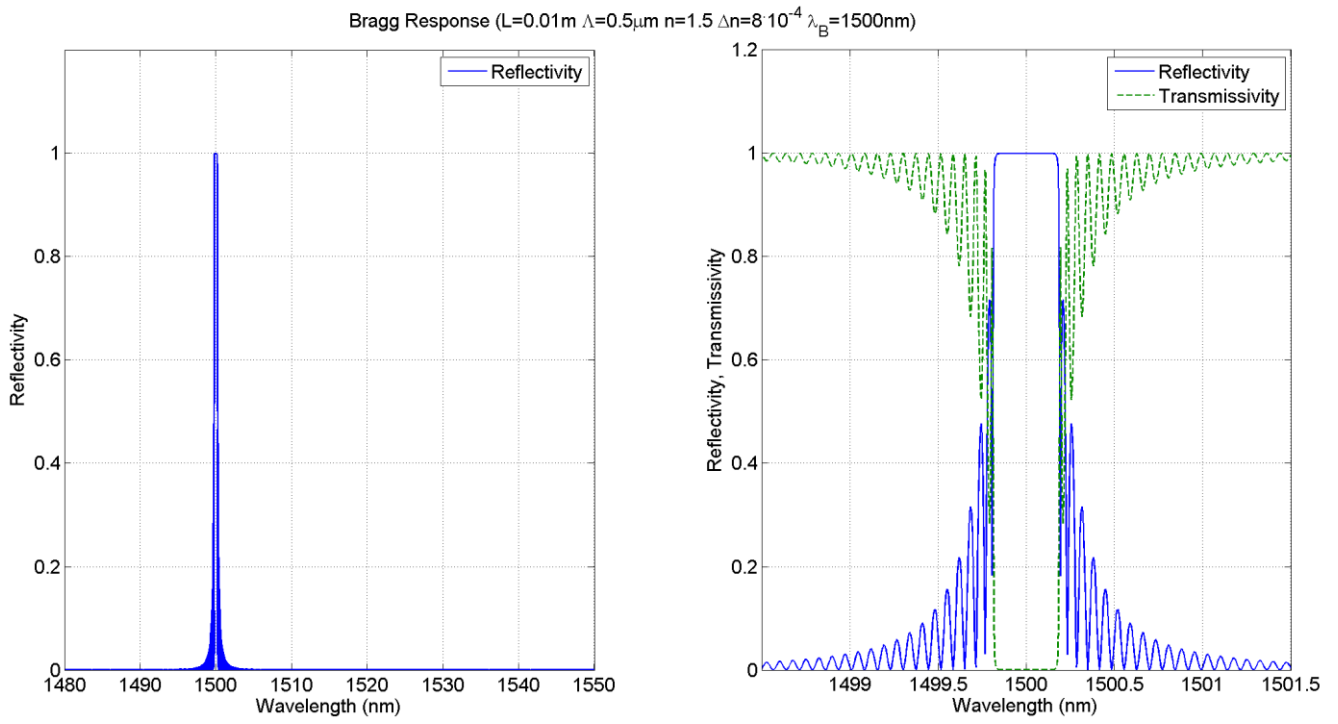
a)



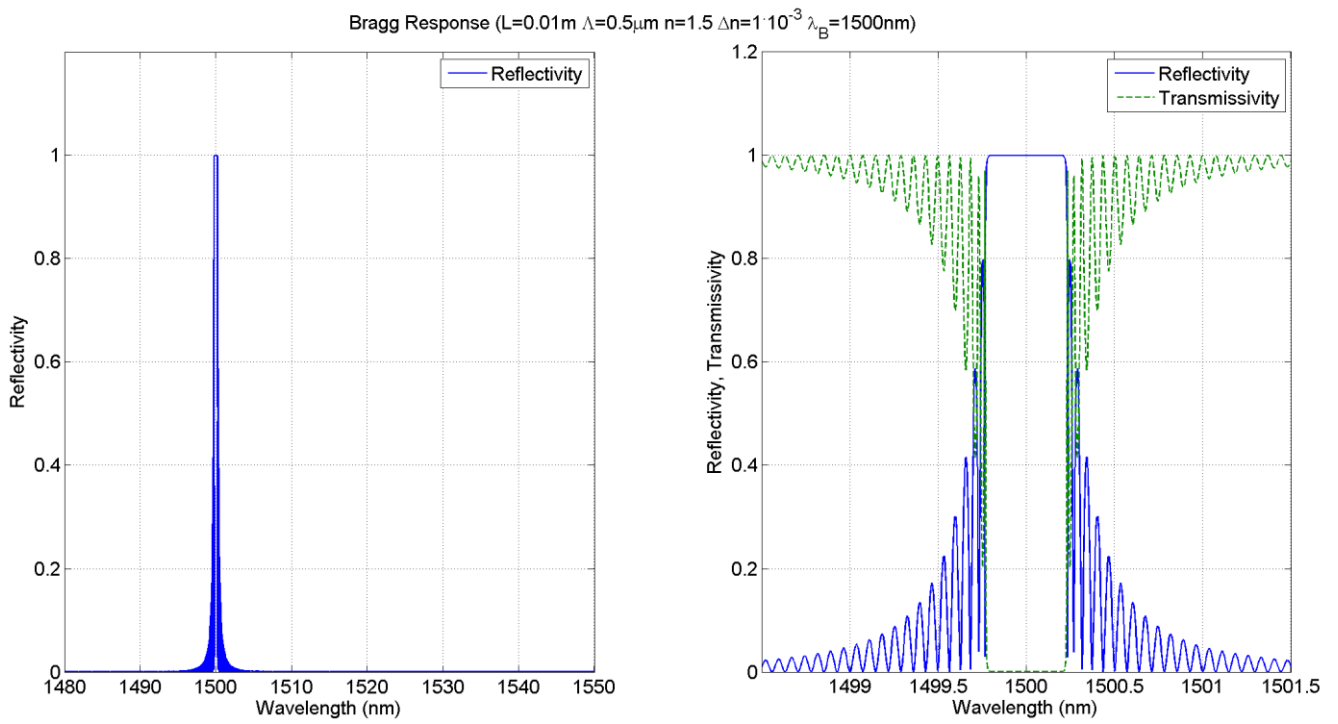
b)



c)



d)



e)

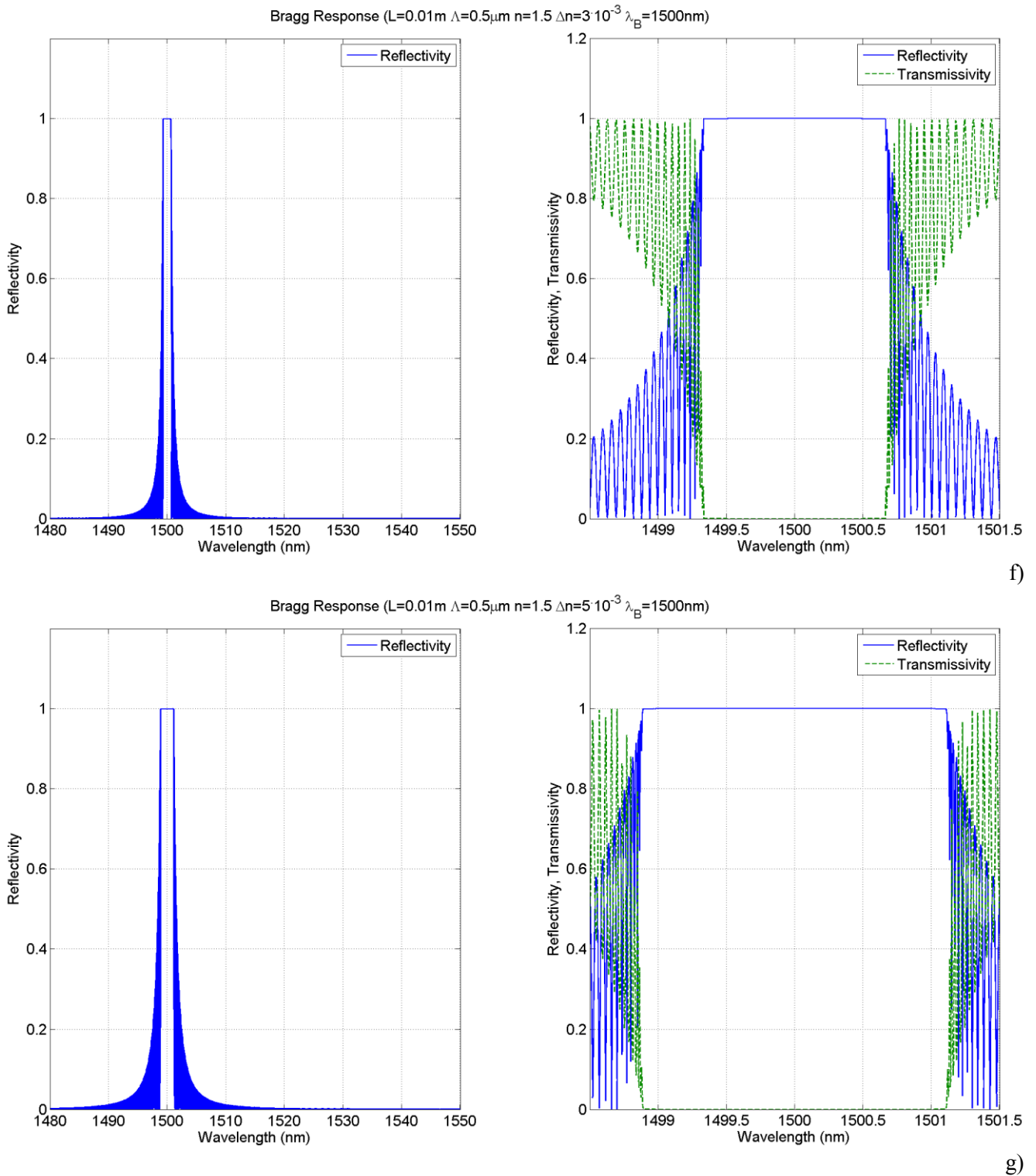
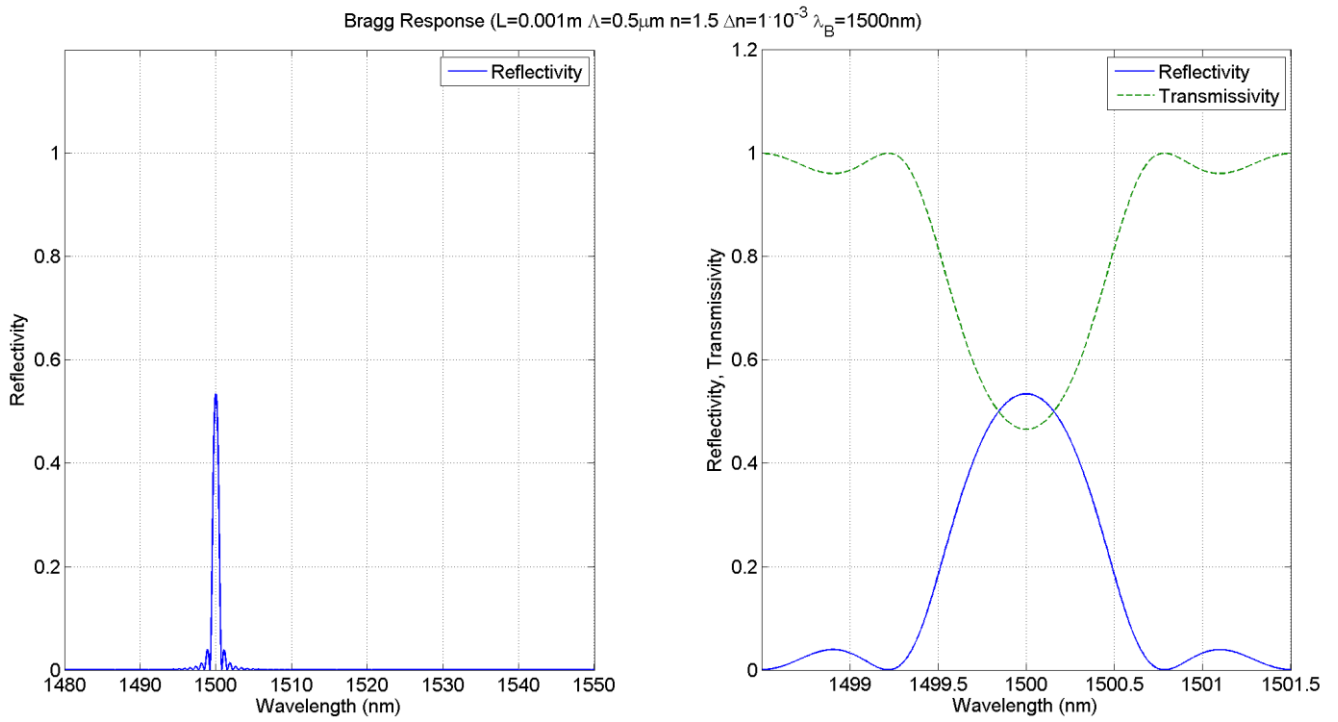
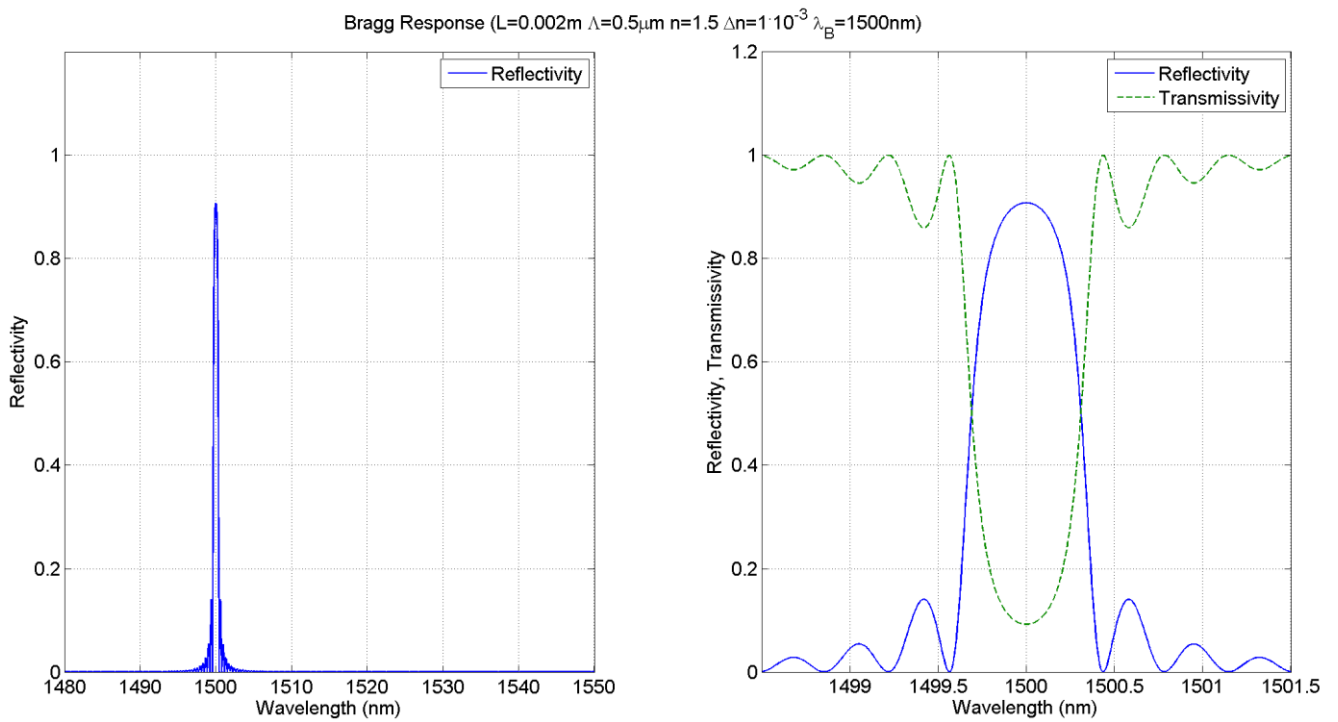


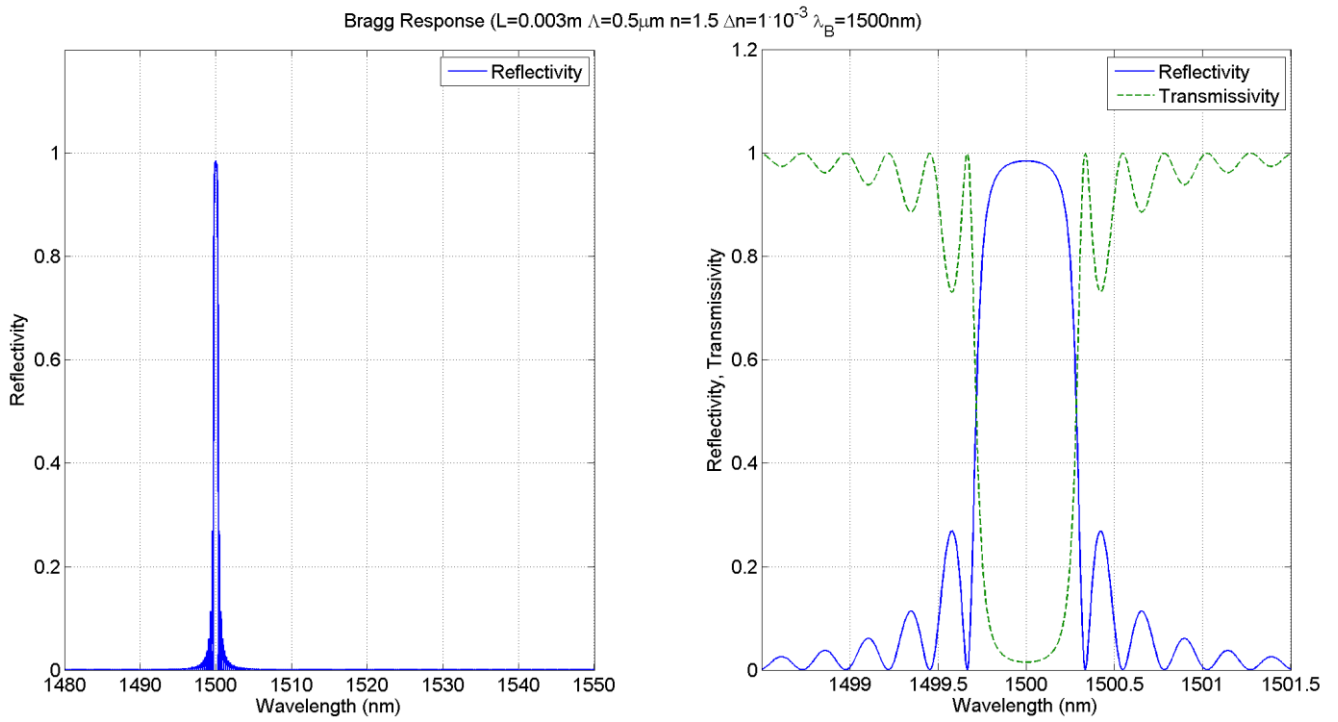
Figure 23 – Reflectivity and Transmissivity coefficients of Fiber Bragg Grating as function of the wavelength for different values of the amplitude of the refractive index perturbation  $\Delta n$



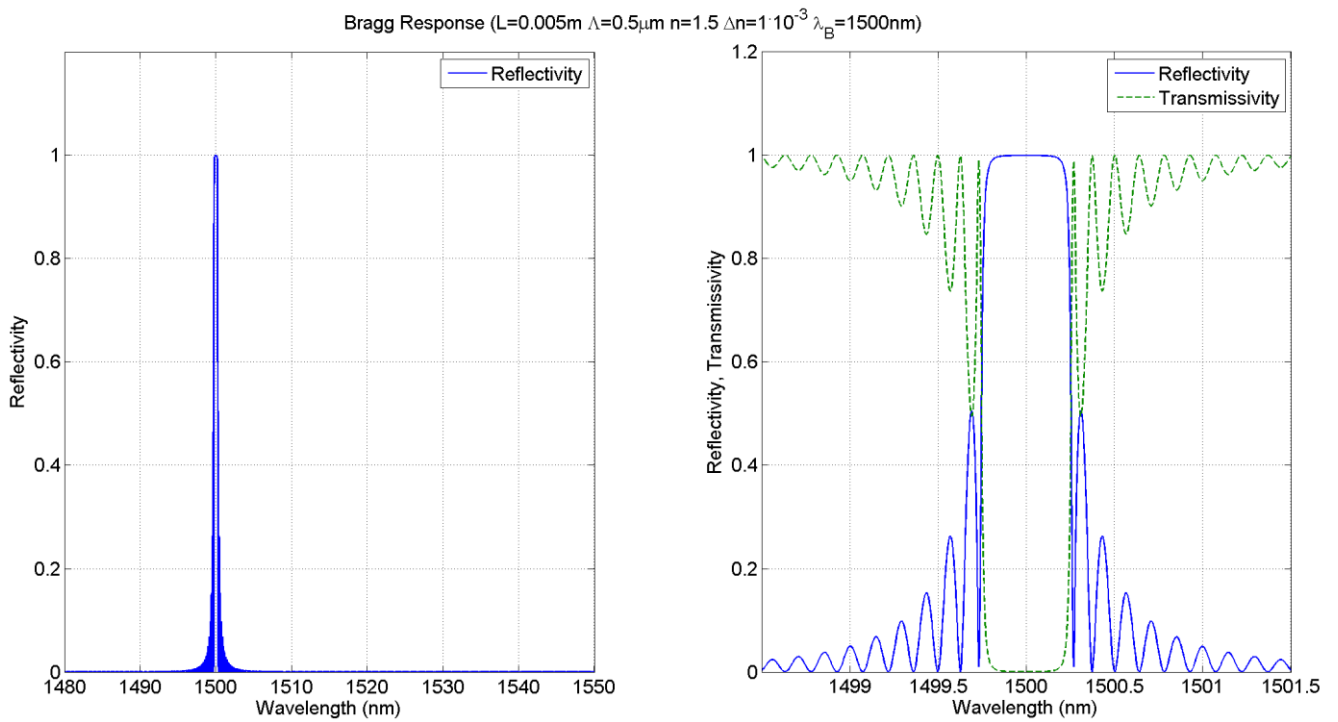
a)



b)



c)



d)

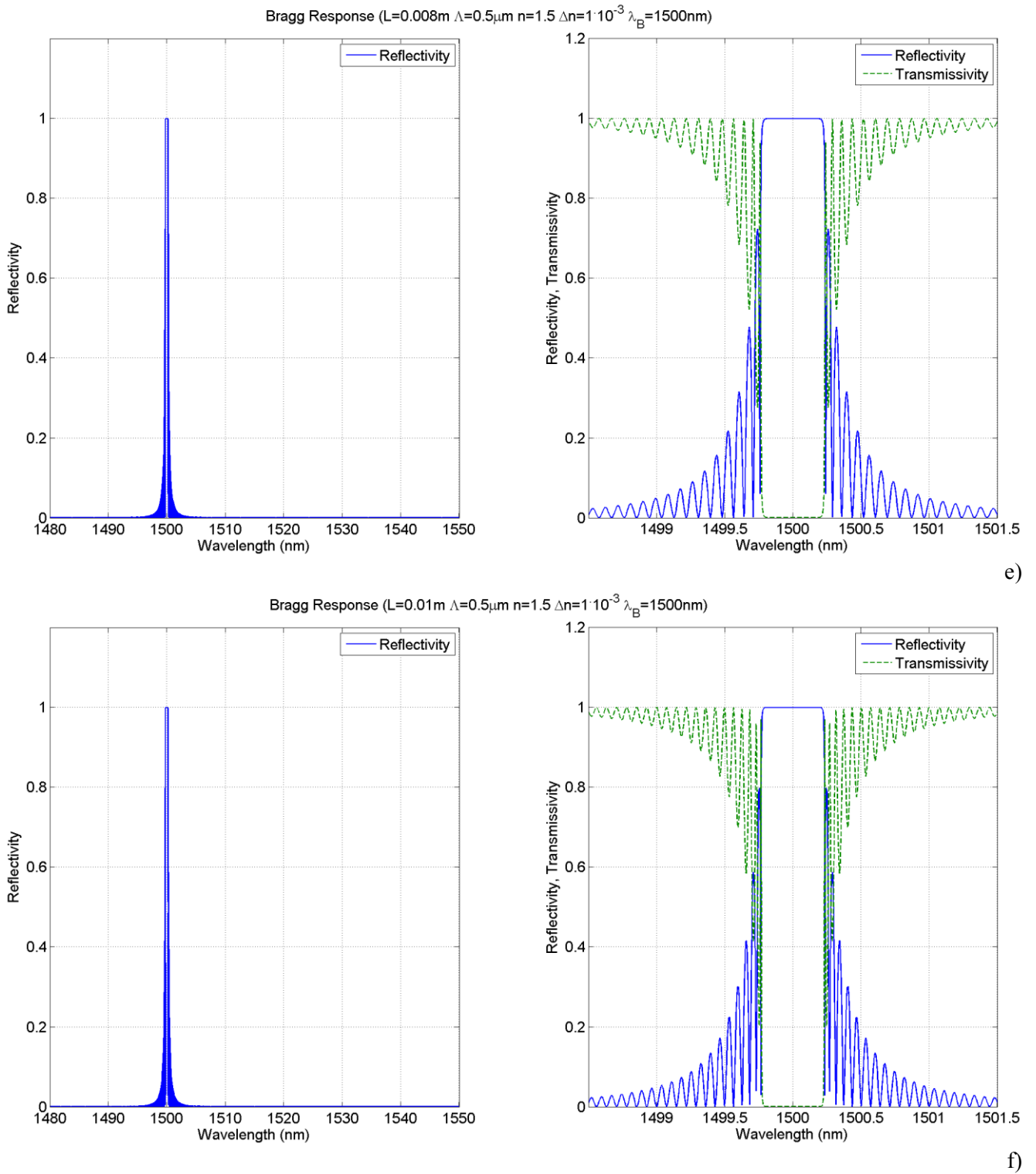


Figure 24 – Reflectivity and Transmissivity coefficients of Fiber Bragg Grating as function of the wavelength for different values of the grating length  $L$  (from 1 to 10mm)



# CHAPTER 3

## ACTIVE COATED FBG MECHANICAL ANALYSIS

### 3.1. FIBER BRAGG GRATING WAVELENGTH SHIFT

As showed in the previous section, the wavelength for which one has the maximum in reflectivity, i.e. the Bragg wavelength, is given by two times the product of the grating period for the refractive index of the medium. Therefore any change in the Bragg period or the refractive index caused by external factors such as variations of the temperature or strain experienced by the grating, will result in a shift of Bragg wavelength of the grating. This makes the Fiber Bragg gratings very suitable to be employed as sensors for strain or temperature measures. For this purpose an active coating material surrounding the optical grating, designed to have a large strain due to the physical quantity to measure, can be employed to increase the sensitivity of a Fiber Bragg Grating sensor. Indeed it's worth to consider that, generally, the sensitivity of a nude FBG is large enough only with respect to the strain variations, since they influence directly the grating period  $\Lambda$ .

---

A simple mathematical model can be employed in order to model the sensor wavelength shift. For this purpose the differential of the strain of a sample of length  $L$  must be introduced. It's defined as:

$$d\varepsilon = \frac{dL}{L} \quad \text{Eq. 104}$$

This relation can be integrated obtaining:

$$\int_{\varepsilon_0}^{\varepsilon} d\varepsilon = \int_{L_0}^L \frac{dL}{L} \quad \Rightarrow \quad \varepsilon = \ln\left(\frac{L}{L_0}\right) \quad \text{Eq. 105}$$

If the change in the length of the sample is small, generally it's possible to take:

$$\varepsilon = \ln\left(\frac{L}{L_0}\right) \approx \frac{\Delta L}{L_0} = \frac{L - L_0}{L_0} \quad \text{Eq. 106}$$

Here we can also assume:

$$L = \Lambda \quad \text{Eq. 107}$$

Obtaining therefore:

$$\varepsilon = \ln\left(\frac{\Lambda}{\Lambda_0}\right) \quad \text{Eq. 108}$$

Or, equivalently:

$$d\varepsilon = \frac{d\Lambda}{\Lambda} \quad \text{Eq. 109}$$

The thermal expansion coefficient of a material is defined as the rate of the variation of the strain respect to the temperature change; so we can write:

---

$$\alpha(T) = \frac{d\varepsilon}{dT} \quad \Rightarrow \quad \alpha = \frac{d}{dT} \ln\left(\frac{\Lambda}{\Lambda_0}\right) \quad \text{Eq. 110}$$

Now the wavelength  $\lambda$  reflected by the bragg is proportional to the grating period  $\Lambda$ ; differentiating therefore the Eq. 5 :

$$\lambda = 2n\Lambda \quad \text{Eq. 111}$$

We obtain:

$$d\lambda = 2(\Lambda dn + nd\Lambda) \quad \text{Eq. 112}$$

Furthermore it must be considered that the fiber refractive index has a dependence by the temperature (thermo – optic effect) and the strain (photo – elastic effect); so we have:

$$n = n(T, \Lambda) \quad \text{Eq. 113}$$

which implies:

$$d\lambda = 2 \left[ \Lambda \left( \frac{\partial n}{\partial T} dT + \frac{\partial n}{\partial \Lambda} d\Lambda \right) + nd\Lambda \right] \quad \text{Eq. 114}$$

$$d\lambda = 2 \left[ \Lambda \frac{\partial n}{\partial T} dT + \left( \Lambda \frac{\partial n}{\partial \Lambda} + n \right) d\Lambda \right] \quad \text{Eq. 115}$$

Dividing all for  $\lambda = 2n\Lambda$ , one obtains:

$$\frac{d\lambda}{\lambda} = \frac{\Lambda n_T dT + (\Lambda n_\Lambda + n) d\Lambda}{n\Lambda} \quad \text{with: } n_T = \frac{\partial n}{\partial T} \quad \text{and } n_\Lambda = \frac{\partial n}{\partial \Lambda} \quad \text{Eq. 116}$$

But since  $d\varepsilon_f = d\Lambda/\Lambda$ , where  $\varepsilon_f$  is the fiber strain, it results:

---

$$\frac{d\lambda}{\lambda} = \frac{n_T}{n} dT + \frac{\Lambda n_\Lambda + n}{n} d\varepsilon_f \quad \text{Eq. 117}$$

If we define the thermo optical coefficient  $\xi$  as:

$$\xi = \frac{1}{n} \frac{\partial n}{\partial T} \quad \text{Eq. 118}$$

and the photo elastic coefficient  $p_e$  as:

$$p_e = -\frac{\Lambda}{n} \frac{\partial n}{\partial \Lambda} \quad \text{Eq. 119}$$

we can then write:

$$\frac{d\lambda}{\lambda} = \xi dT + (1 - p_e) d\varepsilon_f \quad \text{Eq. 120}$$

If a free sensor behavior can be assumed (i.e. sensor not subject to external forces and/or constraints), we have consequentially that the strain  $\varepsilon_f$  depends only by the sensor temperature:

$$\varepsilon_f = \varepsilon_f(T) \quad \text{Eq. 121}$$

For a coated FBG a mechanical analysis of the thermal stress and strain inside both the optical fiber and coating is needed and it will be carried out in to following section.

### 3.2. MECHANICAL BEHAVIOR OF THE ACTIVE COATED FBG

The mechanical behavior of the Active Coated FBG (see Figure 25) can be modeled by considering the mechanical equilibrium equations and the temperature dependent stress strain constitutive relations of the involved materials for the active coating and the silica optical fiber.

---

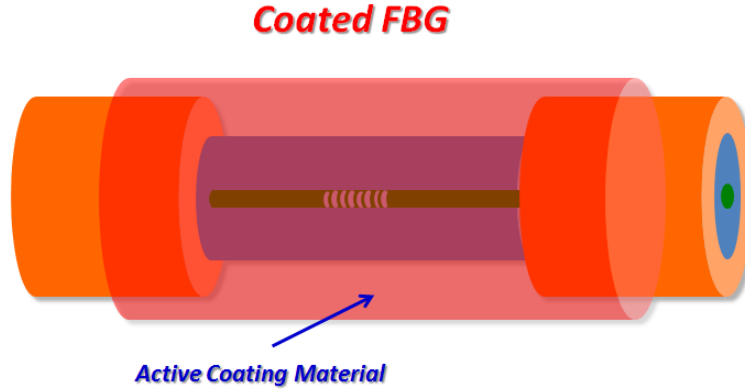


*Figure 25 – Active Coated FBG*

The equations can be efficiently solved in a cylindrical coordinate system having the z-axis directed along the axis of the Active Coated FBG. In cylindrical coordinate the strain components for both the glass fiber and the Coating can be written as:

$$\varepsilon_r = \frac{\partial u_r}{\partial r} \quad \varepsilon_\theta = \frac{1}{r} \frac{\partial u_\theta}{\partial \theta} + \frac{u_r}{r} \quad \varepsilon_z = \frac{\partial u_z}{\partial z} \quad \text{Eq. 122}$$

$$\gamma_{r\theta} = \frac{1}{r} \frac{\partial u_r}{\partial \theta} + r \frac{\partial}{\partial r} \left( \frac{u_\theta}{r} \right) \quad \gamma_{rz} = \frac{\partial u_z}{\partial r} + \frac{\partial u_r}{\partial z} \quad \gamma_{\theta z} = \frac{\partial u_\theta}{\partial z} + \frac{1}{r} \frac{\partial u_z}{\partial \theta} \quad \text{Eq. 123}$$

Where  $u_r$ ,  $u_\theta$  and  $u_z$  represent the components of the displacement field in cylindrical coordinates and  $r$ ,  $\theta$  and  $z$  are respectively the radial, angular and axial coordinate. Due to the geometrical axial-symmetry around the z-axis, the components of the displacements are independent by the  $\theta$  coordinate and therefore they can be expressed as:

$$u_r = u_r(r, z) \quad u_\theta = u_\theta(r, z) \quad u_z = u_z(r, z) \quad \text{Eq. 124}$$

Thus, cancelling the terms containing the derivatives with respect to  $\theta$ , the total strain can be simplified as it follows:

$$\varepsilon_r = \frac{\partial u_r}{\partial r} \quad \varepsilon_\theta = \frac{u_r}{r} \quad \varepsilon_z = \frac{\partial u_z}{\partial z} \quad \text{Eq. 125}$$

$$\gamma_{r\theta} = r \frac{\partial}{\partial r} \left( \frac{u_\theta}{r} \right) \quad \gamma_{rz} = \frac{\partial u_z}{\partial r} + \frac{\partial u_r}{\partial z} \quad \gamma_{\theta z} = \frac{\partial u_\theta}{\partial z} \quad \text{Eq. 126}$$

As well known, from these components the strain tensor can be written as:

$$[\varepsilon] = \begin{pmatrix} \varepsilon_r & \gamma_{r\theta}/2 & \gamma_{rz}/2 \\ \gamma_{r\theta}/2 & \varepsilon_\theta & \gamma_{\theta z}/2 \\ \gamma_{rz}/2 & \gamma_{\theta z}/2 & \varepsilon_z \end{pmatrix} \quad \text{Eq. 127}$$

While the stress tensor is:

$$[\sigma] = \begin{pmatrix} \sigma_{rr} & \tau_{r\theta} & \tau_{rz} \\ \tau_{r\theta} & \sigma_{\theta\theta} & \tau_{\theta z} \\ \tau_{rz} & \tau_{\theta z} & \sigma_{zz} \end{pmatrix} \quad \text{Eq. 128}$$

In order to calculate the temporal evolution of the local stress, the equilibrium equations must be imposed. In Cartesian coordinates it must be:

$$\nabla \cdot [\sigma] + [b] = \rho \frac{\partial^2}{\partial t^2} [u] \quad \text{Eq. 129}$$

$$[b] = \begin{bmatrix} b_x \\ b_y \\ b_z \end{bmatrix} \quad \frac{\partial^2}{\partial t^2} [u] = \begin{bmatrix} \ddot{u}_x \\ \ddot{u}_y \\ \ddot{u}_z \end{bmatrix} \quad \text{Eq. 130}$$

Where  $[\sigma]$  is the stress tensor,  $[b]$  are the body force,  $\rho$  is the density,  $[u]$  is the displacement field  $[\ddot{u}]$  is the local acceleration,  $\rho[\ddot{u}]$  is the inertial term, and  $\nabla$  is the nabla operator:

$$\nabla = \left[ \frac{\partial}{\partial x} \quad \frac{\partial}{\partial y} \quad \frac{\partial}{\partial z} \right] \quad \text{Eq. 131}$$

Since the body forces  $[b]$  and the inertial term can be neglected one has:

$$\nabla \cdot [\sigma] = 0 \quad \text{Eq. 132}$$

Or equivalently:

$$\nabla \cdot \begin{pmatrix} \sigma_{xx} \tau_{xy} \tau_{xz} \\ \tau_{xy} \sigma_{yy} \tau_{yz} \\ \tau_{xz} \tau_{yz} \sigma_{zz} \end{pmatrix} = 0 \quad \text{Eq. 133}$$

In components this yields:

$$\frac{\partial \sigma_{xx}}{\partial x} + \frac{\partial \tau_{xy}}{\partial y} + \frac{\partial \tau_{xz}}{\partial z} = 0 \quad \text{Eq. 134}$$

$$\frac{\partial \sigma_{xx}}{\partial x} + \frac{\partial \tau_{xy}}{\partial y} + \frac{\partial \tau_{xz}}{\partial z} = 0 \quad \text{Eq. 135}$$

$$\frac{\partial \sigma_{xx}}{\partial x} + \frac{\partial \tau_{xy}}{\partial y} + \frac{\partial \tau_{xz}}{\partial z} = 0 \quad \text{Eq. 136}$$

in cylindrical coordinates, the same equations become:

$$\frac{\partial \sigma_r}{\partial r} + \frac{1}{r} \frac{\partial \tau_{r\theta}}{\partial \theta} + \frac{\partial \tau_{rz}}{\partial z} + \frac{\sigma_r - \sigma_\theta}{r} = 0 \quad \text{Eq. 137}$$

$$\frac{\partial \tau_{r\theta}}{\partial r} + \frac{1}{r} \frac{\partial \sigma_\theta}{\partial \theta} + \frac{\partial \tau_{\theta z}}{\partial z} + 2 \frac{\tau_{r\theta}}{r} = 0 \quad \text{Eq. 138}$$

$$\frac{\partial \tau_{rz}}{\partial r} + \frac{1}{r} \frac{\partial \tau_{\theta z}}{\partial \theta} + \frac{\partial \sigma_z}{\partial z} + \frac{\tau_{rz}}{r} = 0 \quad \text{Eq. 139}$$

Due to the axial-symmetry around the z-axis of both geometry and loads, which involves the cancellation of the term containing the derivative with respect to the  $\theta$  coordinate, they can be simplified as it follows:

$$\frac{\partial \sigma_r}{\partial r} + \frac{\partial \tau_{rz}}{\partial z} + \frac{\sigma_r - \sigma_\theta}{r} = 0 \quad \text{Eq. 140}$$

$$\frac{\partial \tau_{r\theta}}{\partial r} + \frac{\partial \tau_{\theta z}}{\partial z} + 2 \frac{\tau_{r\theta}}{r} = 0 \quad \text{Eq. 141}$$

$$\frac{\partial \tau_{rz}}{\partial r} + \frac{\partial \sigma_z}{\partial z} + \frac{\tau_{rz}}{r} = 0 \quad \text{Eq. 142}$$

Furthermore it must be considered that assuming the absence of any angular torsion, the component of the tangential stress directed along  $\theta$  can be considered null:

$$\tau_{r\theta} = 0 \quad \text{Eq. 143}$$

$$\tau_{z\theta} = \tau_{\theta z} = 0 \quad \text{Eq. 144}$$

thus the Eq. 141 is identically verified and the equilibrium equation system reduced to:

$$\frac{\partial \sigma_r}{\partial r} + \frac{\partial \tau_{rz}}{\partial z} + \frac{\sigma_r - \sigma_\theta}{r} = 0 \quad \text{Eq. 145}$$

$$\frac{\partial \tau_{rz}}{\partial r} + \frac{\partial \sigma_z}{\partial z} + \frac{\tau_{rz}}{r} = 0 \quad \text{Eq. 146}$$

### 3.3. CONSTITUTIVE EQUATION OF THE MATERIALS

On the other hand, since the glass fiber present an isotropic behavior, the stress-strain constitutive relations can be written as:

$$\begin{bmatrix} \varepsilon_r^{el} \\ \varepsilon_\theta^{el} \\ \varepsilon_z^{el} \\ \gamma_{r\theta}^{el} \\ \gamma_{rz}^{el} \\ \gamma_{\theta z}^{el} \end{bmatrix} = \begin{pmatrix} 1/E_f & -\nu_f/E_f & -\nu_f/E_f & 0 & 0 & 0 \\ -\nu_f/E_f & 1/E_f & -\nu_f/E_f & 0 & 0 & 0 \\ -\nu_f/E_f & -\nu_f/E_f & 1/E_f & 0 & 0 & 0 \\ 0 & 0 & 0 & 1/G_f & 0 & 0 \\ 0 & 0 & 0 & 0 & 1/G_f & 0 \\ 0 & 0 & 0 & 0 & 0 & 1/G_f \end{pmatrix} \begin{bmatrix} \sigma_r \\ \sigma_\theta \\ \sigma_z \\ \tau_{r\theta} \\ \tau_{rz} \\ \tau_{\theta z} \end{bmatrix} \quad \text{Eq. 147}$$

Where  $\nu_f$  is the fiber Poisson ratio,  $E_f$  is the fiber elastic modulus,  $G_f$  is fiber shear modulus and the superscript  $el$  indicate the elastic component of the strain; similary for an isotropic coating it's possible to write:

$$\begin{bmatrix} \varepsilon_r^{el} \\ \varepsilon_\theta^{el} \\ \varepsilon_z^{el} \\ \gamma_{r\theta}^{el} \\ \gamma_{rz}^{el} \\ \gamma_{\theta z}^{el} \end{bmatrix} = \begin{pmatrix} 1/E_c & -\nu_c/E_c & -\nu_c/E_c & 0 & 0 & 0 \\ -\nu_c/E_c & 1/E_c & -\nu_c/E_c & 0 & 0 & 0 \\ -\nu_c/E_c & -\nu_c/E_c & 1/E_c & 0 & 0 & 0 \\ 0 & 0 & 0 & 1/G_c & 0 & 0 \\ 0 & 0 & 0 & 0 & 1/G_c & 0 \\ 0 & 0 & 0 & 0 & 0 & 1/G_c \end{pmatrix} \begin{bmatrix} \sigma_r \\ \sigma_\theta \\ \sigma_z \\ \tau_{r\theta} \\ \tau_{rz} \\ \tau_{\theta z} \end{bmatrix} \quad \text{Eq. 148}$$

with  $\nu_c$  coating Poisson ratio,  $E_c$  the coating elastic modulus and  $G_c$  coating shear modulus; for an isotropic material it also results:

$$G = \frac{E}{2(1 + \nu)} \quad \text{Eq. 149}$$

Of course the elastic component of the strain are given by:

$$\begin{bmatrix} \varepsilon_r^{el} \\ \varepsilon_\theta^{el} \\ \varepsilon_z^{el} \\ \gamma_{r\theta}^{el} \\ \gamma_{rz}^{el} \\ \gamma_{\theta z}^{el} \end{bmatrix} = \begin{bmatrix} \varepsilon_r^{tot} \\ \varepsilon_\theta^{tot} \\ \varepsilon_z^{tot} \\ \gamma_{r\theta}^{tot} \\ \gamma_{rz}^{tot} \\ \gamma_{\theta z}^{tot} \end{bmatrix} - \begin{bmatrix} \varepsilon_r^{th} \\ \varepsilon_\theta^{th} \\ \varepsilon_z^{th} \\ \gamma_{r\theta}^{th} \\ \gamma_{rz}^{th} \\ \gamma_{\theta z}^{th} \end{bmatrix} - \begin{bmatrix} \varepsilon_r^{sw} \\ \varepsilon_\theta^{sw} \\ \varepsilon_z^{sw} \\ \gamma_{r\theta}^{sw} \\ \gamma_{rz}^{sw} \\ \gamma_{\theta z}^{sw} \end{bmatrix} \quad \text{Eq. 150}$$

In the Eq. 150 the superscript th indicate the thermal fraction of the strain (due to the thermal expansion) while the superscript sw indicate the swelling fraction of the strain (due, for example, to the absorbed humidity; this term can be neglected for the glass fiber). Both the thermal and swelling aliquot of the total strain, caused by the temperature variations and absorbed humidity, can be considered inelastic strains. Therefore, since any stress cause only elastic strain, they must be subtract by the total strain (expressed by the Eq. 125, Eq. 126) in the constitutive relations of the materials, Eq. 147 and Eq. 148. Moreover, for isotropic materials they can be respectively expressed as:

---

$$\begin{bmatrix} \varepsilon_r^{th} \\ \varepsilon_\theta^{th} \\ \varepsilon_z^{th} \\ \gamma_{r\theta}^{th} \\ \gamma_{rz}^{th} \\ \gamma_{\theta z}^{th} \end{bmatrix} = \begin{bmatrix} \alpha \\ \alpha \\ \alpha \\ 0 \\ 0 \\ 0 \end{bmatrix} (T - T_{ref}) \quad \text{Eq. 151}$$

Where  $\alpha$  is the thermal expansion coefficient of the material,  $T$  is the temperature and  $T_{ref}$  is the reference temperature (for which the thermal strain is assumed null); and similarly:

$$\begin{bmatrix} \varepsilon_r^{sw} \\ \varepsilon_\theta^{sw} \\ \varepsilon_z^{sw} \\ \gamma_{r\theta}^{sw} \\ \gamma_{rz}^{sw} \\ \gamma_{\theta z}^{sw} \end{bmatrix} = \begin{bmatrix} \beta \\ \beta \\ \beta \\ 0 \\ 0 \\ 0 \end{bmatrix} (RH - RH_{ref}) \quad \text{Eq. 152}$$

Where  $\beta$  is the swelling coefficient of the material,  $RH$  is the Humidity and  $RH_{ref}$  is the reference Humidity (for which the swelling strain is assumed null). If the thermal transitory and the mass transport phenomena can be considered fast enough, the Temperature and the Humidity can be considered independent of the position and given by the external environment values in which the sensor is placed.

### 3.4. BOUNDARY CONDITIONS

In order to determine the stress and strain fields, the boundary conditions on the external surface of the coating must be imposed; they can be written considering that the stress components are null on the whole external surface of the coating. Defined  $r_{ce}$  as the external radius of the coating, it must result:

$$\sigma_r(r_{ce}, z) = 0 \quad \text{Eq. 153}$$

$$\tau_{rz}(r_{ce}, z) = 0 \quad \text{Eq. 154}$$

Similarly, on the top and bottom surfaces of the fiber and the coating, since they are stress-free too, the boundary conditions are:

$$\sigma_z(r, \pm L/2) = 0 \quad \text{Eq. 155}$$

$$\tau_{rz}(r, \pm L/2) = 0 \quad \text{Eq. 156}$$

Where  $L$  is the full length of the coating along the  $z$ -axis. Finally it must be also considered that on the surface separating the fiber zone from the coating zone the  $z$  and  $\theta$  components of the strain and the radial and tangential components of the stress must be the same for every value of the  $z$  coordinate. If  $r_{ci}$  is the internal radius of the coating, it must be therefore:

$$\varepsilon_{zf}(r_{ci}, z) = \varepsilon_{zc}(r_{ci}, z) \quad \text{Eq. 157}$$

$$\varepsilon_{\theta f}(r_{ci}, z) = \varepsilon_{\theta c}(r_{ci}, z) \quad \text{Eq. 158}$$

$$\sigma_{rf}(r_{ci}, z) = \sigma_{rc}(r_{ci}, z) \quad \text{Eq. 159}$$

$$\tau_{rzf}(r_{ci}, z) = \tau_{rzc}(r_{ci}, z) \quad \text{Eq. 160}$$

### 3.5. STRESS FUNCTION

In order to solve the equilibrium equation system Eq. 145, Eq. 146:

$$\frac{\partial \sigma_r}{\partial r} + \frac{\partial \tau_{rz}}{\partial z} + \frac{\sigma_r - \sigma_\theta}{r} = 0 \quad \text{Eq. 161}$$

---

$$\frac{\partial \tau_{rz}}{\partial r} + \frac{\partial \sigma_z}{\partial z} + \frac{\tau_{rz}}{r} = 0 \quad \text{Eq. 162}$$

As showed in [5], we can introduce a stress function  $\phi$  such that:

$$\sigma_r = \frac{\partial}{\partial z} \left( \nu \nabla^2 \phi - \frac{\partial^2 \phi}{\partial r^2} \right) \quad \text{Eq. 163}$$

$$\sigma_\theta = \frac{\partial}{\partial z} \left( \nu \nabla^2 \phi - \frac{1}{r} \frac{\partial \phi}{\partial r} \right) \quad \text{Eq. 164}$$

$$\sigma_z = \frac{\partial}{\partial z} \left[ (2 - \nu) \nabla^2 \phi - \frac{\partial^2 \phi}{\partial z^2} \right] \quad \text{Eq. 165}$$

$$\tau_{rz} = \frac{\partial}{\partial r} \left[ (1 - \nu) \nabla^2 \phi - \frac{\partial^2 \phi}{\partial z^2} \right] \quad \text{Eq. 166}$$

With the Laplacian  $\nabla^2$  that in cylindrical coordinates is given by:

$$\nabla^2 = \frac{\partial^2}{\partial r^2} + \frac{1}{r} \frac{\partial}{\partial r} + \frac{1}{r^2} \frac{\partial^2}{\partial \theta^2} + \frac{\partial^2}{\partial z^2} \quad \text{Eq. 167}$$

For the Axial symmetry around the z axis, which comports that the derivatives with respect the angular coordinate  $\theta$  is null, the Laplacian reduces to:

$$\nabla^2 = \frac{\partial^2}{\partial r^2} + \frac{1}{r} \frac{\partial}{\partial r} + \frac{\partial^2}{\partial z^2} \quad \text{Eq. 168}$$

By substituting the Eq. 163 - Eq. 166 into the Eq. 161, Eq. 162, we have:

$$\frac{\partial}{\partial r} \frac{\partial}{\partial z} \left( \nu \nabla^2 \phi - \frac{\partial^2 \phi}{\partial r^2} \right) + \frac{\partial}{\partial z} \frac{\partial}{\partial r} \left[ (1 - \nu) \nabla^2 \phi - \frac{\partial^2 \phi}{\partial z^2} \right] + \frac{1}{r} \frac{\partial}{\partial z} \left( \frac{1}{r} \frac{\partial \phi}{\partial r} - \frac{\partial^2 \phi}{\partial r^2} \right) = 0 \quad \text{Eq. 169}$$

$$\frac{\partial^2}{\partial r^2} \left[ (1 - \nu) \nabla^2 \phi - \frac{\partial^2 \phi}{\partial z^2} \right] + \frac{\partial^2}{\partial z^2} \left[ (2 - \nu) \nabla^2 \phi - \frac{\partial^2 \phi}{\partial z^2} \right] + \frac{1}{r} \frac{\partial}{\partial r} \left[ (1 - \nu) \nabla^2 \phi - \frac{\partial^2 \phi}{\partial z^2} \right] = 0 \quad \text{Eq. 170}$$

Simplifying the  $\nu \nabla^2 \phi$  terms in the first equation, and rewriting, in the second one:

$$(2 - \nu) \nabla^2 \phi = \nabla^2 \phi + (1 - \nu) \nabla^2 \phi \quad \text{Eq. 171}$$

We obtain:

$$\frac{\partial}{\partial r} \frac{\partial}{\partial z} \left( -\frac{\partial^2 \phi}{\partial r^2} \right) + \frac{\partial}{\partial z} \frac{\partial}{\partial r} \left[ \nabla^2 \phi - \frac{\partial^2 \phi}{\partial z^2} \right] + \frac{1}{r} \frac{\partial}{\partial z} \left( \frac{1}{r} \frac{\partial \phi}{\partial r} - \frac{\partial^2 \phi}{\partial r^2} \right) = 0 \quad \text{Eq. 172}$$

$$\frac{\partial^2}{\partial r^2} \left[ (1 - \nu) \nabla^2 \phi - \frac{\partial^2 \phi}{\partial z^2} \right] + \frac{\partial^2}{\partial z^2} \left[ \nabla^2 \phi + (1 - \nu) \nabla^2 \phi - \frac{\partial^2 \phi}{\partial z^2} \right] + \frac{1}{r} \frac{\partial}{\partial r} \left[ (1 - \nu) \nabla^2 \phi - \frac{\partial^2 \phi}{\partial z^2} \right] = 0 \quad \text{Eq. 173}$$

Grouping the terms to be derived with respect to the z coordinate in the first equation and evidencing, in the second one, the quantity  $[(1 - \nu) \nabla^2 \phi - \partial^2 \phi / \partial z^2]$  we have:

$$\frac{\partial}{\partial z} \left( \frac{\partial}{\partial r} \left[ \nabla^2 \phi - \frac{\partial^2 \phi}{\partial z^2} - \frac{\partial^2 \phi}{\partial r^2} \right] + \frac{1}{r} \left( \frac{1}{r} \frac{\partial \phi}{\partial r} - \frac{\partial^2 \phi}{\partial r^2} \right) \right) = 0 \quad \text{Eq. 174}$$

$$\left( \frac{\partial^2}{\partial r^2} + \frac{1}{r} \frac{\partial}{\partial r} + \frac{\partial^2}{\partial z^2} \right) \left[ (1 - \nu) \nabla^2 \phi - \frac{\partial^2 \phi}{\partial z^2} \right] + \frac{\partial^2}{\partial z^2} \nabla^2 \phi \quad \text{Eq. 175}$$

Furthermore, since:

$$\frac{1}{r} \left( \frac{1}{r} \frac{\partial \phi}{\partial r} - \frac{\partial^2 \phi}{\partial r^2} \right) = \frac{\partial}{\partial r} \left( -\frac{1}{r} \frac{\partial \phi}{\partial r} \right) \quad \text{Eq. 176}$$

recognizing the Laplacian operator  $\nabla^2$  in the second equation, we get:

$$\frac{\partial}{\partial z} \left( \frac{\partial}{\partial r} \left[ \nabla^2 \phi - \frac{\partial^2 \phi}{\partial z^2} - \frac{\partial^2 \phi}{\partial r^2} \right] + \frac{\partial}{\partial r} \left( -\frac{1}{r} \frac{\partial \phi}{\partial r} \right) \right) = 0 \quad \text{Eq. 177}$$

$$\nabla^2 \left[ (1 - \nu) \nabla^2 \phi - \frac{\partial^2 \phi}{\partial z^2} \right] + \frac{\partial^2}{\partial z^2} \nabla^2 \phi \quad \text{Eq. 178}$$

And therefore:

$$\frac{\partial}{\partial z} \left( \frac{\partial}{\partial r} \left[ \nabla^2 \phi - \frac{\partial^2 \phi}{\partial z^2} - \frac{\partial^2 \phi}{\partial r^2} - \frac{1}{r} \frac{\partial \phi}{\partial r} \right] \right) = 0 \quad \text{Eq. 179}$$

$$(1 - \nu) \nabla^2 \nabla^2 \phi - \nabla^2 \left[ \frac{\partial^2 \phi}{\partial z^2} \right] + \frac{\partial^2}{\partial z^2} \nabla^2 \phi = 0 \quad \text{Eq. 180}$$

Which comports:

$$\frac{\partial}{\partial z} \left( \frac{\partial}{\partial r} [\nabla^2 \phi - \nabla^2 \phi] \right) = 0 \quad \text{Eq. 181}$$

$$(1 - \nu) \nabla^2 \nabla^2 \phi - \left( \frac{\partial^2 \phi}{\partial z^2} + \frac{\partial^2 \phi}{\partial r^2} + \frac{1}{r} \frac{\partial \phi}{\partial r} \right) \left[ \frac{\partial^2 \phi}{\partial z^2} \right] + \frac{\partial^2}{\partial z^2} \left( \frac{\partial^2 \phi}{\partial z^2} + \frac{\partial^2 \phi}{\partial r^2} + \frac{1}{r} \frac{\partial \phi}{\partial r} \right) = 0 \quad \text{Eq. 182}$$

i.e. the first equation is identically verified. Furthermore, since  $\partial^2/\partial z^2$  commutes with  $\nabla^2$ :

$$\nabla^2 \frac{\partial^2}{\partial z^2} = \frac{\partial^2}{\partial z^2} \nabla^2 \quad \text{Eq. 183}$$

the Eq. 182 can be simplified to:

$$(1 - \nu) \nabla^2 \nabla^2 \phi = 0 \quad \text{Eq. 184}$$

Therefore the equation system Eq. 161, Eq. 162 is satisfied if the function  $\phi(r,z)$  is chosen in a way such that:

$$\nabla^2 \nabla^2 \phi = 0 \quad \text{Eq. 185}$$

Or equivalently:

$$\left( \frac{\partial^2}{\partial r^2} + \frac{1}{r} \frac{\partial}{\partial r} + \frac{\partial^2}{\partial z^2} \right) \left( \frac{\partial^2}{\partial r^2} + \frac{1}{r} \frac{\partial}{\partial r} + \frac{\partial^2}{\partial z^2} \right) \phi = 0 \quad \text{Eq. 186}$$

### 3.5.1. FACTORIZATION OF THE STRESS FUNCTION

The Eq. 186 is a Biharmonic equation. We can search a solution in the form:

$$\phi = \sin(kz) F(r) \quad \text{Eq. 187}$$

By substituting the Eq. 187 in the Eq. 186 we have:

$$\left( \frac{\partial^2}{\partial r^2} + \frac{1}{r} \frac{\partial}{\partial r} + \frac{\partial^2}{\partial z^2} \right) \left( \frac{\partial^2}{\partial r^2} + \frac{1}{r} \frac{\partial}{\partial r} + \frac{\partial^2}{\partial z^2} \right) \sin(kz) F(r) = 0 \quad \text{Eq. 188}$$

$$\left[ \left( \frac{\partial^2}{\partial r^2} + \frac{1}{r} \frac{\partial}{\partial r} \right)^2 + 2 \left( \frac{\partial^2}{\partial r^2} + \frac{1}{r} \frac{\partial}{\partial r} \right) \frac{\partial^2}{\partial z^2} + \frac{\partial^4}{\partial z^4} \right] \sin(kz) F(r) = 0 \quad \text{Eq. 189}$$

By calculating the derivatives with respect to z we get:

$$\left[ \sin(kz) \left( \frac{d^2}{dr^2} + \frac{1}{r} \frac{d}{dr} \right)^2 F(r) - 2k^2 \sin(kz) \left( \frac{d^2}{dr^2} + \frac{1}{r} \frac{d}{dr} \right) F(r) + k^4 \sin(kz) F(r) \right] = 0 \quad \text{Eq. 190}$$

And by simplifying the  $\sin(kz)$  term:

$$\left[ \left( \frac{d^2}{dr^2} + \frac{1}{r} \frac{d}{dr} \right)^2 F(r) - 2k^2 \left( \frac{d^2}{dr^2} + \frac{1}{r} \frac{d}{dr} \right) F(r) + k^4 F(r) \right] = 0 \quad \text{Eq. 191}$$

$$\left( \frac{d^2}{dr^2} + \frac{1}{r} \frac{d}{dr} - k^2 \right) \left( \frac{d^2}{dr^2} + \frac{1}{r} \frac{d}{dr} - k^2 \right) F(r) = 0 \quad \text{Eq. 192}$$

### 3.5.2. RADIAL SOLUTION

Two particular solutions of the Eq. 192 can be found considering that it's satisfied if :

$$\left( \frac{d^2}{dr^2} + \frac{1}{r} \frac{d}{dr} - k^2 \right) F(r) = 0 \quad \text{Eq. 193}$$

Through the substitution:

$$x = ikr \quad \text{Eq. 194}$$

We get:

$$\frac{d}{dr} = \frac{d}{dx} \frac{dx}{dr} = ik \frac{d}{dx} \quad \frac{d^2}{dr^2} = -k^2 \frac{d^2}{dx^2} \quad F(r) = F\left(\frac{x}{ik}\right) = y(x) \quad \text{Eq. 195}$$

And therefore:

$$\left(-k^2 \frac{d^2}{dx^2} + \frac{ik}{x} ik \frac{d}{dx} - k^2\right)y = 0 \quad \text{Eq. 196}$$

$$\left(-k^2 \frac{d^2}{dx^2} - \frac{1}{x} k^2 \frac{d}{dx} - k^2\right)y = 0 \quad \text{Eq. 197}$$

$$x^2 \frac{d^2 y}{dx^2} + x \frac{dy}{dx} + x^2 y = 0 \quad \text{Eq. 198}$$

Here it's easy to recognize the Eq. 198 as a Bessel equation of zero order:

$$x^2 \frac{d^2 y}{dx^2} + x \frac{dy}{dx} + (x^2 - \nu^2)y = 0 \quad \nu = 0 \quad \text{Eq. 199}$$

which, as well known has the solutions:

$$y = AJ_\nu(x) + BY_\nu(x) \quad \nu = 0 \quad \text{Eq. 200}$$

Where A and B are arbitrary constants,  $J_\nu$  is the Bessel function of the first kind and order  $\nu$  while  $Y_\nu$  is the Bessel function of the second kind and order  $\nu$ . By substituting the expression of  $x(r)$  we have:

$$F(r) = AJ_0(ikr) + BY_0(ikr) \quad \text{Eq. 201}$$

Of course, since the Eq. 192 is of the fourth order, two further particular solutions must be found; it's possible to verify that they are:

$$F(r) = C(ikr)J_1(ikr) + D(ikr)Y_1(ikr) \quad \text{Eq. 202}$$

Where C and D are arbitrary constants and  $J_1, Y_1$  Bessel function of the first order. Indeed, indicating for compactness:

$$xJ_\nu = (ikr)J_\nu(ikr) \quad \text{Eq. 203}$$

For the following properties of the Bessel functions  $J_n$ :

$$\frac{d}{dx}(x^n J_n) = x^n J_{n-1} \quad \text{Eq. 204}$$

$$\frac{d}{dx}(x^n J_{-n}) = -x^n J_{-n+1} \quad \text{Eq. 205}$$

we have:

$$\frac{d}{dr}(x J_1) = \frac{d}{dx}(x J_1) \frac{dx}{dr} = ikx J_0 \quad \text{Eq. 206}$$

$$\frac{d}{dr}(x J_{-1}) = \frac{d}{dx}(x J_{-1}) \frac{dx}{dr} = -ikx J_0 \quad \text{Eq. 207}$$

And therefore:

$$\frac{1}{r} \frac{d}{dr}(x J_1) = -k^2 J_0 \quad \text{Eq. 208}$$

While

$$\frac{d^2}{dr^2}(x J_1) = \frac{d}{dr}(ikx J_0) = \frac{d}{dx}(ikx J_0) \frac{dx}{dr} = -k^2 \left[ J_0 + \frac{x}{2}(J_{-1} - J_1) \right] \quad \text{Eq. 209}$$

So we can verify that  $x J_1$  is a particular solution of the Eq. 192 starting to calculate the term:

---

$$\left(\frac{d^2}{dr^2} + \frac{1}{r} \frac{d}{dr} - k^2\right) xJ_1 \quad \text{Eq. 210}$$

Employing the Eq. 208 and the Eq. 209 we have:

$$\left(\frac{d^2}{dr^2} + \frac{1}{r} \frac{d}{dr} - k^2\right) xJ_1 = -k^2 \left[J_0 + \frac{x}{2}(J_{-1} - J_1)\right] - k^2 J_0 - k^2 xJ_1 \quad \text{Eq. 211}$$

$$\left(\frac{d^2}{dr^2} + \frac{1}{r} \frac{d}{dr} - k^2\right) xJ_1 = -k^2 \left[2J_0 + \frac{x}{2}(J_{-1} + J_1)\right] \quad \text{Eq. 212}$$

Furthermore, for another well known property of the Bessel function:

$$J_{n+1}(x) = \frac{2n}{x} J_n(x) - J_{n-1}(x) \quad \text{Eq. 213}$$

Which comports for n=0:

$$J_1(x) + J_{-1}(x) = 0 \quad \text{Eq. 214}$$

The Eq. 212 becomes:

$$\left(\frac{d^2}{dr^2} + \frac{1}{r} \frac{d}{dr} - k^2\right) xJ_1 = -2k^2 J_0 \quad \text{Eq. 215}$$

Introducing the L operator:

$$L = \left(\frac{d^2}{dr^2} + \frac{1}{r} \frac{d}{dr} - k^2\right) \quad \text{Eq. 216}$$

We have:

$$L^2(xJ_1) = -2k^2 \left(\frac{d^2}{dr^2} + \frac{1}{r} \frac{d}{dr} - k^2\right) J_0 \quad \text{Eq. 217}$$

So we must now simply verify that (Eq. 192) :

$$L^2(xJ_1) = 0 \quad \text{Eq. 218}$$

Therefore, since:

$$\frac{d}{dx}J_\nu = \frac{1}{2}(J_{\nu-1} - J_{\nu+1}) \quad \text{Eq. 219}$$

$$\frac{d^2}{dx^2}J_\nu = \frac{1}{4}(J_{\nu-2} - 2J_{\nu-2} + J_{\nu+2}) \quad \text{Eq. 220}$$

It results:

$$\frac{d^2}{dr^2}J_0 = \frac{d}{dr} \frac{d}{dr}J_0 = \frac{d}{dx} \left( \frac{d}{dx}J_0 \right) \left( \frac{dx}{dr} \right)^2 = \frac{d}{dx} \left( \frac{J_{-1} - J_1}{2} \right) (-k^2) = -k^2 \left( \frac{J_{-2} - 2J_0 + J_2}{4} \right) \quad \text{Eq. 221}$$

And:

$$\frac{1}{r} \frac{d}{dr}J_0 = \frac{1}{r} \left( \frac{d}{dx}J_0 \right) \frac{dx}{dr} = \frac{ik}{r} \left( \frac{J_{-1} - J_1}{2} \right) \quad \text{Eq. 222}$$

Substituting in the Eq. 218, we have:

$$L^2(xJ_1) = -2k^2 \left[ -k^2 \left( \frac{J_{-2} - 2J_0 + J_2}{4} \right) + \frac{ik}{r} \left( \frac{J_{-1} - J_1}{2} \right) - k^2J_0 \right] \quad \text{Eq. 223}$$

$$L^2(xJ_1) = k^4 \left[ \left( \frac{J_{-2} + 2J_0 + J_2}{2} \right) + \frac{J_{-1} - J_1}{ikr} \right] \quad \text{Eq. 224}$$

$$L^2(xJ_1) = k^4 \left[ \left( \frac{J_{-2} + 2J_0 + J_2}{2} \right) + \frac{J_{-1} - J_1}{x} \right] \quad \text{Eq. 225}$$

But, for the property of the Bessel functions, Eq. 213:

$$J_{n+1}(x) = \frac{2n}{x}J_n(x) - J_{n-1}(x) \quad \text{Eq. 226}$$

Which for  $n=1$  and  $n=-1$  comports:

---

$$J_2(x) = \frac{2}{x}J_1(x) - J_0(x) \Rightarrow \frac{J_1(x)}{x} = \frac{J_2(x) + J_0(x)}{2} \quad \text{Eq. 227}$$

$$J_0(x) = -\frac{2}{x}J_{-1}(x) - J_{-2}(x) \Rightarrow \frac{J_{-1}(x)}{x} = -\frac{J_{-2}(x) + J_0(x)}{2} \quad \text{Eq. 228}$$

We get:

$$\frac{J_{-1} - J_1}{x} = \frac{-J_{-2} - J_0 - J_2 - J_0}{2} = -\frac{J_{-2} + 2J_0 + J_2}{2} \quad \text{Eq. 229}$$

By substituting in the Eq. 225 we have:

$$L^2(xJ_1) = k^4 \left[ \left( \frac{J_{-2} + 2J_0 + J_2}{2} \right) - \frac{J_{-2} + 2J_0 + J_2}{2} \right] = 0 \quad \text{Eq. 230}$$

Which proves that the function  $C(ikr)J_1(ikr)$  is a particular solution of the Eq. 192. Since the properties of the Bessel functions of the first kind  $J_\nu(x)$ , Eq. 204, Eq. 205, Eq. 219, Eq. 220 and Eq. 213 are also valid for the second kind Bessel functions  $Y_\nu(x)$ , it's also proved that  $D(ikr)Y_1(ikr)$  is a particular solution of the Eq. 192. Finally we can write:

$$F(r) = AJ_0(ikr) + BY_0(ikr) + C(ikr)J_1(ikr) + D(ikr)Y_1(ikr) \quad \text{Eq. 231}$$

And:

$$\phi(r, z) = \sin(kz) [AJ_0(ikr) + BY_0(ikr) + C(ikr)J_1(ikr) + D(ikr)Y_1(ikr)] \quad \text{Eq. 232}$$

Or, for compactness:

$$\phi(r, z) = \sin(kz) F(r) = \sin(kz) (AJ_0 + BY_0 + CxJ_1 + DxY_1) \quad \text{Eq. 233}$$

### 3.5.3. STRESS COMPONENTS

Substituting the Eq. 232 in the Eq. 163 - Eq. 166, it results:

$$\sigma_r = \frac{\partial}{\partial z} \left( \nu \nabla^2 - \frac{\partial^2}{\partial r^2} \right) [\sin(kz) (AJ_0 + BY_0 + CxJ_1 + DxY_1)] \quad \text{Eq. 234}$$

$$\sigma_\theta = \frac{\partial}{\partial z} \left( \nu \nabla^2 - \frac{1}{r} \frac{\partial}{\partial r} \right) [\sin(kz) (AJ_0 + BY_0 + CxJ_1 + DxY_1)] \quad \text{Eq. 235}$$

$$\sigma_z = \frac{\partial}{\partial z} \left[ (2 - \nu) \nabla^2 - \frac{\partial^2}{\partial z^2} \right] [\sin(kz) (AJ_0 + BY_0 + CxJ_1 + DxY_1)] \quad \text{Eq. 236}$$

$$\tau_{rz} = \frac{\partial}{\partial r} \left[ (1 - \nu) \nabla^2 - \frac{\partial^2}{\partial z^2} \right] [\sin(kz) (AJ_0 + BY_0 + CxJ_1 + DxY_1)] \quad \text{Eq. 237}$$

All the terms from the Eq. 234 to the Eq. 237 must be calculated; in the Eq. 234 we have:

$$\frac{\partial^2}{\partial r^2} [\sin(kz) F(r)] = \sin(kz) \frac{d^2}{dr^2} F(r) = -k^2 \sin(kz) \frac{d^2}{dx^2} (AJ_0 + BY_0 + CxJ_1 + DxY_1) \quad \text{Eq. 238}$$

The last term in the Eq. 238 can be evaluated considering the Eq. 219, Eq. 220 in combination with the following relations for the Bessel functions:

$$J_{-n} = (-1)^n J_n \quad \text{Eq. 239}$$

$$Y_{-n} = (-1)^n Y_n \quad \text{Eq. 240}$$

It results:

$$\frac{d^2}{dx^2} (AJ_0 + BY_0) = A \frac{1}{4} (J_{-2} - 2J_0 + J_2) + B \frac{1}{4} (Y_{-2} - 2Y_0 + Y_2) = A \frac{J_2 - J_0}{2} + B \frac{Y_2 - J_0}{2} \quad \text{Eq. 241}$$

$$\frac{d^2}{dx^2} (CxJ_1 + DxY_1) = C(J_0 - xJ_1) + D(Y_0 - xY_1) \quad \text{Eq. 242}$$

And for the Eq. 226:

$$\frac{d^2}{dx^2}(AJ_0 + BY_0) = A \frac{J_2 - J_0}{2} + B \frac{Y_2 - Y_0}{2} = A \left( \frac{J_1}{x} - J_0 \right) + B \left( \frac{Y_1}{x} - Y_0 \right) \quad \text{Eq. 243}$$

Then, in the Eq. 235 we have:

$$\frac{1}{r} \frac{\partial}{\partial r} [\sin(kz) F(r)] = \sin(kz) \frac{1}{r} \frac{d}{dr} F(r) = -k^2 \sin(kz) \frac{1}{x} \frac{d}{dx} (AJ_0 + BY_0 + CxJ_1 + DxY_1) \quad \text{Eq. 244}$$

$$\frac{1}{r} \frac{\partial}{\partial r} [\sin(kz) F(r)] = k^2 \sin(kz) \left( \frac{AJ_1 + BY_1}{x} - CJ_0 - DY_0 \right) \quad \text{Eq. 245}$$

Finally:

$$\frac{\partial^2}{\partial z^2} [\sin(kz) F(r)] = -k^2 \sin(kz) F(r) \quad \text{Eq. 246}$$

$$\nabla^2 [\sin(kz) F(r)] = \sin(kz) \left( \frac{d^2}{dr^2} + \frac{1}{r} \frac{d}{dr} - k^2 \right) F(r) = \sin(kz) L(F(r)) \quad \text{Eq. 247}$$

With:

$$L = \left( \frac{d^2}{dr^2} + \frac{1}{r} \frac{d}{dr} - k^2 \right) \quad \text{Eq. 248}$$

Considering also that  $AJ_0 + BY_0$  is a solution of the Eq. 193:

$$L(AJ_0 + BY_0) = \left( \frac{d^2}{dr^2} + \frac{1}{r} \frac{d}{dr} - k^2 \right) (AJ_0 + BY_0) = 0 \quad \text{Eq. 249}$$

We have:

$$L(F(r)) = L(CxJ_1 + DxY_1) = -k^2 \left( \frac{d^2}{dx^2} + \frac{1}{x} \frac{d}{dx} + 1 \right) (CxJ_1 + DxY_1) = -k^2 L_x(CxJ_1 + DxY_1) \quad \text{Eq. 250}$$

Having defined the  $L_x$  operator as:

$$L_x = \left( \frac{d^2}{dx^2} + \frac{1}{x} \frac{d}{dx} + 1 \right) \quad \text{Eq. 251}$$

Calculating  $L_x(CxJ_1 + DxY_1)$  by employing the Eq. 204 and the Eq. 242 we obtain:

$$L_x(CxJ_1 + DxY_1) = \frac{d^2}{dx^2} (CxJ_1 + DxY_1) + \frac{1}{x} \frac{d}{dx} (CxJ_1 + DxY_1) + (CxJ_1 + DxY_1) \quad \text{Eq. 252}$$

$$L_x(CxJ_1 + DxY_1) = C(J_0 - xJ_1) + D(Y_0 - xY_1) + \frac{CxJ_0 + DxY_0}{x} + (CxJ_1 + DxY_1) \quad \text{Eq. 253}$$

$$L_x(CxJ_1 + DxY_1) = 2CJ_0 + 2DY_0 \quad \text{Eq. 254}$$

By substituting the Eq. 242, Eq. 243, Eq. 245, Eq. 247, Eq. 250 and Eq. 254 in the stress components, from Eq. 234 to the Eq. 237, we get:

$$\sigma_r = \frac{\partial}{\partial z} \left[ k^2 \sin(kz) \left( -2\nu(CJ_0 + DY_0) + \frac{d^2}{dx^2} (AJ_0 + BY_0 + CxJ_1 + DxY_1) \right) \right] \quad \text{Eq. 255}$$

$$\sigma_\theta = \frac{\partial}{\partial z} \left[ -k^2 \sin(kz) \left( 2\nu(CJ_0 + DY_0) + \frac{AJ_1 + BY_1}{x} - CJ_0 - DY_0 \right) \right] \quad \text{Eq. 256}$$

$$\sigma_z = \frac{\partial}{\partial z} \left[ -k^2 \sin(kz) (2(2 - \nu)(CJ_0 + DY_0) - (AJ_0 + BY_0 + CxJ_1 + DxY_1)) \right] \quad \text{Eq. 257}$$

$$\tau_{rz} = \frac{\partial}{\partial r} \left[ -k^2 \sin(kz) ((1 - \nu)(CJ_0 + DY_0) - (AJ_0 + BY_0 + CxJ_1 + DxY_1)) \right] \quad \text{Eq. 258}$$

Which can be simplified as:

$$\sigma_r = k^3 \cos(kz) \left( -2\nu(CJ_0 + DY_0) + A \left( \frac{J_1}{x} - J_0 \right) + B \left( \frac{Y_1}{x} - Y_0 \right) + C(J_0 - xJ_1) + D(Y_0 - xY_1) \right) \quad \text{Eq. 259}$$

$$\sigma_\theta = -k^3 \cos(kz) \left( 2\nu(CJ_0 + DY_0) + \frac{AJ_1 + BY_1}{x} - CJ_0 - DY_0 \right) \quad \text{Eq. 260}$$

$$\sigma_z = -k^3 \cos(kz) [2(2 - \nu)(CJ_0 + DY_0) - (AJ_0 + BY_0 + CxJ_1 + DxY_1)] \quad \text{Eq. 261}$$

$$\tau_{rz} = -ik^3 \sin(kz) \frac{d}{dx} [2(1 - \nu)(CJ_0 + DY_0) - (AJ_0 + BY_0 + CxJ_1 + DxY_1)] \quad \text{Eq. 262}$$

And then rearranged in:

$$\sigma_r = k^3 \cos(kz) \left( A \left( \frac{J_1}{x} - J_0 \right) + B \left( \frac{Y_1}{x} - Y_0 \right) + C[J_0(1 - 2\nu) - xJ_1] + D[Y_0(1 - 2\nu) - xY_1] \right) \quad \text{Eq. 263}$$

$$\sigma_\theta = k^3 \cos(kz) \left( -\frac{AJ_1 + BY_1}{x} + CJ_0(1 - 2\nu) + DY_0(1 - 2\nu) \right) \quad \text{Eq. 264}$$

$$\sigma_z = k^3 \cos(kz) [AJ_0 + BY_0 + C[xJ_1 - 2(2 - \nu)J_0] + D[xY_1 - 2(2 - \nu)Y_0]] \quad \text{Eq. 265}$$

$$\tau_{rz} = -ik^3 \sin(kz) [-2(1 - \nu)(CJ_1 + DY_1) + (AJ_1 + BY_1 - CxJ_0 - DxY_0)] \quad \text{Eq. 266}$$

To get the final expression of the stress:

$$\sigma_r = k^3 \cos(kz) \left( A \left( \frac{J_1}{x} - J_0 \right) + B \left( \frac{Y_1}{x} - Y_0 \right) + C[J_0(1 - 2\nu) - xJ_1] + D[Y_0(1 - 2\nu) - xY_1] \right) \quad \text{Eq. 267}$$

$$\sigma_\theta = k^3 \cos(kz) \left( -\frac{AJ_1 + BY_1}{x} + CJ_0(1 - 2\nu) + DY_0(1 - 2\nu) \right) \quad \text{Eq. 268}$$

$$\sigma_z = k^3 \cos(kz) [AJ_0 + BY_0 + C[xJ_1 - 2(2 - \nu)J_0] + D[xY_1 - 2(2 - \nu)Y_0]] \quad \text{Eq. 269}$$

$$\tau_{rz} = ik^3 \sin(kz) [-AJ_1 - BY_1 + C[2(1 - \nu)J_1 + xJ_0] + D[2(1 - \nu)Y_1 + xY_0]] \quad \text{Eq. 270}$$

### 3.6. DETERMINATION OF THE CONSTANTS IN THE STRESS COMPONENTS

Now we must consider that the sensor is divided into two different zones: the glass fiber zone and the coating zone and for each zone for an assigned value of  $k$ , 4 constant, A,B,C and D must be found. In order to determine these constant, the appropriate boundary conditions on this two zone must be imposed; furthermore it must be considered that Bessel functions of the second kind  $Y_0$  and  $Y_1$  are not defined in  $r=0$ , for which  $x=ikr=0$ , i.e. at the center of the glass fiber zone; therefore it must be:

$$B_f = 0, \quad D_f = 0 \quad \text{Eq. 271}$$

Where the subscript f indicates the glass fiber. Conversely for the Eq. 159 we have to impose:

$$\sigma_{rf}(r_{ci}, z) = \sigma_{rc}(r_{ci}, z) \quad \text{Eq. 272}$$

$$\begin{aligned} k^3 \cos(kz) \left( A_c \left( \frac{J_1}{x_{ci}} - J_0 \right) + B_c \left( \frac{Y_1}{x_{ci}} - Y_0 \right) + C_c [J_0(1 - 2\nu) - x_{ci}J_1] + D_c [Y_0(1 - 2\nu) - x_{ci}Y_1] \right) = \\ = k^3 \cos(kz) \left( A_f \left( \frac{J_1}{x_{ci}} - J_0 \right) + C_f [J_0(1 - 2\nu) - x_{ci}J_1] \right) \end{aligned} \quad \text{Eq. 273}$$

And for the Eq. 160

$$\tau_{rzf}(r_{ci}, z) = \tau_{rzc}(r_{ci}, z) \quad \text{Eq. 274}$$

$$\begin{aligned} ik^3 \sin(kz) [-A_c J_1 - B_c Y_1 + C_c [2(1 - \nu)J_1 + x_{ci}J_0] + D_c [2(1 - \nu)Y_1 + x_{ci}Y_0]] = \\ = ik^3 \sin(kz) [-A_f J_1 + C_f [2(1 - \nu)J_1 + x_{ci}J_0]] \end{aligned} \quad \text{Eq. 275}$$

Where the subscript c indicates the coating zone and  $x_{ci}$  the x value for  $r = r_{ci}$  i.e. the internal radius of the coating:

$$x_{ci} = ikr_{ci} \quad \text{Eq. 276}$$

Of the course all the Bessel function in the Eq. 273 Eq. 275 are intended evaluated in  $x = x_{ci}$

Further two relations can be obtained imposing that, on the external coating surface the radial and the tangential stress must be zero, according to the Eq. 153 and Eq. 154; thus it must be:

$$\sigma_r(r_{ce}, z) = 0 \Rightarrow \quad \text{Eq. 277}$$

$$\left( A_c \left( \frac{J_1}{x} - J_0 \right) + B_c \left( \frac{Y_1}{x} - Y_0 \right) + C_c [J_0(1 - 2\nu) - xJ_1] + D_c [Y_0(1 - 2\nu) - xY_1] \right)_{x=x_{ce}} = 0 \quad \text{Eq. 278}$$

And

$$\tau_{rz}(r_{ce}, z) = 0 \Rightarrow \quad \text{Eq. 279}$$

$$(-A_c J_1 - B_c Y_1 + C_c [2(1 - \nu)J_1 + xJ_0] + D_c [2(1 - \nu)Y_1 + xY_0])_{x=x_{ce}} = 0 \quad \text{Eq. 280}$$

The last two condition must be imposed to guarantee the continuity of the circumferential and axial strain at the interface between fiber and coating, according to the Eq. 157, Eq. 158; the total circumferential strains at the interface, for the Eq. 150 and the constitutive materials relations, Eq. 147, Eq. 148 are respectively given by:

$$\begin{aligned} \varepsilon_{\theta f}(r_{ci}, z) &= (\varepsilon_{\theta f}^{el} + \varepsilon_{\theta f}^{th} + \varepsilon_{\theta f}^{sw})_{r=r_{ci}} = \\ &= \frac{\sigma_{\theta f}(r_{ci}, z) - \nu_f [\sigma_{rf}(r_{ci}, z) + \sigma_{zf}(r_{ci}, z)]}{E_f} + \alpha_f (T - T_{ref}) + \beta_f (RH - RH_{ref}) \end{aligned} \quad \text{Eq. 281}$$

$$\begin{aligned} \varepsilon_{\theta c}(r_{ci}, z) &= (\varepsilon_{\theta c}^{el} + \varepsilon_{\theta c}^{th} + \varepsilon_{\theta c}^{sw})_{r=r_{ci}} = \\ &= \frac{\sigma_{\theta c}(r_{ci}, z) - \nu_c [\sigma_{rc}(r_{ci}, z) + \sigma_{zc}(r_{ci}, z)]}{E_c} + \alpha_c (T - T_{ref}) + \beta_c (RH - RH_{ref}) \end{aligned} \quad \text{Eq. 282}$$

While the axial strains are given by:

$$\begin{aligned} \varepsilon_{zf}(r_{ci}, z) &= (\varepsilon_{zf}^{el} + \varepsilon_{zf}^{th} + \varepsilon_{zf}^{sw})_{r=r_{ci}} = \\ &= \frac{\sigma_{zf}(r_{ci}, z) - \nu_f [\sigma_{rf}(r_{ci}, z) + \sigma_{\theta f}(r_{ci}, z)]}{E_f} + \alpha_f(T - T_{ref}) + \beta_f(RH - RH_{ref}) \end{aligned} \quad \text{Eq. 283}$$

$$\begin{aligned} \varepsilon_{zc}(r_{ci}, z) &= (\varepsilon_{zc}^{el} + \varepsilon_{zc}^{th} + \varepsilon_{zc}^{sw})_{r=r_{ci}} = \\ &= \frac{\sigma_{zc}(r_{ci}, z) - \nu_c [\sigma_{rc}(r_{ci}, z) + \sigma_{\theta c}(r_{ci}, z)]}{E_c} + \alpha_c(T - T_{ref}) + \beta_c(RH - RH_{ref}) \end{aligned} \quad \text{Eq. 284}$$

Of course the glass fiber doesn't absorb humidity, and then we can write:

$$\beta_f = 0 \quad \text{Eq. 285}$$

Therefore the continuity condition  $\varepsilon_{\theta f}(r_{ci}, z) = \varepsilon_{\theta c}(r_{ci}, z)$  becomes:

$$\begin{aligned} &\frac{\sigma_{\theta f}(r_{ci}, z) - \nu_f [\sigma_{rf}(r_{ci}, z) + \sigma_{zf}(r_{ci}, z)]}{E_f} + \alpha_f(T - T_{ref}) = \\ &= \frac{\sigma_{\theta c}(r_{ci}, z) - \nu_c [\sigma_{rc}(r_{ci}, z) + \sigma_{zc}(r_{ci}, z)]}{E_c} + \alpha_c(T - T_{ref}) + \beta_c(RH - RH_{ref}) \end{aligned} \quad \text{Eq. 286}$$

While the continuity condition  $\varepsilon_{zf}(r_{ci}, z) = \varepsilon_{zc}(r_{ci}, z)$  can be expressed as:

$$\begin{aligned} &\frac{\sigma_{zf}(r_{ci}, z) - \nu_f [\sigma_{rf}(r_{ci}, z) + \sigma_{\theta f}(r_{ci}, z)]}{E_f} + \alpha_f(T - T_{ref}) = \\ &= \frac{\sigma_{zc}(r_{ci}, z) - \nu_c [\sigma_{rc}(r_{ci}, z) + \sigma_{\theta c}(r_{ci}, z)]}{E_c} + \alpha_c(T - T_{ref}) + \beta_c(RH - RH_{ref}) \end{aligned} \quad \text{Eq. 287}$$

The Eq. 286 and Eq. 287 are the last two equations to impose. Together with the Eq. 273, Eq. 275, Eq. 278 and Eq. 280 they form an equation system that allows to determine the 6 unknowns  $A_f, C_f, A_c, B_c, C_c, D_c$  given that  $B_f = 0, D_f = 0$  for the Eq. 271. The equation system can be written compactly in the form:

$$\begin{bmatrix} \sigma_r(r_{ce}, z) \\ \tau_{rz}(r_{ce}, z) \\ \sigma_{rf}(r_{ci}, z) - \sigma_{rc}(r_{ci}, z) \\ \tau_{rzf}(r_{ci}, z) - \tau_{rzc}(r_{ci}, z) \\ \varepsilon_{\theta f}^{el}(r_{ci}, z) - \varepsilon_{\theta c}^{el}(r_{ci}, z) \\ \varepsilon_{zf}^{el}(r_{ci}, z) - \varepsilon_{zc}^{el}(r_{ci}, z) \end{bmatrix} = \begin{bmatrix} 0 \\ 0 \\ 0 \\ 0 \\ (\alpha_c - \alpha_f)(T - T_{ref}) + \beta_c(RH - RH_{ref}) \\ (\alpha_c - \alpha_f)(T - T_{ref}) + \beta_c(RH - RH_{ref}) \end{bmatrix} \quad \text{Eq. 288}$$

### 3.6.1. FOURIER SERIES EXPANSION

Here it's worth to evidence that the strain continuity equations, corresponding to the last two rows in the Eq. 288, cannot be solved substituting directly the expression of stress relations, from Eq. 267 to the Eq. 270 since their dependence by the z coordinate is sinusoidal, while the right member Eq. 288 is a constant in z. Therefore a decomposition in a sinusoidal series of the term  $(\alpha_c - \alpha_f)(T - T_{ref}) + \beta_c(RH - RH_{ref})$  is needed. This is possible since a combination of the stress relations, from Eq. 267 to the Eq. 270, with different values of k (wave number) is still a solution of the equilibrium equation system, Eq. 163 - Eq. 166, being it linear. Anyway the choice of the wave number cannot be arbitrary; conversely it must assure the on both the bottom and the top surface of the coating and the fiber the axial stress is zero. Therefore it must be:

$$\sigma_z \left( r, \pm \frac{L}{2} \right) = k^3 \cos \left( \frac{kL}{2} \right) R(r) = 0 \quad \text{Eq. 289}$$

And then the acceptable values of k are:

$$\cos \left( \pm \frac{kL}{2} \right) = 0 \Rightarrow \frac{kL}{2} = \pi \left( \frac{1}{2} + m \right) \Rightarrow k_m = \frac{\pi}{L} (1 + 2m) \quad m = 0, 1, 2, \dots \quad \text{Eq. 290}$$

Since all normal stress components,  $\sigma_r, \sigma_\theta, \sigma_z$  depend by z through  $\cos(kz)$  the Eq. 286 can be written as:

$$\begin{aligned} & \sum_k k^3 \cos(kz) \frac{F_{\theta f}(r_{ci}) - \nu_f [F_{rf}(r_{ci}) + F_{zf}(r_{ci})]}{E_f} + \alpha_f (T - T_{ref}) = \\ & = \sum_k k^3 \cos(kz) \frac{F_{\theta c}(r_{ci}) - \nu_c [F_{rc}(r_{ci}) + F_{zc}(r_{ci})]}{E_c} + \alpha_c (T - T_{ref}) + \beta_c (RH - RH_{ref}) \end{aligned} \quad \text{Eq. 291}$$

While the continuity condition Eq. 287 can be expressed as:

$$\begin{aligned} & \sum_k k^3 \cos(kz) \frac{F_{zf}(r_{ci}) - \nu_f [F_{rf}(r_{ci}) + F_{\theta f}(r_{ci})]}{E_f} + \alpha_f (T - T_{ref}) = \\ & = \sum_k k^3 \cos(kz) \frac{F_{zc}(r_{ci}) - \nu_c [F_{rc}(r_{ci}) + F_{\theta c}(r_{ci})]}{E_c} + \alpha_c (T - T_{ref}) + \beta_c (RH - RH_{ref}) \end{aligned} \quad \text{Eq. 292}$$

Where all the functions  $F_{ij}$  are dependent by  $r_{ci}$  and k only. Defining therefore :

$$H_{\theta_f}(r_{ci}, k) = \frac{F_{\theta_f}(r_{ci}) - \nu_f [F_{r_f}(r_{ci}) + F_{z_f}(r_{ci})]}{E_f} \quad \text{Eq. 293}$$

$$H_{\theta_c}(r_{ci}, k) = \frac{F_{\theta_c}(r_{ci}) - \nu_c [F_{r_c}(r_{ci}) + F_{z_c}(r_{ci})]}{E_c} \quad \text{Eq. 294}$$

$$H_{z_f}(r_{ci}, k) = \frac{F_{z_f}(r_{ci}) - \nu_f [F_{r_f}(r_{ci}) + F_{\theta_f}(r_{ci})]}{E_f} \quad \text{Eq. 295}$$

$$H_{z_c}(r_{ci}, k) = \frac{F_{z_c}(r_{ci}) - \nu_c [F_{r_c}(r_{ci}) + F_{\theta_c}(r_{ci})]}{E_c} \quad \text{Eq. 296}$$

The Eq. 286 and Eq. 287 become:

$$\sum_k k^3 \cos(kz) H_{\theta_f}(r_{ci}, k) + \alpha_f (T - T_{ref}) = \sum_k k^3 \cos(kz) H_{\theta_c}(r_{ci}, k) + \alpha_c (T - T_{ref}) + \beta_c (RH - RH_{ref}) \quad \text{Eq. 297}$$

$$\sum_k k^3 \cos(kz) H_{z_f}(r_{ci}, k) + \alpha_f (T - T_{ref}) = \sum_k k^3 \cos(kz) H_{z_c}(r_{ci}, k) + \alpha_c (T - T_{ref}) + \beta_c (RH - RH_{ref}) \quad \text{Eq. 298}$$

Or equivalently:

$$\sum_k k^3 \cos(kz) [H_{\theta_f}(r_{ci}, k) - H_{\theta_c}(r_{ci}, k)] = (\alpha_c - \alpha_f)(T - T_{ref}) + \beta_c (RH - RH_{ref}) \quad \text{Eq. 299}$$

$$\sum_k k^3 \cos(kz) [H_{z_f}(r_{ci}, k) - H_{z_c}(r_{ci}, k)] = (\alpha_c - \alpha_f)(T - T_{ref}) + \beta_c (RH - RH_{ref}) \quad \text{Eq. 300}$$

If we define the difference between the un-elastic strain as:

$$\Delta \varepsilon^{ue} = (\alpha_c - \alpha_f)(T - T_{ref}) + \beta_c (RH - RH_{ref}) \quad \text{Eq. 301}$$

$\Delta \varepsilon^{ue}$  can be expressed as function of the z coordinate with a cosine series in the interval  $[-L/2, L/2]$ :

$$\Delta \varepsilon^{ue} = \sum_{m=0}^{+\infty} c_m \cos(k_m z) \quad \text{Eq. 302}$$

Where the coefficients are given by:

---

$$c_m = \frac{1}{N} \int_{-\frac{L}{2}}^{+\frac{L}{2}} \Delta \varepsilon^{ue} \cos(k_m z) dz \quad \text{Eq. 303}$$

And N is given by:

$$N = \int_{-\frac{L}{2}}^{+\frac{L}{2}} \cos^2(kz) dz = \left[ \frac{z}{2} + \frac{\sin(2kz)}{4k} \right]_{-\frac{L}{2}}^{+\frac{L}{2}} = \frac{L}{2} \quad \text{Eq. 304}$$

Therefore we have:

$$c_m = \frac{2}{L} \Delta \varepsilon^{ue} \int_{-\frac{L}{2}}^{+\frac{L}{2}} \cos(k_m z) dz \quad \text{Eq. 305}$$

$$c_m = \frac{2}{Lk_m} \Delta \varepsilon^{ue} [\sin(k_m z)]_{-\frac{L}{2}}^{+\frac{L}{2}} = \frac{2}{Lk_m} \Delta \varepsilon^{ue} [\sin(1 + 2m)z]_{-\frac{L}{2}}^{+\frac{L}{2}} \quad \text{Eq. 306}$$

$$c_m = \frac{4}{Lk_m} \Delta \varepsilon^{ue} \sin \frac{(1 + 2m)L}{2} = \frac{4\Delta \varepsilon^{ue} (-1)^m}{Lk_m} \quad \text{Eq. 307}$$

The Eq. 301 becomes:

$$\Delta \varepsilon^{ue} = \sum_{m=0}^{+\infty} \frac{4\Delta \varepsilon^{ue} (-1)^m}{Lk_m} \cos(k_m z) \quad \text{Eq. 308}$$

Which, substituted in the Eq. 299 Eq. 300 and gives:

$$\sum_{m=0}^{+\infty} k_m^3 \cos(k_m z) [H_{\theta f}(r_{ci}, k_m) - H_{\theta c}(r_{ci}, k_m)] = \sum_{m=0}^{+\infty} \frac{4\Delta \varepsilon^{ue} (-1)^m}{Lk_m} \cos(k_m z) \quad \text{Eq. 309}$$

$$\sum_{m=0}^{+\infty} k_m^3 \cos(k_m z) [H_{z f}(r_{ci}, k_m) - H_{z c}(r_{ci}, k_m)] = \sum_{m=0}^{+\infty} \frac{4\Delta \varepsilon^{ue} (-1)^m}{Lk_m} \cos(k_m z) \quad \text{Eq. 310}$$

Since the terms  $[H_{\theta f}(r_{ci}, k_m) - H_{\theta c}(r_{ci}, k_m)]$  and  $[H_{z f}(r_{ci}, k_m) - H_{z c}(r_{ci}, k_m)]$  depend linearly by the coefficients  $A_f, C_f, A_c, B_c, C_c, D_c$ , which now must be determined for each value of  $k_m$ , we have:

$$\sum_{m=0}^{+\infty} k_m^3 \cos(k_m z) [\Delta H_{\varepsilon \theta}(r_{ci}, k_m)]_{1 \times 6} [A_f, C_f, A_c, B_c, C_c, D_c]_{k_m}^T = \sum_{m=0}^{+\infty} \frac{4\Delta\varepsilon^{ue}(-1)^m}{Lk_m} \cos(k_m z) \quad \text{Eq. 311}$$

$$\sum_{m=0}^{+\infty} k_m^3 \cos(k_m z) [\Delta H_{\varepsilon z}(r_{ci}, k_m)]_{1 \times 6} [A_f, C_f, A_c, B_c, C_c, D_c]_{k_m}^T = \sum_{m=0}^{+\infty} \frac{4\Delta\varepsilon^{ue}(-1)^m}{Lk_m} \cos(k_m z) \quad \text{Eq. 312}$$

And therefore for each coefficient relative to the term  $\cos(k_m z)$  it must be:

$$[\Delta H_{\varepsilon \theta}(r_{ci}, k_m)]_{1 \times 6} [A_f, C_f, A_c, B_c, C_c, D_c]_{k_m}^T = \frac{4\Delta\varepsilon^{ue}(-1)^m}{Lk_m^4} \quad \text{Eq. 313}$$

$$[\Delta H_{\varepsilon z}(r_{ci}, k_m)]_{1 \times 6} [A_f, C_f, A_c, B_c, C_c, D_c]_{k_m}^T = \frac{4\Delta\varepsilon^{ue}(-1)^m}{Lk_m^4} \quad \text{Eq. 314}$$

Where  $[\Delta H_{\theta}(r_{ci}, k_m)]_{1 \times 6}$  and  $[\Delta H_z(r_{ci}, k_m)]_{1 \times 6}$  are two row vectors depending by  $r_{ci}$  and  $k_m$  only, while the superscript T represent the Transposition operation.

### 3.6.2. ALGEBRAIC SOLVING SYSTEM

The Eq. 313, Eq. 314 represent the continuity strain relation at the interface fiber coating for every assigned value of the wave number  $k_m$ . Similarly we can decompose in series the first 4 relations in the solving system, Eq. 288, obtaining:

$$\sum_{m=0}^{+\infty} \begin{bmatrix} k_m^3 \cos(k_m z) H_{\sigma r}(r_{ce}, k_m) \\ ik_m^3 \sin(k_m z) H_{\tau rz}(r_{ce}, k_m) \\ k_m^3 \cos(k_m z) \Delta H_{\sigma r}(r_{ci}, k_m) \\ ik_m^3 \cos(k_m z) \Delta H_{\tau rz}(r_{ci}, k_m) \\ k_m^3 \cos(k_m z) \Delta H_{\varepsilon z}(r_{ci}, k_m) \\ k_m^3 \cos(k_m z) \Delta H_{\varepsilon z}(r_{ci}, k_m) \end{bmatrix}_{6 \times 6} \begin{bmatrix} A_f \\ C_f \\ A_c \\ B_c \\ C_c \\ D_c \end{bmatrix}_m = \sum_{m=0}^{+\infty} \frac{4(\Delta\varepsilon^{ue})(-1)^m}{Lk_m} \begin{bmatrix} 0 \\ 0 \\ 0 \\ 0 \\ \cos(k_m z) \\ \cos(k_m z) \end{bmatrix} \quad \text{Eq. 315}$$

And finally for each single acceptable value  $k_m = (1 + 2m)\pi/L$  :

---

$$\begin{bmatrix} H_{\sigma r}(r_{ce}, k_m) \\ H_{\tau rz}(r_{ce}, k_m) \\ \Delta H_{\sigma r}(r_{ci}, k_m) \\ \Delta H_{\tau rz}(r_{ci}, k_m) \\ \Delta H_{\varepsilon z}(r_{ci}, k_m) \\ \Delta H_{\varepsilon z}(r_{ci}, k_m) \end{bmatrix}_{6 \times 6} \begin{bmatrix} A_f \\ C_f \\ A_c \\ B_c \\ C_c \\ D_c \end{bmatrix}_m = \frac{4 \left( (\alpha_c - \alpha_f)(T - T_{ref}) + \beta_c (RH - RH_{ref}) \right) (-1)^m}{L k_m^4} \begin{bmatrix} 0 \\ 0 \\ 0 \\ 0 \\ 1 \\ -1 \end{bmatrix} \quad \text{Eq. 316}$$

The Eq. 316 allows to determine the coefficients  $A_f, C_f, A_c, B_c, C_c, D_c$ , for each value of  $k_m$  by expressing the  $H_{\sigma r}, H_{\tau rz}$  and  $\Delta H_{\sigma r}, \Delta H_{\tau rz}$  in terms of the Bessel functions according to the obtained stress solution from Eq. 267 to the Eq. 270 and the  $\Delta H_{\varepsilon \theta}, \Delta H_{\varepsilon z}$  by employing the relations from Eq. 293 to the Eq. 296. From the Eq. 316 it's possible to note that, as expected, the forcing term on the right side is null in the reference condition; therefore, in this condition, the equation system has only the null solution for each  $k_m$  and all the stress and strain components are identically zero everywhere.

# **CHAPTER 4**

## **FIBER OPTICAL SENSORS FOR CRYOGENIC TEMPERATURE MONITORING IN LHC**

### **4.1. MOTIVATIONS**

As described in the Chapter 1, in the LHC at CERN many different kinds of magnets are employed to accelerate and direct the particle beams on the curved path of the collider: 1232 dipole magnets to bend the beams and 392 quadrupole magnets for focusing the beams and increase the chances of collisions. The superconducting magnets are cooled by a massive cryogenics system: these need in fact extreme cooling conditions to preserve the internal superconductivity highly crucial for their performances. The magnets coils, built with NbTi based superconductors, are cooled through a distribution system of Liquid He which allows them to reach an operative temperature of 1.9 K, meaning  $-271.3^{\circ}\text{C}$ .

---

Currently, the main cost of superconductivity is the cooling process. Whatever energy is earned through the use of superconducting wires is lost in the energy needed to cool the wires. But CERN researchers are working on a way to use superconducting cables for the entire journey from source to magnet, which would lower the energy required to cool the wires [2]. In LHC monitoring temperature is therefore a crucial aspect to control the temperature operative condition of the equipments in order to secure the minimal power loss in the power transmission and prevent damages to the superconductive elements.

The employment of the FBG sensors, which allow measurements in extreme environmental conditions with also very high immunity toward the strong electromagnetic field, is therefore particularly suitable also for this kind of High Energy Physics Cryogenic applications. In addition it's possible to get benefits from all their classical advantageous aspects, such as compactness, lower cost of the devices for the data acquisition, low attenuation of the optic signal, very large temperature value operative range, high precision and fast response. Through their multiplexing capability obtained by linking in series different FBGs with different Bragg reference wavelengths, temperature in hundred points can be monitored with a very limited number of optical fibers.

For this reason, many authors have studied the FBG sensor behavior also in cryogenic conditions, mainly for strain, temperature and structural health monitoring. Nevertheless it must be considered that, at those cryogenic temperature, the sensitivity of a standard commercial FBG sensitivity is very low; typical values are reported in the Table 2:

<i><math>\lambda</math> Shift Sensitivity</i>	<i>Temperature</i>
<i>8 - 12 pm/K</i>	<i>room Temperature</i>
<i>&lt; 0.1 pm/K</i>	<i>below 40 K</i>

*Table 2- Values of an commercial FBG sensitivity at room and cryogenic temperatures*

In order to prototype new FBG sensors for such extreme conditions of cryogenic applications, active coating materials with a large thermal expansion coefficient (CTE) in the temperature range from 4 K to 300 K, must

---

be employed to increase the induced variation of the Reflected Bragg Signal and overcome the low values of temperature sensitivities for an commercial FBG at cryogenic temperature reported in the Table 2.

For this purpose, 2 polymeric materials based on EPOXY and Methacrylate (PMMA) were tested for the FBG coating to check their suitability for the use in Cryogenic temperature monitoring of the superconducting magnets. Epoxy and PMMA have been chosen and preferred to other coating materials for their large thermal expansion coefficients and for their excellent adhesion to the surface of the fiber, which can assure an optimal stress distribution at the fiber-coating interface.

#### 4.2. DESIGN CHOICE OF THE ACTIVE COATED FBG THICKNESS

In order to achieve an adequate level of sensitivity for the Active Coated FBGs to be manufactured, the choice of the coating thickness was crucial. For this reason preliminary simulations were carried out by employing the mechanical model developed in Chapter 3 of present thesis and solving the Eq. 316 using the material properties and geometrical parameters reported in the Table 3.

<i>Parameter</i>	<i>Symbol</i>	<i>Value</i>
<i>Fiber Radius (cladding included)</i>	$r_{ci}$	62.5 $\mu\text{m}$
<i>Coating Radius</i>	$r_{ce}$	62.5 $\mu\text{m} \div 2.5 \text{ mm}$
<i>Glass Fiber Elastic modules</i>	$E_c$	70 GPa
<i>Coating Elastic modules</i>	$E_f$	3 GPa
<i>Glass Fiber Poisson Coefficient</i>	$\nu_f$	0.3
<i>Coating Poisson Coefficient</i>	$\nu_c$	0.3
<i>Glass Fiber Thermal Expansion Coefficient</i>	$\alpha_f$	2 $\mu\epsilon/\text{K}$
<i>Coating Thermal Expansion Coefficient</i>	$\alpha_c$	100 $\mu\epsilon/\text{K}$

*Table 3- Coated FBG material and geometric parameters for the preliminary simulations to evaluate the FBGs sensitivities*

From the performed simulations, an important result was achieved. Indeed, for the order of magnitude of the material parameters reported in the Table 3, the  $\varepsilon_f(r, z)$  and  $\varepsilon_c(r, z)$  strain fields resulted only weakly dependent by  $r$  and  $z$ , so that they could be assumed almost uniform in both the glass fiber and coating zone. Thus, since at the interface they must also be the same, with very good approximation, we can write :

$$\varepsilon_f^{tot} \cong \varepsilon_c^{tot} \equiv \varepsilon \quad \forall r, z \quad \text{Eq. 317}$$

And therefore:

$$\varepsilon_f^{th} + \varepsilon_f^{el} \cong \varepsilon_c^{el} + \varepsilon_c^{th} + \varepsilon_c^{sw} = \varepsilon \quad \text{Eq. 318}$$

i.e. the total strain in the fiber zone equals the total strain in the coating zone. Of course, using the relation above,  $d\lambda/\lambda$  expressed by the Eq. 120 becomes:

$$\frac{d\lambda}{\lambda} = \xi dT + (1 - p_e)d\varepsilon \quad \text{Eq. 319}$$

Where  $\varepsilon$  is the common total strain of fiber and coating. This justify the introduction of an equivalent thermal expansion coefficient of the whole FBG sensor:

$$\alpha_{sensor}(T) = \frac{d\varepsilon}{dT} \quad \text{Eq. 320}$$

Substituting the Eq. 320 in the Eq. 319, we obtain:

$$\frac{d\lambda}{\lambda} = [\xi + (1 - p_e)\alpha_{sensor}]dT \quad \text{Eq. 321}$$

$$\frac{1}{\lambda} \frac{d\lambda}{dT} = \xi + (1 - p_e)\alpha_{sensor} \quad \text{Eq. 322}$$

For a temperature coated sensor based on the FBG, we can neglect the coating swelling and assume  $\varepsilon_c^{sw} = 0$ ; from the Eq. 318 we obtain:

---

$$\varepsilon_f^{el} = \varepsilon - \varepsilon_f^{th} \quad \text{Eq. 323}$$

$$\varepsilon_c^{el} = \varepsilon - \varepsilon_c^{th} \quad \text{Eq. 324}$$

In the case of a temperature variation applied to the coating a difference in tension respect to the fiber is generated due to the thermal expansion coefficient mismatch between the different materials. Detailing the mechanical constraints acting on the fiber optic, it is therefore possible to evaluate the effective deformation experienced by the FBG sensor; of course the deformation is determined by the thermal expansion coefficient of the optical fiber constituent material. The balancing of the resulting thermal forces along the fiber axis allows the determination of the common deformation of the coating and the fiber: for the axial force equilibrium (along z) it must also be verified:

$$F_{zc} + F_{zf} = 0 \quad \text{Eq. 325}$$

The axial force is given by:

$$F_z = A\sigma_z \quad \text{Eq. 326}$$

Where A is the areal section on which the stress acts. By neglecting the Poisson effects from the Eq. 147 and Eq. 148, it results:

$$\sigma_{zc} = E_c \varepsilon_c^{el} \quad \text{Eq. 327}$$

$$\sigma_{zc} = E_f \varepsilon_f^{el} \quad \text{Eq. 328}$$

By employing the relations Eq. 323, Eq. 324 and substituting in the Eq. 325, one has:

---

$$\pi(r_{ce}^2 - r_{ci}^2)E_c(\varepsilon - \varepsilon_f^{th}) + \pi r_{ci}^2 E_f(\varepsilon - \varepsilon_f^{th}) = 0 \quad \text{Eq. 329}$$

Defining the longitudinal stiffness, respectively of the coating,  $H_c$  and the glass fiber,  $H_f$  as:

$$H_c = \pi(r_{ce}^2 - r_{ci}^2)E_c \quad \text{Eq. 330}$$

$$H_f = \pi r_{ci}^2 E_f \quad \text{Eq. 331}$$

and solving the Eq. 329 with respect to  $\varepsilon$ , we obtain:

$$\varepsilon = \frac{H_f \varepsilon_f^{th} + H_c \varepsilon_c^{th}}{H_f + H_c} \quad \text{Eq. 332}$$

Then, differentiating the Eq. 332 with respect to the temperature we have:

$$\alpha_{sensor} = \frac{d\varepsilon}{dT} = \frac{H_f \alpha_f + H_c \alpha_c}{H_f + H_c} \quad \text{Eq. 333}$$

Finally, by substituting in the Eq. 322, we get:

$$\frac{1}{\lambda} \frac{d\lambda}{dT} = \xi + (1 - p_e) \frac{H_f \alpha_f + H_c \alpha_c}{H_f + H_c} \quad \text{Eq. 334}$$

Moreover, by considering constant, in first approximation, the properties of the materials as function of the temperature, both the members of Eq. 334 can be easily integrated to obtain a relation correlating the lambda shift with the temperature and the thermal expansion coefficient of the materials, starting from as assigned reference status  $(T_0, \lambda_0)$ :

$$\int_{\lambda_0}^{\lambda} \frac{d\lambda}{\lambda} = \int_{T_0}^T \xi + (1 - p_e) \frac{\alpha_f H_f + \alpha_c H_c}{H_f + H_c} dT \quad \text{Eq. 335}$$


---

$$\ln\left(\frac{\lambda}{\lambda_0}\right) = \left[ \xi + (1 - p_e) \frac{\alpha_f H_f + \alpha_c H_c}{H_f + H_c} \right] (T - T_0) \quad \text{Eq. 336}$$

$$\lambda = \lambda_0 \exp\left( \left[ \xi + (1 - p_e) \frac{\alpha_f H_f + \alpha_c H_c}{H_f + H_c} \right] (T - T_0) \right) \quad \text{Eq. 337}$$

#### 4.2.1. ACTIVE COATED FBG CRYOGENIC SENSORS SENSITIVITY

From the Eq. 336, it's natural to define a logarithmic sensor sensitivity evaluated in the logarithm scale:

$$S_{T \log} \equiv \frac{d}{dT} \ln\left(\frac{\lambda}{\lambda_0}\right) = \xi + (1 - p_e) \frac{\alpha_f H_f + \alpha_c H_c}{H_f + H_c} \quad \text{Eq. 338}$$

By employing the coating and fiber stiffness, Eq. 330 and Eq. 331, the logarithmic sensor sensitivity can be expressed as function of the coating thickness:

$$S_{T \log} = \xi + (1 - p_e) \frac{r_{ci}^2 E_f \alpha_f + (r_{ce}^2 - r_{ci}^2) E_c \alpha_c}{r_{ci}^2 E_f + (r_{ce}^2 - r_{ci}^2) E_c} \quad \text{Eq. 339}$$

Of course, in order to calculate the sensitivities of the FBGs to be manufactured as function of the coating thickness, the physical properties of FBG at cryogenic temperature were needed. As well explained in [1], many authors studied the physical properties influencing the Bragg response at cryogenic temperature.

For example Rajinikumar et al. [19] have evaluated the thermo-optic coefficient, the photo-elastic coefficient, the glass thermal expansion coefficient as function of temperature in the wide range 4-300 K. In his work FBGs were tested at cryogenic conditions and coated with metal materials to enhance the sensor sensitivity at low temperature. The calculated values of the sensitivity resulted anyway lower than the sensitivity achievable through polymer coating due the difference between the CTE of the tested metals and the CTE of an epoxy or PMMA.

Mizunami et al.[20] measured at low temperature the temperature sensitivity of FBG sensors fixed on a Teflon substrate, which have showed an higher sensitivity compared to other substrate materials. It was found that the temperature sensitivity was even higher than the sensitivity achievable by using a PMMA substrate; however the main inconvenience relies on the epoxy adhesive layer required to fix the FBG to the Teflon substrate.

James et al. [21] evaluated the temperature sensitivity of the nude FBGs down to 2.2 K. Habisreuther et al. [22] analyzed instead the response at cryogenic temperatures of Ormocer (an hybrid polymer material synthesized by a sol-gel process) coated FBG sensors: at 10 K, the thermal expansion coefficient for the Ormocer coated fiber resulted  $1.5 \cdot 10^{-6} \text{ K}^{-1}$ .

Tanaka et al. [23] tested FGB sensors at cryogenic conditions under high magnetic fields confirming the magnetic field immunity, while Latka et al. [24] showed the negligibility of the thermo-optic and magneto-optic effects in cryogenic environments for FBG strain sensors employed for the structural health monitoring of superconductors when subjected to significant forces generated by strong magnetic fields.

According for example to Rajinikumar et al.[19], the photo elastic constant in the Eq. 334 can be assumed as:

$$p_e = -\frac{\partial n}{n \partial \varepsilon} \approx 0.23 \quad \text{Eq. 340}$$

While for the thermo optic coefficient  $\xi$  of silica at room temperature appearing in the same equation Eq. 334, again according to [19], the following value can be employed:

$$\xi = \frac{\partial n}{n \partial T} \approx 8 \text{ ppm/K} \quad \text{Eq. 341}$$

The values of  $p_e$  and  $\xi$  reported in the Eq. 340, Eq. 341, in combination with the needed values of the material properties, Table 3, allowed a preliminary estimation of the sensor sensitivity by employing the Eq. 336. The results are reported in the Figure 26. From the Figure 26 it's possible to see that for thickness

---

higher than 1mm, saturation of the sensitivity was obtained. A thickness of 2.5 mm was finally chosen to ensure an adequate level of sensitivity to the Active Coated FBG to manufacture.

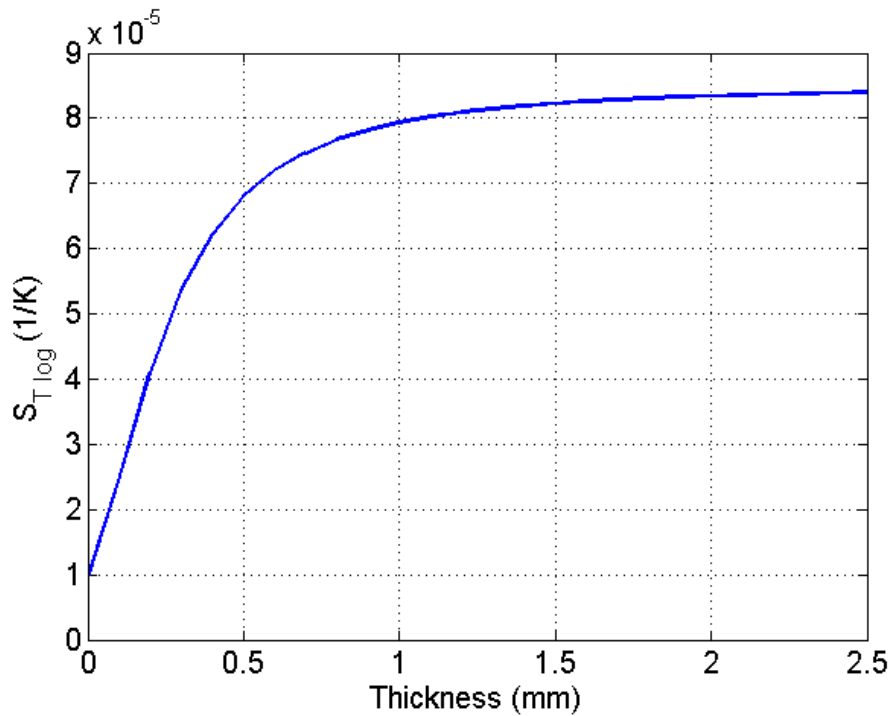


Figure 26 – Logarithmic Sensor Sensitivity as function of the Active Coating thickness

### 4.3. SAMPLES PREPARATION

The coated FBGs prototypes were manufactured by Optosmart in partnership with the Institute for Composite and Biomedical Materials of the National Research Council CNR-IMCB, Italy, for the first cryogenic test campaign at CERN. The sensors were manufactured with two different coating materials, EPOXY and PMMA. Two different reference wavelengths of each material were also employed. The uncovered Fiber Bragg Gratings were provided by Welltech Instrument Company Limited (Hong Kong) with the following specifications: grating length 10mm, Bragg wavelength tolerance +/- 0.5nm, reflectivity >90%, FWHM (full width at half maximum of the spectrum) <0.3 nm.

---

### **4.3.1. COATING MATERIALS**

Polymeric coatings around FBGs were produced using two classes of polymeric precursors: epoxy and acrylic. For the epoxy based polymer, precursors are DiGlycidyl ether of Bisphenol-A (DGEBA) high purity liquids with an Epoxy Equivalent Weight (EEW) of 170-175 g/mole, multi-functional aliphatic amine as hardener and a tertiary amine as catalyst. The employed epoxy system was supplied by Elantas Camattini (Italy) under the label, EC-170 + IG 824 -K24. PMMA precursors were arranged in a two component system: a very fine PMMA powder mixed with a peroxide catalyst and a liquid mixture, characterized by the presence of methylmethacrylate monomers, crosslinking agent and initiator. The acrylic system was supplied by Heraeus (Paladur). The powder and the liquid mixture were premixed in the right proportion and then quickly used due to its rapid reaction time (within a few minutes).

### **4.3.2. COATING METHODS**

Epoxy based and acrylic polymers were obtained starting from its liquid precursors by in situ polymerization, then reactive casting was employed as most suitable manufacturing process to manufacture the Active Coated FBG samples.

This solution allows producing an interface between polymeric material and fiber cladding, which ensures an efficient strain transfer from the polymer system to fiber. Polymer precursors are liquid and highly compatible with silica, which represents the main constituent of the fiber cladding, and thus a good surface wetting could be achieved before polymerization.

After the fiber was cleaned with isopropyl alcohol, the polymeric material was casted around the cladding section near the Bragg grating. The final nominal dimensions of coating of the fiber containing the Bragg grating were 2.5 mm height, 5.0 mm width, 25.0 mm length.

---

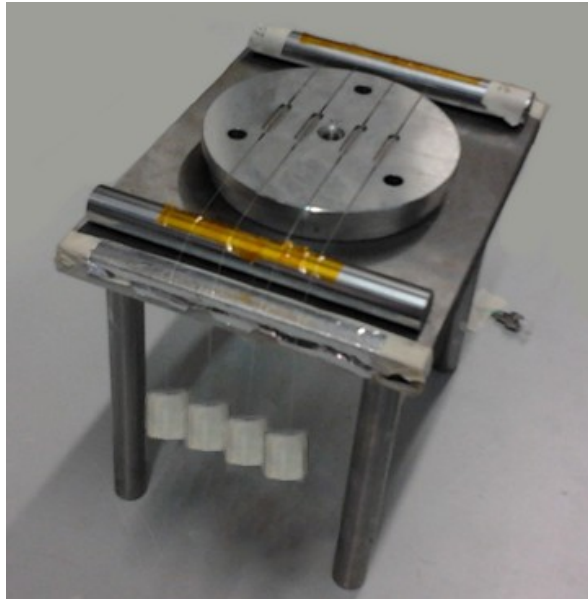


*Figure 27 - Mould set up for manufacturing of polymer coating on FBG fiber*

To carry out the manufacturing process by reactive casting, an optimized mould was used; the inferior half mould is reported in the Figure 27. In the manufacturing setup, a constrain system was designed in order to induce pre-alignment and pre-stress to the FBG sensor and at the same time to control the chemical shrinkage due to the polymerization reaction during the first curing stage.

An extra post-curing stage was considered for both reactive systems by using a constrain-free configuration; this to allow the natural rearrangement of the system and to reduce the local interfacial stresses between polymer coating and cladding near the FBG grating. Both systems exhibited a very low viscosity at room temperature, which facilitates the casting process but, conversely, it allows air inclusions during premixing operation. To overcome this inconvenience, mixing stage was performed by using a planetary mixer under vacuum (10 kPa abs) at room temperature.

For the epoxy based system, all components were premixed in the right proportion according to supplier data sheet in order to obtain a reactive mixture and then degassed to prevent gas entrapment in the final product. After degassing the casting was performed in a few seconds. The curing profile was then divided a preliminary curing stage at room temperature for 12 h followed by a post-curing stage at 100 °C for 4 h. For

---

the acrylic system the first polymerization stage was very fast, as gelation occurred in a few minutes and solidification in less than 1 hour. Post curing stage was the same as for epoxy system.

#### 4.4. EXPERIMENTAL SET UP FOR CRYOGENIC TEMPERATURE MEASUREMENTS AT CERN

At CERN Cryo Lab, the samples were positioned in a dedicated sample holder and then inserted into the cryostat as shown in the following Figure 28(a):

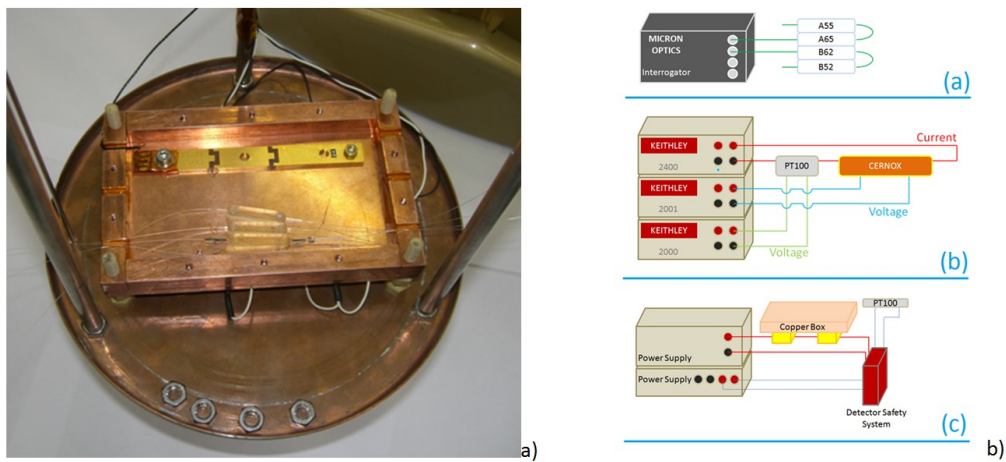


Figure 28 – a) Experimental setup. b) Schematic drawing of the DAQ: The optical measurement (a), the readout of the reference temperature sensors (b) and the heater with the Universal transmitter - DSS (c).

The FBG sensor holder consisted in a small copper box assuring a good thermal stability among the FBG fibers and the reference temperature sensors.

Two temperature sensors, one of a type CERNOX™ and another thermo resistive Platinum thermocouple (PT100), previously calibrated, were used to monitor the ambient temperature. The cooling down of the system was performed by using liquid helium pumped into the cryostat until the final temperature reached 4.2 K. In order to control the warm-up, resistors were placed at the bottom of the sample holder.

The two temperature sensors were connected electrically in series and powered by a Keithley 2400 source meter operating in a constant current source mode. Voltage readouts were performed by a Keithley 2000 and a Keithley 2001 precision DMM devices. The resistors were connected to a TTI TSX3510 power supply. All

three Keithleys and the TTI devices were connected to a GPIB bus that controlled by customized software. A schematic diagram showing all the instruments used in the experimental set up for the data acquisition is reported in the Figure 28(b), where the optical measurement (a), the readout of the reference temperature sensors (b) and the heater (c) are drawn.

The 4 active coated FBG prototype sensors tested were located in the sample holder. In order to increase the reliability of the sensors, two epoxy coated FBGs were spliced together to form an array. Both ends of this array were brought out from the cryostat. The same setup was built for the PMMA coated sensors. This configuration, allowed the readout on all sensors from both sides, so data were assured to be recorded even in case of optic fiber break. One end of the epoxy sensors array and one end of the PMMA sensors array were connected to a Micronoptics SM125 interrogator.

#### 4.5. EXPERIMENTAL RESULTS

Figure 29 shows the reflected spectra of the 4 FBG sensors in the reference conditions, i.e at room temperature.

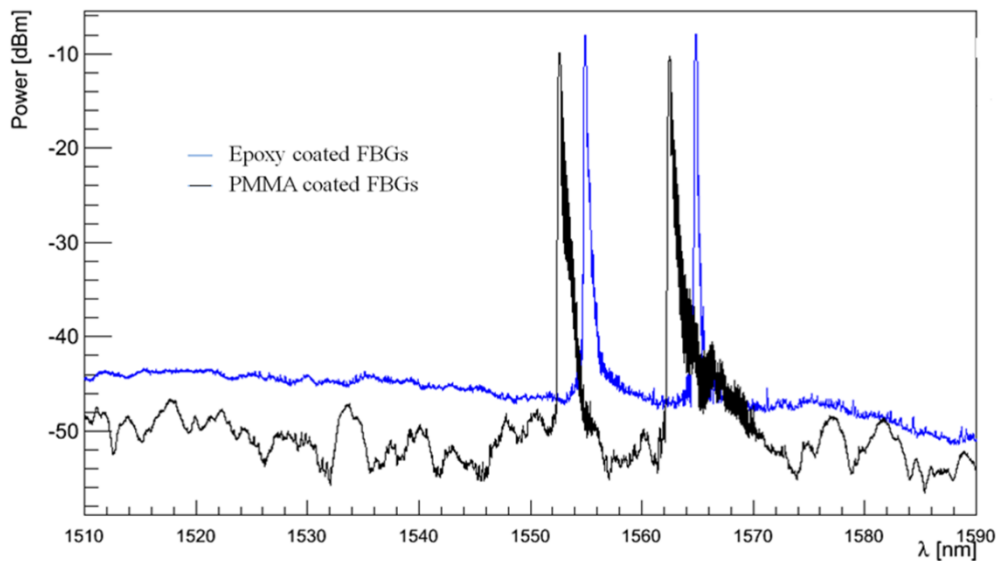


*Figure 29 - Spectral distribution of the reflected light from the FBG sensors on room temperature. Blue line refers to Epoxy coated FBGs array. Black line refers to PMMA coated FBGs array.*

---

From the Figure 29 it's possible to note the 4 peaks in the reflected signal, one for each one of the tested sensor: 2 of them are relative to the Epoxy coated FBGs, blue line, while 2 remaining peaks are relative to the PMMA coated FBGs, black line. The data acquisition of sensor signals was then performed for several cooling down and warm up cycles.

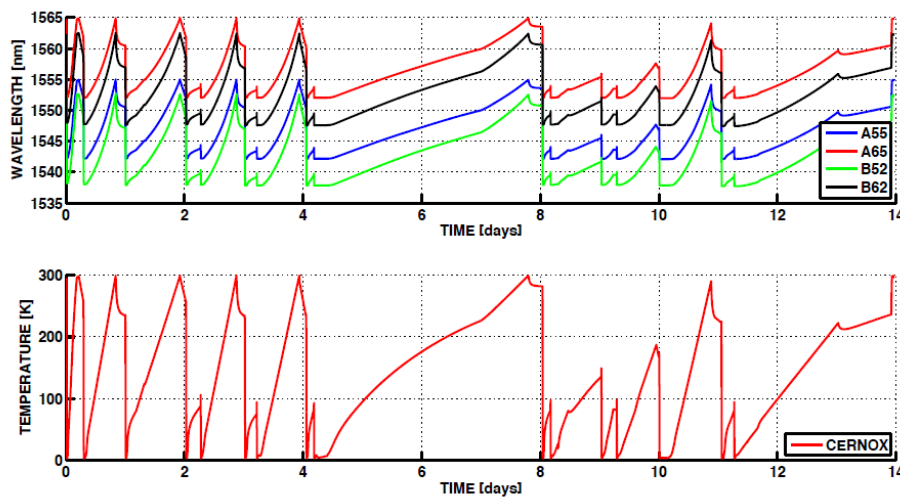


Figure 30 - a) Bragg wavelength of the FBG sensors vs. time. The blue and the red lines represent the epoxy-coated FBGs (A55, A65), the green and the black line represents the PMMA-coated FBGs (B52, B62). b) Reference sensor temperature vs time.

The experimental dataset consists of two types of signal: voltage from the thermal resistive sensors (PT100 and Cernox) and central reflected wavelength signals from FBG sensors. Figure 30(a) shows the temporal evolution of the Bragg wavelength for all the FBG sensors.

The letter A represents the Epoxy-coated sensor while the letter B represents the PMMA-coated sensor. The two digits indicate the sensors reference Bragg wavelength in nanometers at room temperature (e.g. 62 stands for 1562 nm). Figure 30(b) shows the time evolution of the temperature, as measured by the Cernox sensor. In total 16 different warm-up and 16 cool-down steps were performed. Raw data related to the Bragg wavelength and temperature evolution, as reported in Figure 30, were computed according to Eq. 336 normalizing the sensor responses to the room temperature and to the reference Bragg wavelength.

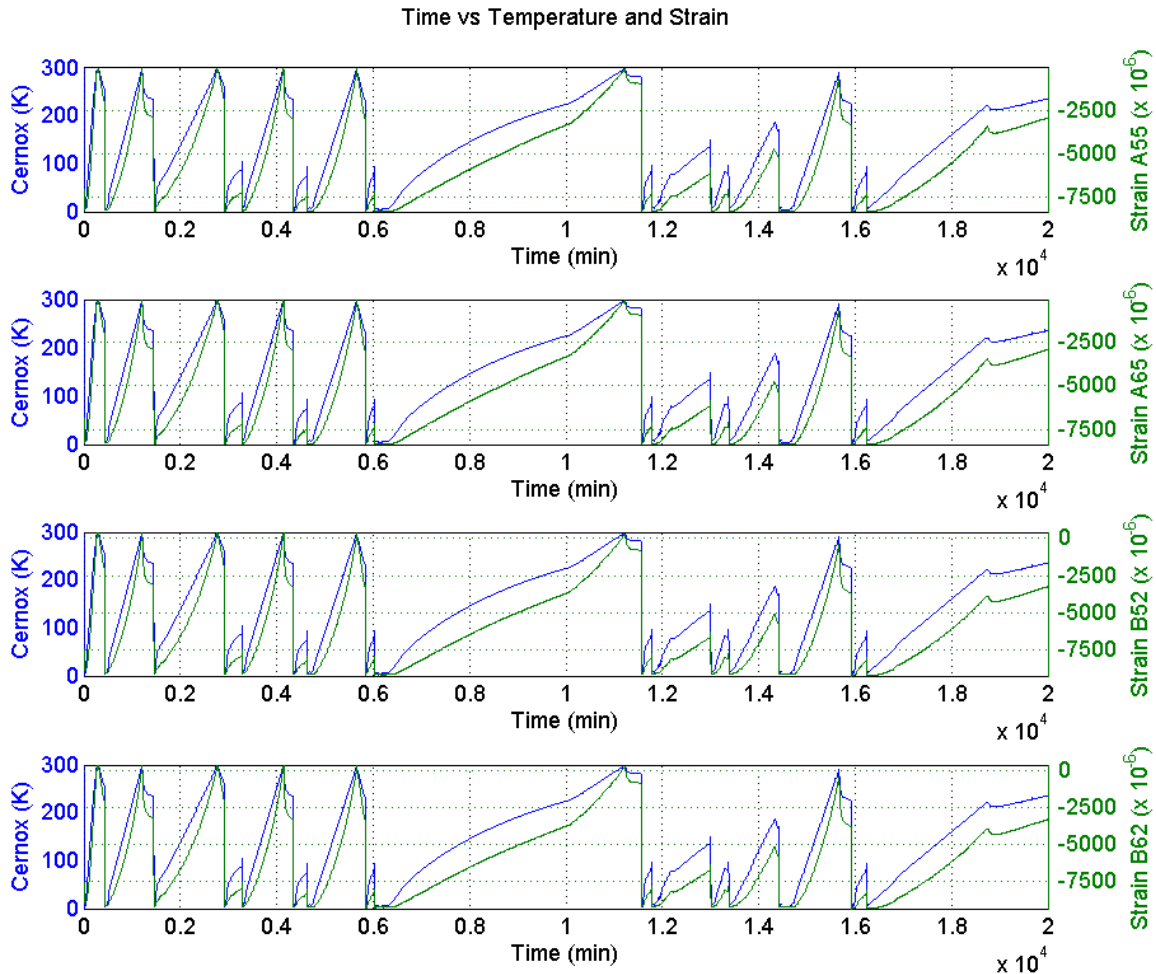


Figure 31 - Time versus Temperature (by Cernox) and Strain for each one of the tested sensors

By employing the Eq. 319, and the photo elastic and thermo optic coefficients, Eq. 340 and Eq. 341 the Figure 31 shows the calculated strain for each one of the tested sensors. The Figure 32 reports the normalized sensors output as a function of the temperature (only warm up test were analyzed). From the figure it's possible to note that Epoxy-coated sensors present in general a smaller change of the Bragg wavelength compared to the PMMA-coated sensors within the range 4-300 K. The Figure 33 shows the normalized sensors outputs in the low temperature range: the Figure 33(a) and 6(b) report the normalized sensors outputs, relative to the Epoxy and PMMA coated sensors, respectively. All the thermal cycles are reported. The Figure 33(c) and Figure 33(d) show the values averaged among all the warming up cycles. The sensitivity of the FBG sensors decreases at low temperatures for both the polymers.

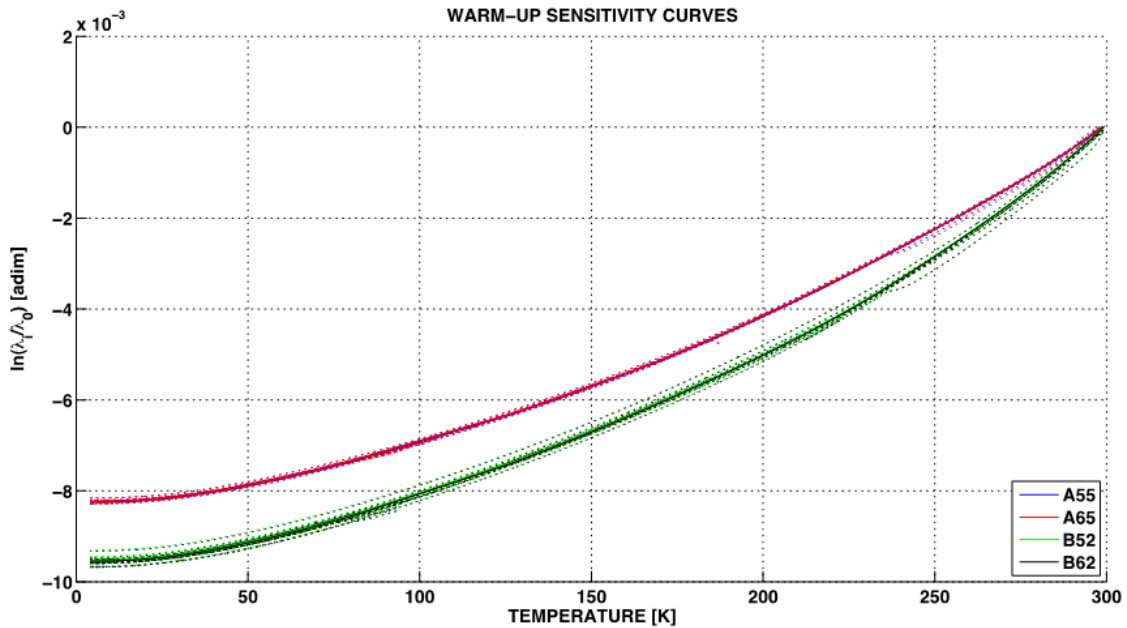


Figure 32 - Normalization to room temperature and reference Bragg wavelength of FBG sensors outputs vs. temperature (only warm-ups). Solid lines are averaged over different warm ups, dotted lines are individual warm-ups outputs.

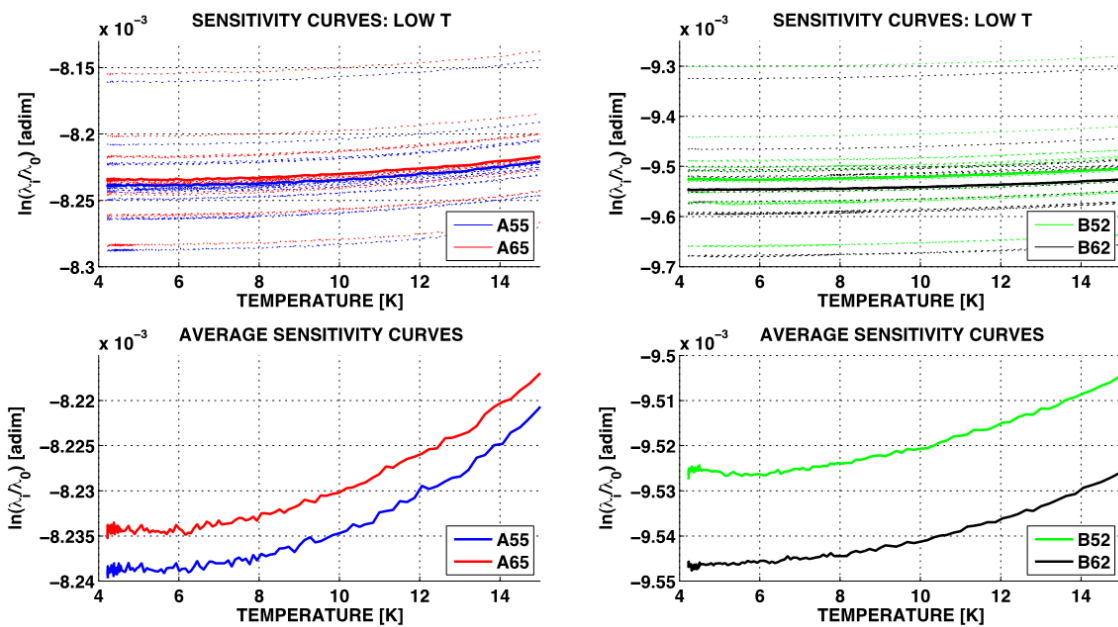


Figure 33 – Zoom plot for normalized sensor outputs from 4 K to 15 K. a) Epoxy-coated sensors. All the warm-ups. b) PMMA-coated sensors. All the warm-ups. c) Epoxy-coated sensors. Average sensitivity curves. d) PMMA-coated sensors. Average sensitivity curves.

## 4.6. EVALUATION OF THE THERMAL EXPANSION COEFFICIENT

The measure of the linear thermal expansion coefficient (CTE) of a material is generally obtained by the experimental data relative to the strain or length changes due to the temperature variations. Starting from the data acquired through the FBG in the test campaign at CERN, a standard numerical derivative method was employed to estimate thermal expansion coefficients of the Active Coating material on FBG. Moreover the correlated fluctuation analysis (CFA) based procedure was also proposed, as a reliable alternative, to overcome numerical derivative drawbacks at very low temperatures within the range of 4 K to 20 K. The calculated values of thermal expansion coefficient for both systems were in agreement with literature data on similar materials and the relative results have been published on a peer reviewed international journal [1].

### 4.6.1. METHODOLOGY

The thermal expansion coefficient of the coating system,  $\alpha_{\text{coating}}(T)$ , can be easily found starting from the Eq. 334; we obtain:

$$\alpha_{\text{coating}}(T) = \frac{H_{\text{glass}} + H_c}{H_c(1 - p_e)} \left( \frac{1}{\lambda} \frac{d\lambda}{dT} - \xi \right) - \frac{H_{\text{glass}}}{H_c} \alpha_{\text{glass}} \quad \text{Eq. 342}$$

The thermal expansion coefficient of the coating material is not only dependent on the thermo and elasto optical properties of the FBG sensor but also on thermo-mechanical properties of the fiber itself and its coating material. Therefore the more accurate analysis of the terms in Eq. 342 is needed.

At Room Temperature (RT), 300 K, the Young modulus of the glass and the polymers, are  $E_{\text{glass}} = 77$  GPa and  $E_{\text{coating}} = 3$  GPa, respectively, according to Takeda [25]. These values lead to the following relative stiffness for the tested sensors:  $H_{\text{glass}}/H_c = 0.015$  @ RT. On the other hand, at very low temperature the polymers Young modulus,  $E_{\text{coating}}$ , increases more than the Young modulus of the silica,  $E_{\text{glass}}$ , with a further arising of the relative stiffness of coating. In particular, at Cryo Temperature (CT), 4 K,

---

the Young modulus of the glass and the polymers are respectively  $E_{\text{glass}} = 83 \text{ GPa}$ ,  $E_{\text{coating}} = 9 \text{ GPa}$  [25] and thus relative stiffness is  $H_{\text{glass}}/H_c = 0.005 @ \text{CT}$ .

Furthermore at Room Temperature, according to Rajinikumar et al.[19], James et al. [21] and Habisreuther et al. [22], the physical properties of the FBG silica are:

$$\alpha_{\text{glass}} = 2.6 \text{ ppm/K}, \quad \xi = 8.59 \text{ ppm/K}, \quad p_e \cong 0.23 \quad \text{Eq. 343}$$

while at low temperatures (4 K), the physical properties of the FBG silica are[19][21][22]:

$$\alpha_{\text{glass}} = 1.0 \text{ ppm/K}, \quad \xi = 1.02 \text{ ppm/K}, \quad p_e \cong 0.23 \quad \text{Eq. 344}$$

The following Table 4 summarizes all the fiber and coating properties at cryo and room temperature:

Temperature	$E_{\text{glass}}$	$E_{\text{coating}}$	$\alpha_{\text{glass}}$	$\xi$	$p_e$
4 K	83 GPa	9 GPa	1.0ppm/K	1.02 ppm/K	0.23
300 K	77 GPa	3 GPa	2.6ppm/K	8.59 ppm/K	0.2

Table 4- List of all the properties at cryo and room temperature of fiber and coating

Based on these values, the following engineering assumptions have been set:

$$H_{\text{glass}}/H_c \cong 0 \quad \text{Eq. 345}$$

$$p_e(T) \cong 0.23 \quad \text{Eq. 346}$$

independently by the temperature. Substituting in the Eq. 334, these assumptions give back:

$$k(T) \equiv \frac{d \ln(\lambda/\lambda_u)}{dT} = \alpha_{\text{coating}}(T)(1 - p_e) + \xi(T) \quad \text{Eq. 347}$$


---

(with  $\lambda_u = 1$  nm), or equivalently:

$$\alpha_{coating}(T) = \frac{1}{1 - p_e} (k(T) - \xi(T)) \quad \text{Eq. 348}$$

$$\alpha_{coating}(T) = \frac{1}{1 - p_e} \left( \frac{d}{dT} \ln \left( \frac{\lambda}{\lambda_u} \right) - \xi(T) \right) \quad \text{Eq. 349}$$

The evaluation of the thermal expansion coefficient of the coating material can be obtained by the estimation of the temperature derivative of the logarithm of sensor outputs,  $\lambda(T)$ . A standard procedure to perform numerical temperature derivative, in according to the Eq. 349 has been applied to the outputs of FBG and temperature sensors. The numerical derivative method needs a continuous monotonically temperature variation to reconstruct the function and thereof its temperature derivative. Due to the poor temperature control in very low temperature range, the numerical derivative algorithm inevitably fails. An alternative method should be implemented to overcome such drawback.

#### 4.6.2. CORRELATED FLUCTUATION ANALYSIS (CFA)

Hereafter, an alternative methodology is proposed to evaluate the CTE based on Correlated Fluctuation Analysis (CFA) of the two time signals, namely the Bragg wavelength shift,  $\ln(\lambda)$ , and temperature,  $T$ . The fluctuation analysis has been performed by dividing the temperature history in short temporal intervals,  $I$ , in which the temperature is almost constant. In these conditions the relationship between temperature  $T$  and  $\ln(\lambda/\lambda_u)$  can be considered linear, thus from the Eq. 336 we can write:

$$\ln \left( \frac{\lambda}{\lambda_u} \right) (t) = k_i \cdot T(t) + c \quad \text{Eq. 350}$$

where  $i$  indicates the  $i$ -th interval and  $k_i$  is provided by Eq. 347. Under these hypothesis, for the  $i$ -th set of points, for the expected value  $E\{\}$  and variance  $\text{Var}\{\}$ , it results:

---

$$E \left\{ \ln \left( \frac{\lambda}{\lambda_u} \right) \right\}_i = k_i E\{T\}_i + c \quad \text{Eq. 351}$$

$$\text{Var} \left\{ \ln \left( \frac{\lambda}{\lambda_u} \right) \right\}_i = k_i^2 \cdot \text{Var}\{T\}_i \quad \text{Eq. 352}$$

or, equivalently:

$$k_i = \frac{\sigma_{\ln(\lambda/\lambda_u)}_i}{\sigma_{T_i}} \quad \text{Eq. 353}$$

$$k_i = \sqrt{\frac{\text{Var}\{\ln(\lambda/\lambda_0)\}_i}{\text{Var}\{T\}_i}} \quad \text{Eq. 354}$$

where  $\sigma_{\ln(\lambda/\lambda_u)}$  and  $\sigma_T$  are, respectively, standard deviations relative to the  $i$ -th interval of the logarithm of Bragg wavelength shift and of the temperature. Once calculated  $k_i$  the thermal expansion coefficient can be found through the Eq. 348:

$$\alpha_{\text{coating}}(E\{T\}_i) = \frac{1}{1 - p_e} (k_i - \xi) \quad \text{Eq. 355}$$

The time duration of each sub interval  $i$ , was chosen such as the corresponding temperature variation within the sub-interval was less than 0.3 K.

## 4.7. RESULTS AND DISCUSSION

The thermal expansion coefficients of coating polymers were obtained by computing both methods: i.e. by evaluating the temperature derivative and by performing the CFA based procedure. Figure 34 shows the estimated CTE values (averaged over the all warm-ups) accounting the sensor raw data (different for coating material employed and reference Bragg wavelength) according to the numerical temperature derivative method without considering the thermo-optic effect.

---

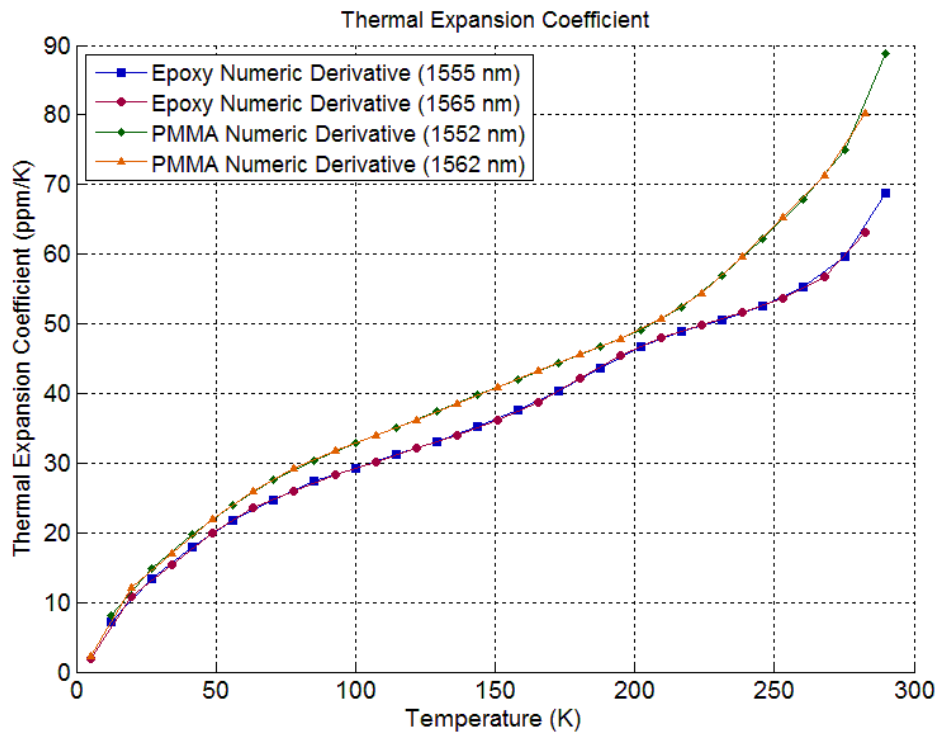


Figure 34 - Thermal expansion coefficient obtained through numeric derivative from sensors with different reference Bragg wavelength data averaged on all the warm-ups.

Analysis performed on different FBG sensors coated by the same material gives CTE values substantially identical. Similar results have been obtained with the fluctuation analysis procedure.

Figure 35(a) and Figure 35(b) report respectively, for each of the indicated material and employed algorithm, the mean and the standard deviation. These latter values were computed by taking into account all curves (one for each warm-up step from 4 to 300 K) of the thermal expansion coefficient as function of the temperature achieved without considering the thermo-optic effect. On the same graph, literature data for similar material systems were reported as dotted points [26].

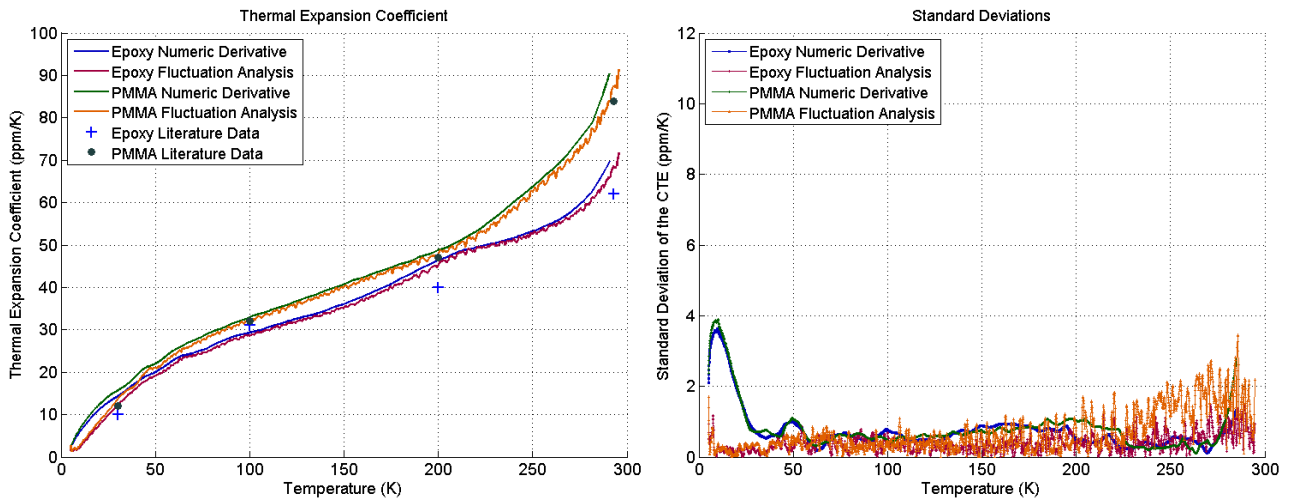


Figure 35 - a) Thermal expansion coefficients of Epoxy and PMMA (averaged on all the warm-ups) without considering thermo-optic coefficient. b) Standard deviation of the thermal expansion coefficient for the Epoxy and the PMMA thermo-optic coefficient without considering thermo-optic coefficient.

Good agreement was found between the two methods for the estimation of the thermal expansion coefficient in the temperature range between 50-300 K, while remarkable discrepancies were found in the very low temperature range between 4-50 K.

Estimated values of the thermal expansion coefficients for epoxy and PMMA systems used in this study have been compared with literature data regarding similar material systems [26] showing an excellent agreement. Very interestingly, the numerical derivative method provides a worse estimation of the CTE values within the low temperature range. In the range 4-20 K the standard deviations are of the same order of magnitude of the estimated CTE values. This effect is probably due to the fact that numerical derivative method needs a continuous monotonically temperature variation to reconstruct the function and thereof its temperature derivative, while fluctuation analysis do not require this constrained conditions. In particular, correlated fluctuation analysis method has been proposed, in this work, to overcome limitations arising from a not ideal temperature and Bragg wavelength signal synchronicity (from diffusive time lags and analog signals synchronization) and a not monotonic temperature variations (due to the not perfectly controlled temperature

ramping). It is worth noting that correlated fluctuation analysis is well performing also in the temperature range where a numerical derivative method results ineffective.

Figure 36 shows a close up of the thermal expansion coefficients in the low temperature range 4-50 K. In this range the two methods provide significant difference in the thermal expansion coefficients estimates. Most relevant is the concavity of the function  $\alpha_{\text{coating}}(T)$ . CFA analysis registers a level off of the thermal expansion coefficients just below 10 K, while numerical derivative method suggests a sharp decrease of the thermal expansion coefficient within the same range.

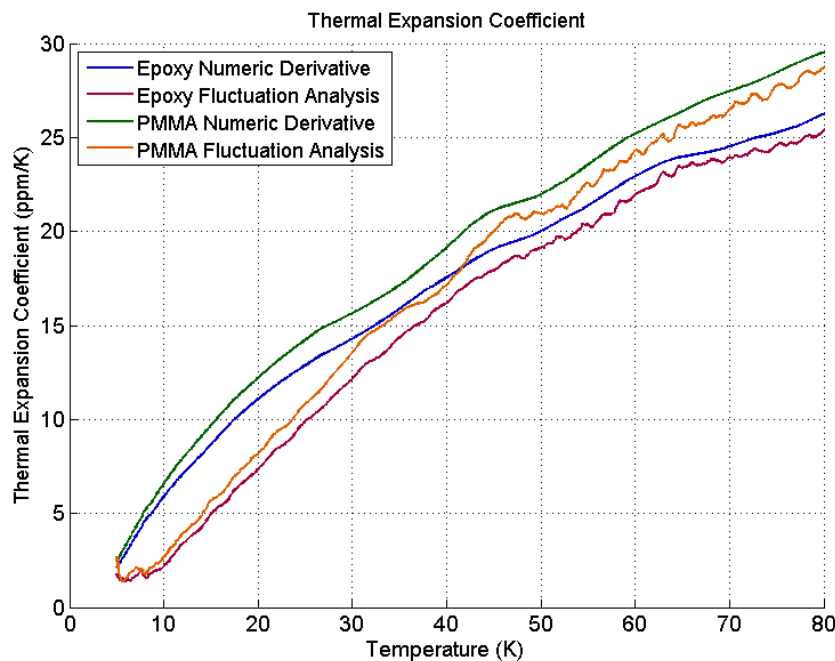


Figure 36 - Thermal expansion coefficient (zoom at low temperatures)

In particular, CFA analysis suggests a strong non linearity within the range 4-10 K. In this range, defined as Debye temperature range, maxima of the thermal expansion coefficient have been already reported [26]. The 4-10 K range will be matter of further and dedicated experimental investigations. From the showed results it's evident that for both the Epoxy and PMMA the thermal expansion reduces drastically at very low temperature and therefore the sensitivity of the sensors become very small or null; thus they are not suitable

to be employed in this temperature range. Finally, Figure 37 shows thermal expansion coefficient predictions obtained by using Rajinikumar et al. [19] measurements of the temperature dependent thermo-optic coefficient.

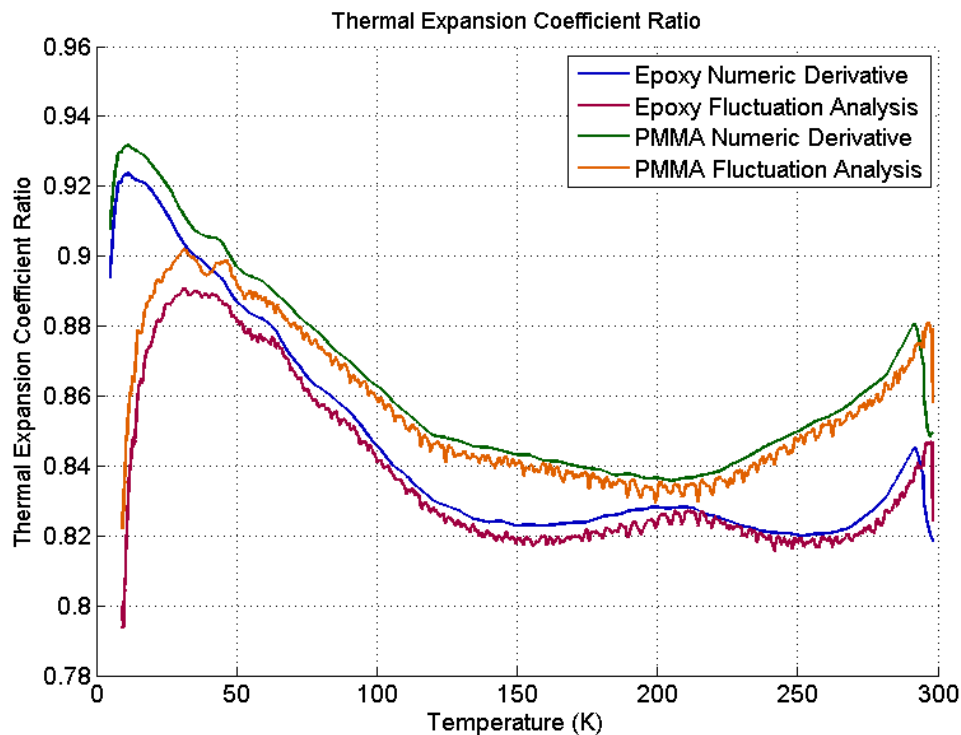


Figure 37 - Ratio between the thermal expansion coefficients obtained considering and not the thermo-optic effect

As a matter of fact, neglecting the thermo optic coefficient will introduce a maximum 20% overestimation of the CTE values, as showed in the Figure 37 by the ratio between the CTE values obtained considering thermo optic effect and those achieved without taking into account this effect.

#### 4.8. CONCLUSIONS

FBGs have been used to evaluate the thermal expansion coefficients of two coating polymeric materials: an epoxy and a PMMA resin, in order to verify their possible use as active coating for a cryogenic temperature FBG sensor manufacturing. In general, the response to a temperature change of an Active Coated FBG

---

depends on the physical properties of the fiber (thermo-mechanical, thermo-optical and elasto-optic properties), on the thermo-mechanical properties of the Active Coating material and on the geometry of the assembly, i.e. fiber radius and the coating thickness. Such a complex interplay between these factors makes very complex the response of the coated FBG sensor to the temperature variations. The potential application of this sensor system for the evaluation of the thermal expansion coefficient of the coating material requires an appropriate design. In particular, the thickness of the coating could be chosen in order to set the stiffness of the coating in respect to that of the sensor. In fact, when  $H_c \gg H_{\text{glass}}$ , the temperature response of the coated FBG is dominated by the thermal expansion coefficient of the coating. Based on this engineering approximation, the thermal expansion coefficients of an epoxy resin and a PMMA have been evaluated accounting for both the elasto-optic coefficient and thermo-optic coefficient of the optical fiber in a wide range of temperature, i.e. 4-300 K. Results for the two polymers have been compared with literature data for similar polymeric systems resulting in an excellent agreement.

Thermal expansion coefficient requires the evaluation of sensor output variation due to the temperature variation. The standard numerical temperature derivative method suffers of serious drawbacks due to the phase mismatch between the two experimental signals, mostly in the very low temperature range where temperature control is difficult. To overcome such problems a method based on the analysis of the fluctuations of the two signal has been proposed such as a correlated fluctuation analysis based procedure. Comparison between the direct calculation from the sensors output of the numerical temperature derivative and the CFA method have showed that thermal expansion coefficients evaluation are consistent and at in the very low temperature range, the so called Debye temperature range (4-10 K), the CFA produces better estimates.

Main results of the present work are: a) the demonstration of the efficiency of FBG sensor in the measurement of the coating material thermal expansion coefficient down to cryogenic temperatures, b) the proposal of a methodology based on the correlated analysis of the FBGs outputs and the temperature sensors to evaluate the thermal expansion coefficient extending the data interpretation in the Debye temperature

---

range (4-10 K) and c) the suitability of the Epoxy and PMMA coatings to be employed for cryogenic temperature monitoring in the wide range 4-300 K. The level of the sensitivity assured to the sensor by their thermal expansion coefficient is very good in the range from 30 K to 300K, with a reduction only observed in the very low temperature range, from 4K to 30K.

---

# CHAPTER 5

## FIBER OPTICAL RELATIVE HUMIDITY SENSORS FOR HIGH ENERGY PHYSICS APPLICATIONS

### 5.1. MOTIVATIONS

One of the fundamental factors causing damage and high levels of noise signals in the Silicon Tracker System in CMS is the exposition to high levels of radiations caused by the very low distance from the interaction point where particle collisions occur, being the Tracker the most close equipment to the central beam pipe of the CMS. Ionizing and non-ionizing radiations cause an increasing of the leakage current which is also source of heat generation. In most critical regions of CMS Pixel Tracker the expected cumulative level of radiations is 200 kGy, after integrated luminosity of  $100 \text{ fb}^{-1}$  in 3 year data taking, corresponding

---

to the RUN2 (period 2015-2018) and in additional 600 kGy after accumulation of further 300 fb<sup>-1</sup> integrated luminosity, after further 3 years of data taking, corresponding to the RUN3 (period 2021-2023). These levels of irradiation dose decrease by almost a factor 10 in the largest volume of CMS Tracker (more external Pixel layers and Strips region). In order to reduce the noise level and increase its operative lifetime, the Tracker System must be kept at a negative Temperature, and therefore cooled by circulating fluids to maintain the adequate operative thermal conditions. The operative temperature must be kept between -20°C and -30°C. At these temperatures, the most important parameter to keep under control in the Tracker volume is the Relative Humidity (RH). Indeed if the temperature is too low to reach the saturation conditions, Dew Point Temperature, the water molecules will condensate to the liquid state, and then quickly to the solid one (ice) due to the negative temperature. This circumstance represent a severe risk for the Tracker System, causing significant damage for the readout electronics of the silicon modules of the Tracker. For this reason the design of an efficient control of the relative humidity in the whole volume is crucial in order to maintain secure it dry.

## 5.2. HUMIDITY DEFINITION

In order to specify the humidity in terms of the vapor content in the air, two main parameters can be employed: they are the Absolute Humidity (H) and the Relative Humidity (RH). The Absolute Humidity is defined as the ratio, for an unitary volume, between the vapor mass content and the whole mass of the thermodynamic system constituted by dry air and vapor:

$$H = \frac{m_v}{m_a + m_v} \quad \text{Eq. 356}$$

where  $m_v$  is the vapor mass while  $m_a$  is the air mass in the reference volume. The employment of this quantity to measure the vapor content presents the drawback of not giving any information about the degree of saturation of the mixture air-vapor at the temperature and pressure operative conditions assigned. In order to overcome this drawback, the Relative Humidity (RH) is introduced. It's defined as the ratio between the

---

density  $\rho_v$  of the vapor in the mixture and the density  $\rho_{vs}$  of the vapor in the saturation conditions, for an assigned level of temperature and pressure:

$$RH = \frac{\rho_v}{\rho_{vs}(p, T)} \tag{Eq. 357}$$

The RH parameters reaches its maximum value (100%) when the vapor has the same density of the saturated vapor. The following Figure 38 (Carrier psychrometric diagram), relative to a pressure value of 1 atm, shows the correlation between H and RH. In the figure it's possible to see the saturation curve (100% RH) and the dry air curve (corresponding to the x axis).

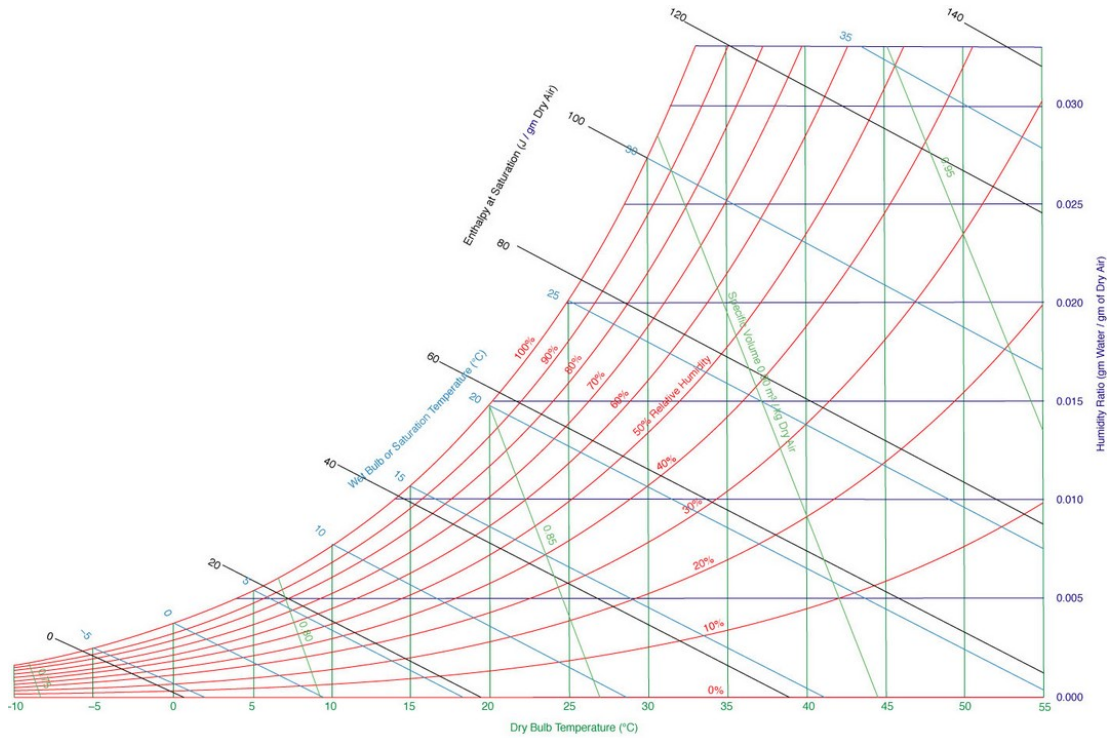


Figure 38 – Carrier Psychrometric Diagram

For an assigned level of H, represented by an horizontal line on the diagram, when the temperature decrease below the value corresponding to the Temperature where intersection with saturation curve takes place (Dew Point), the water contained in the mixture can't remain entirely in the vapor state, and therefore at the

---

equilibrium conditions the thermodynamic system will be constituted by a mixture of saturated vapor and condensed liquid, which is the condition to avoid for the above discussed reasons.

### 5.3. HUMIDITY SENSORS BASED ON OPTICAL FIBER TECHNOLOGY

At present, traditional commercial electronic sensors based on capacitive sensing element in thermoset polymer are employed in CMS for Relative Humidity monitoring. The main drawback in their these lies in their poor radiation hardness capability. They present indeed a very short operative lifetime in the harsh environment of the inner layers of the CMS Tracker System, thereafter they must be substituted due to the irreversible damage caused by radiations in those regions of the detector. Moreover they need power supply and 3 wires for each sensing point, involving the needing of a large number of cables. During RUN1 (2010-2012) CMS Tracker was running at 5C, given the very low accumulated radiation level. For following RUN periods the operation at negative T becomes mandatory in order to secure the expected lifetime of Tracker with respect to the expected accumulated radiation level. For this reason in CMS the development of sensors for hygrometric monitoring which could overcome these issues was a fundamental request to be solved before the start up of RUN2 period (2015-2018).

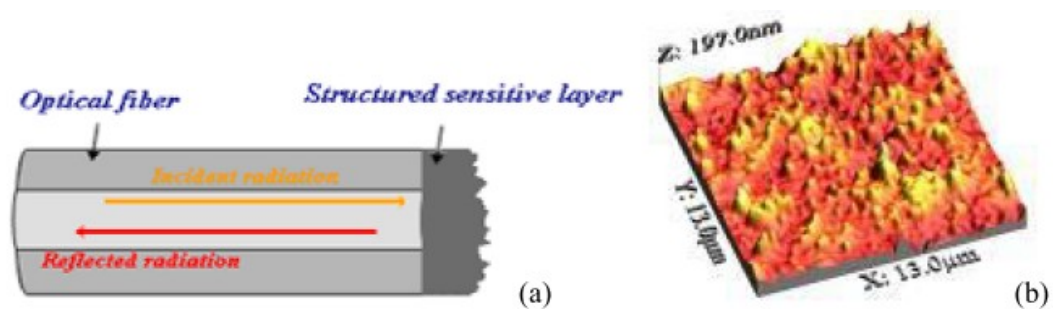


Figure 39 – RH optical sensor based on employment of a layer SnO<sub>2</sub> changing its refractive index by absorption of water molecules

Fiber Optical Sensor technology was one of the most interesting candidate solutions mainly for the offered advantages, including specifically: water and corrosion resistance, easy multiplexing with drastic reduction

---

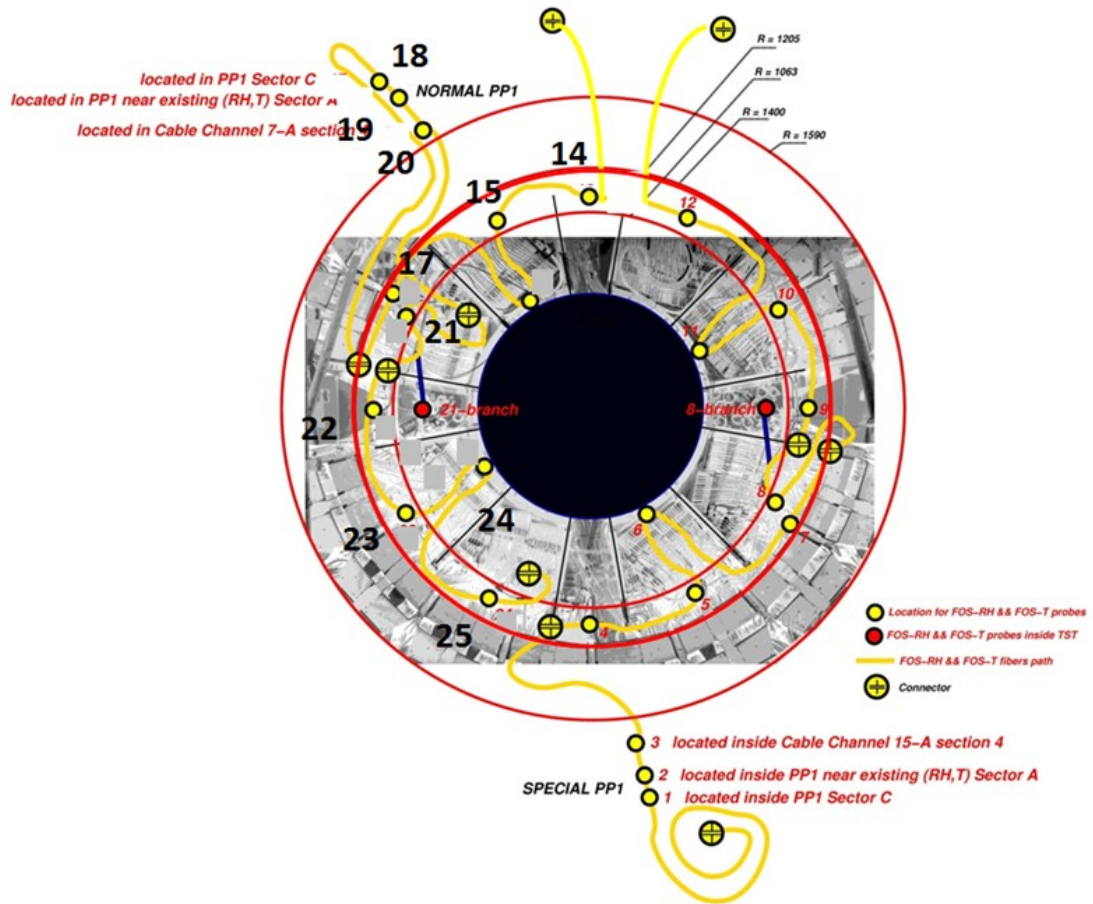
of cabling complexity, immunity toward the strong magnetic field (4 Tesla) allowing to avoid difficult recalibrations once the detector is installed and inaccessible, intrinsic safety due the passive operation, over than compactness, low weight, and reduced need of services, fundamental aspects for installation in the almost completely filled space of the Tracker System volume.

For this purpose, the possibility to apply this kind of technology for hygrometric monitoring in High Energy Physics experiments at CERN was investigated by G.Breglio et al [6]. where a first kind of working principle taken in consideration to manufacture such type of sensors was based on same results obtained by T.L,Yeo [27],[28] which demonstrate the very good SnO<sub>2</sub> sensitivity for chemical detection through fiber optical technology, since its surfaces present microstructures with dimensions comparable to those of light wavelength. By depositing a tin oxide overlay on one termination of a cleaved optical fiber, see Figure 39, any change of the refractive index of the SnO<sub>2</sub> layer due to absorption of water molecules result in a change of reflectance easily detectable by an optical interrogator. As also evidenced in [6], a perfect agreement with traditional electronic commercial RH sensors (Honeywell HIH 4000 series) can be achievable through this principle in order to get a measure of the Relative Humidity, even at low temperature close to 0°C.

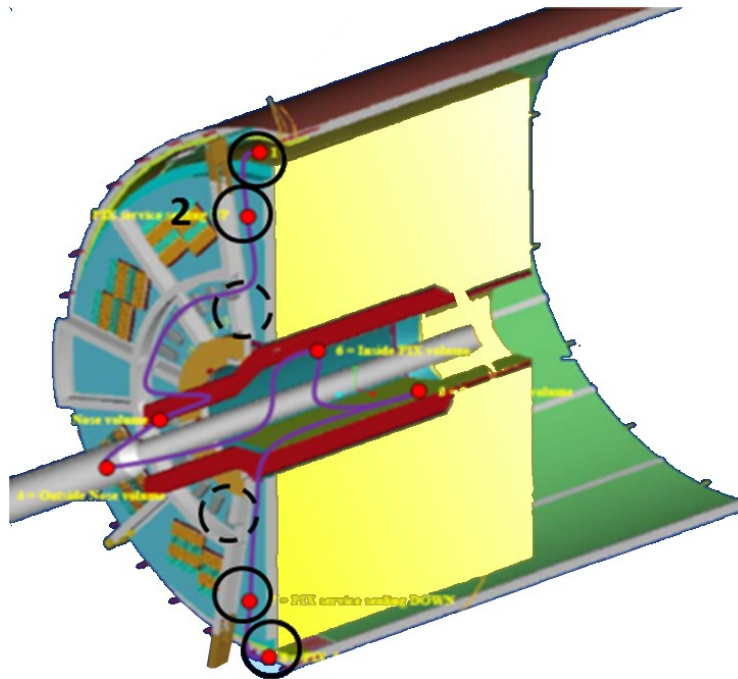
#### **5.4. RELATIVE HUMIDITY SENSORS BASED ON POLYIMIDE COATED FBG**

Sensor configuration described in previous paragraph 5.3 doesn't allow to take advantage from the multiplexing possibility offered by the fiber optical technology, since in that case it's possible to achieve only a single sensor for each optical fiber, while in CMS Tracker System a granular and distributed monitoring of the relative humidity level is needed. In order to overcome this drawback, a different kind of approach in design of fiber optical humidity can be followed. In particular as showed by TL Yeo in [27],[29] and Kronenberg [32], Relative Humidity measures can be realized by recoating FBG with opportune hygroscopic materials swelling due to the absorption of water molecules from the external environment. Polyimide (PI) is among the most used hygroscopic material for sensing application.

---



a)



b)

Figure 40 –Fiber Array path where the RH Sensors have been installed  
a) Bulkhead inside b) Pixel Volume of the CMS Tracker System

Even if the swelling of PI is lower than other polymers, it exhibits a linear and also reversible volume expansion due to water molecules absorption, as explained in [27]-[29], and for that reason it's widely used also in the transducer of traditional RH electrical sensors. Basing on this principle, our research group demonstrated the applicability of this technology (polyimide recoated FBG) also for High Energy Physics application at CERN, in presence of high levels of radiations (G.Berruti et al. [30]). For this purpose 80 hygrometers based on this technology were manufactured in Optosmart firm, calibrated at CERN and installed in CMS in the tracker and pixel volume, as described in Figure 40. Indeed, as explained in [33], modern fiber fabrication technologies allow manufacturing fibers with a very good radiation hardness capability. As described in next paragraphs, these sensor based on PI coated FBGs have been tested up to a cumulative dose at least of 200 kGy, achieving a percent resolution in the temperature range  $-15^{\circ}$  to  $20^{\circ}$  C.

### 5.5. BRAGG WAVELENGTH SHIFT DUE TO RELATIVE HUMIDITY CHANGES

Bare silica fibers are insensitive to relative humidity, which justify the assumption made in the development of the mechanical model of the coated FBG, Eq. 285 in the Chapter 3. From the Eq. 120, the Bragg wavelength shift of the single-mode optical fiber, can be expressed as:

$$\frac{d\lambda}{\lambda} = \xi dT + (1 - p_e)d\varepsilon_f \quad \text{Eq. 358}$$

where  $p_e$  is the photo-elastic constant of the fiber,  $\varepsilon_f$  is the fiber strain and  $\xi$  is the thermo-optic coefficient.

By employing the developed mechanical model presented in the Chapter 3, and solving the Eq. 316 using the mechanical and geometrical parameters of the Coated FBGs, (see Table 5), a result similar to the one achieved for the Cryogenic sensors illustrated in the Chapter 4 has been obtained. Indeed the  $\varepsilon_f(r, z)$  and  $\varepsilon_c(r, z)$  resulted again only weakly dependent by  $r$  and  $z$ , so that they can be assumed almost uniform in both the glass fiber and coating zone.

---

<i>Parameter</i>	<i>Symbol</i>	<i>Value</i>
<i>Fiber Radius (cladding included)</i>	$r_{ci}$	62.5 $\mu\text{m}$
<i>Polyimide Thickness</i>	$r_{ce}$	10 $\mu\text{m}$ , 22.5 $\mu\text{m}$
<i>Glass Fiber Elastic modules</i>	$E_c$	70 GPa
<i>Polyimide Elastic modules</i>	$E_f$	6 GPa
<i>Glass Fiber Poisson Coefficient</i>	$\nu_f$	0.3
<i>Polyimide Poisson Coefficient</i>	$\nu_c$	0.3
<i>Glass Fiber Thermal Expansion Coefficient</i>	$\alpha_f$	2.6 $\mu\epsilon/\text{K}$
<i>Polyimide Thermal Expansion Coefficient</i>	$\alpha_c$	60 $\mu\epsilon/\text{K}$
<i>Polyimide Swelling Coefficient</i>	$\beta_c$	18 $\mu\epsilon/\%RH$

Table 5- Coated FBG material and geometric parameters of the developed RH FBGs

Thus, since at the interface they must also be the same, with very good approximation we can write:

$$\epsilon_f^{tot} \cong \epsilon_c^{tot} \equiv \epsilon \quad \forall r, z \tag{Eq. 359}$$

And therefore:

$$\epsilon_f^{th} + \epsilon_f^{el} \cong \epsilon_c^{el} + \epsilon_c^{th} + \epsilon_c^{sw} = \epsilon \tag{Eq. 360}$$

i.e. the total strain in the fiber zone is equal to the total strain in the coating zone. Of course, using the relation Eq. 360,  $d\lambda/\lambda$  expressed by the Eq. 120 becomes:

$$\frac{d\lambda}{\lambda} = \xi dT + (1 - p_e) d\epsilon \tag{Eq. 361}$$

Where  $\epsilon$  is the common total strain of fiber and coating. Assuming null the mixed derivatives:

$$\frac{\partial \xi}{\partial \epsilon} = \frac{\partial p_e}{\partial T} = 0 \tag{Eq. 362}$$

The relation Eq. 361 represents an exact differential which can be easily integrated separately for the two variables  $T$  and  $\epsilon$ :

$$\int_{\lambda_0}^{\lambda} \frac{d\lambda}{\lambda} = \int_{T_0}^T \xi dT + \int_0^{\varepsilon} (1 - p_e) d\varepsilon \quad \text{Eq. 363}$$

Which gives:

$$\ln\left(\frac{\lambda}{\lambda_0}\right) = \xi(T - T_0) + (1 - p_e)\varepsilon \quad \text{Eq. 364}$$

Or equivalently:

$$\lambda = \lambda_0(T_0, RH_0) e^{\xi(T - T_0) + (1 - p_e)\varepsilon} \quad \text{Eq. 365}$$

Taking into account that the total strain  $\varepsilon$  must be the same, Eq. 359, from the Eq. 360 we obtain:

$$\varepsilon_f^{el} = \varepsilon - \varepsilon_f^{th} \quad \text{Eq. 366}$$

$$\varepsilon_c^{el} = \varepsilon - \varepsilon_c^{th} - \varepsilon_c^{sw} \quad \text{Eq. 367}$$

Applying a procedure similar to the one discussed in the Chapter 4 relatively to the Cryogenic sensors, it's possible to calculate the common strain by equilibrium considerations starting from the thermo mechanical properties of fiber and coating, with the only difference consisting in the fact that in the RH case the swelling strain of the coating must be also be taken into account (see Eq. 367). Therefore in this case the Eq. 329 must be now modified as it follows:

$$\pi(r_{ce}^2 - r_{ci}^2)E_c(\varepsilon - \varepsilon_c^{th} - \varepsilon_c^{sw}) + \pi r_{ci}^2 E_f(\varepsilon - \varepsilon_f^{th}) = 0 \quad \text{Eq. 368}$$

Solving the Eq. 368 with respect to  $\varepsilon$ , we obtain:

$$\varepsilon = \frac{H_f \varepsilon_f^{th} + H_c(\varepsilon_c^{th} + \varepsilon_c^{sw})}{H_f + H_c} \quad \text{Eq. 369}$$

where the longitudinal stiffness, respectively of the active coating,  $H_c$  and the glass fiber,  $H_f$  as:

$$H_c = \pi(r_c^2 - r_f^2)E_c \quad \text{Eq. 370}$$

$$H_f = \pi r_f^2 E_f \quad \text{Eq. 371}$$

In the hypothesis of linearity for the thermal and swelling strains, we get:

$$\varepsilon = \frac{H_f \alpha_f (T - T_0) + H_c \alpha_c (T - T_0) + H_c \beta_c (RH - RH_0)}{H_f + H_c} \quad \text{Eq. 372}$$

Finally, by substituting in the Eq. 365, we obtain:

$$\lambda = \lambda_0(T_0, RH_0) e^{\xi(T-T_0) + (1-p_e) \frac{H_f \alpha_f (T-T_0) + H_c \alpha_c (T-T_0) + H_c \beta_c (RH-RH_0)}{H_f + H_c}} \quad \text{Eq. 373}$$

Or, replacing the expression of  $H_f, H_c$ :

$$\lambda = \lambda_0 e^{\xi(T-T_0) + (1-p_e) \frac{(r_{ci}^2 E_f \alpha_f (T-T_0) + (r_{ce}^2 - r_{ci}^2) E_c [\alpha_c (T-T_0) + \beta_c (RH-RH_0)])}{[r_{ci}^2 E_f + (r_{ce}^2 - r_{ci}^2) E_c]}} \quad \text{Eq. 374}$$

### 5.5.1. SENSOR SENSITIVITIES

If the variations of T and RH are in the range of linear response of the FBG, the expression of the wavelength shift, Eq. 374, can be approximated by linearization. From the Eq. 361 we get:

$$\Delta\lambda = \lambda_0 \xi (T - T_0) + \lambda_0 (1 - p_e) \varepsilon \quad \text{Eq. 375}$$

$$\Delta\lambda = \lambda_0 \xi \Delta T + \lambda_0 (1 - p_e) \frac{(H_f \alpha_f + H_c \alpha_c) \Delta T + H_c \beta_c \Delta RH}{H_f + H_c} \quad \text{Eq. 376}$$

$$\Delta\lambda = \left[ \lambda_0 \xi + \lambda_0 (1 - p_e) \frac{H_f \alpha_f + H_c \alpha_c}{H_f + H_c} \right] \Delta T + \left[ \lambda_0 (1 - p_e) \frac{H_c \beta_c}{H_f + H_c} \right] \Delta RH \quad \text{Eq. 377}$$


---

By defining, in the previous expression, the sensitivities:

$$S_T = \lambda_0 \left[ \xi + (1 - p_e) \frac{H_f \alpha_f + H_c \alpha_c}{H_f + H_c} \right] \quad \text{Eq. 378}$$

$$S_{RH} = \lambda_0 \left[ (1 - p_e) \frac{H_c \beta_c}{H_f + H_c} \right] \quad \text{Eq. 379}$$

The shift can be expressed as:

$$\Delta\lambda = S_T \Delta T + S_{RH} \Delta RH \quad \text{Eq. 380}$$

Substituting the Eq. 374 in the Eq. 378 and Eq. 379, it results that the sensitivities  $S_T, S_{RH}$  are given by:

$$S_T = \lambda_0(T_0, RH_0) \left[ \xi + (1 - p_e) \frac{r_{ci}^2 E_f \alpha_f + (r_{ce}^2 - r_{ci}^2) E_c \alpha_c(RH)}{r_{ci}^2 E_f + (r_{ce}^2 - r_{ci}^2) E_c} \right] \quad \text{Eq. 381}$$

$$S_{RH} = \lambda_0(T_0, RH_0) \left[ (1 - p_e) \frac{(r_{ce}^2 - r_{ci}^2) E_c \beta_c(T)}{r_{ci}^2 E_f + (r_{ce}^2 - r_{ci}^2) E_c} \right] \quad \text{Eq. 382}$$

The dependence  $\alpha_c(RH)$  and  $\beta_c(T)$  is confirmed by the data obtained in [30], where  $S_T$  resulted a decreasing function of RH while  $S_{RH}$  resulted to be slightly dependent by temperature.

According for example to Rajinikumar et al. [19], the photo elastic constant in the Eq. 374 can be assumed as:

$$p_e = -\frac{\partial n}{n \partial \varepsilon} \approx 0.23 \quad \text{Eq. 383}$$

While for the thermo optic coefficient  $\xi$  of silica appearing in the same equation Eq. 374, again according to [19], the following value can be employed:

$$\xi = \frac{\partial n}{n \partial T} \approx 8 \text{ ppm/K} \quad \text{Eq. 384}$$

The Eq. 380, shows clearly that the Bragg reflected wavelength depends by both the temperature and the Relative Humidity. For this reason, in order to get the RH from the reflected Bragg readout, a further sensor measuring the temperature in the same point where the RH is placed is needed for compensation.

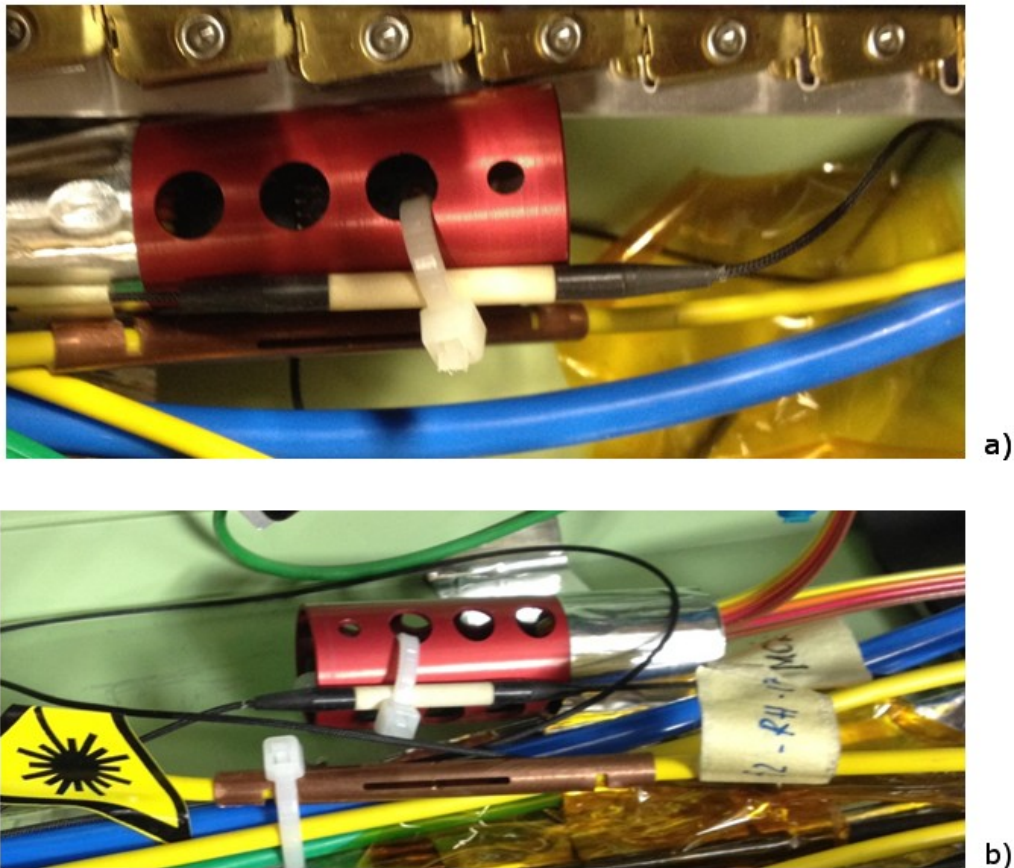


*Figure 41 -a) b) RH FBG sensor (in the copper package) and Temperature FBG sensor (in white ceramic package) for T for T compensation*

For the above reason, in the FBG hygrometer installation campaign in CMS in November 2013, two independent optical fiber arrays of sensors were employed, one for the temperature measure by standard commercial FBG, and a second one with the PI active coated FBG array sensitive to the relative humidity by swelling. The PI active coated FBGs were placed inside a copper package with a split allowing air inside to get same RH of the external environment, as shown in Figure 41 b).

---

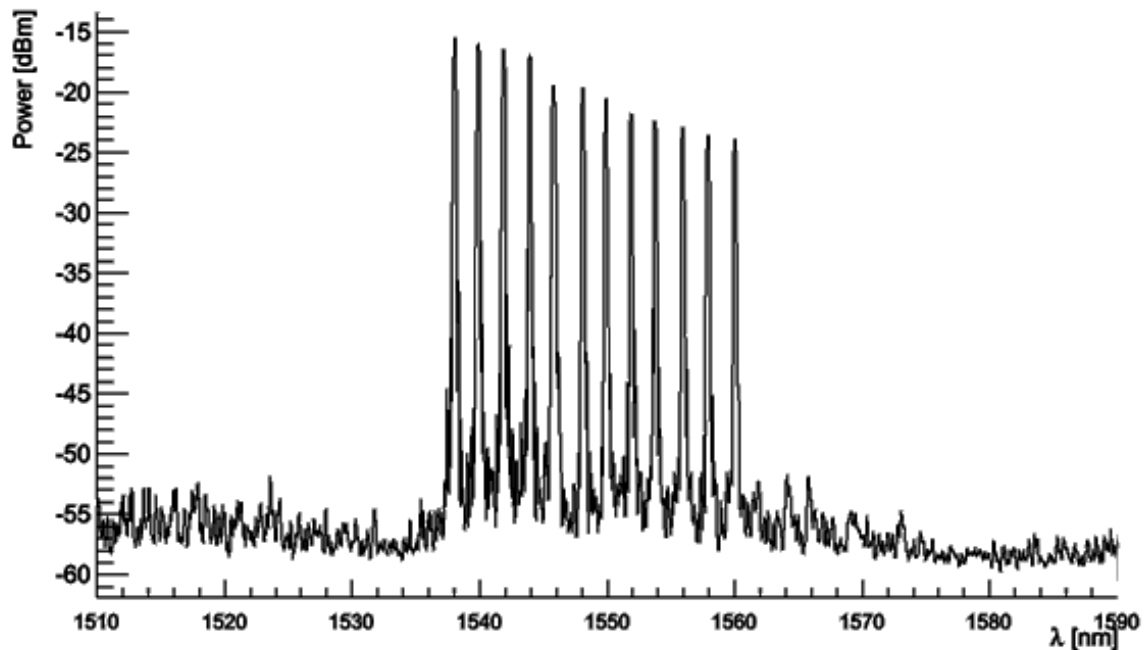


Figure 42 – Typical back reflected signal in the reference conditions of a FBG array. The points in correspondence of the peaks, are relative to the different Bragg wavelength of each FBG in the array

By linking in series several FBGs with different reference wavelength on a single optical fiber to create an array, the typical back reflected signal obtained by interrogator readout is reported in the Figure 42, where the multiple main peaks in correspondence to each FBG are clearly visible.

## 5.6. MASS TRANSPORT PHENOMENA

As predicted by the Eq. 374, increasing the coating thickness, a greater sensitivity is expected, as also shown by T.L. Yeo [27]: in the Figure 43 the Bragg Wavelength shift as function of the Relative Humidity he obtained for different coating thickness are reported. The main drawback in the use of a coating too thick resides in the slower response of the sensor with respect to changes of relative humidity, due the grater diffusion time of water molecules inside the sensitive overlay, as also reported in other literature studies publications [27][28].

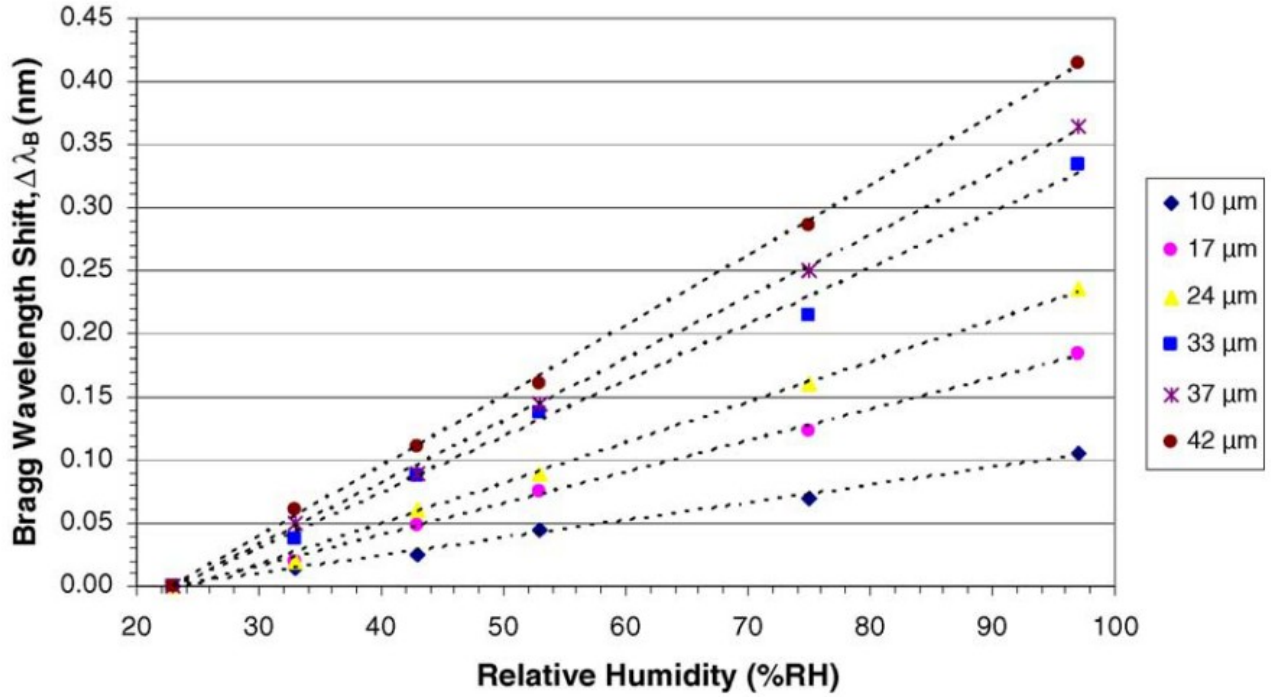


Figure 43 –Bragg Wavelength shift for different coating thickness as function of the Relative Humidity [27]

The dynamic of diffusion can be determined by solving the Fick diffusion equation in the in the solid phase (polyimide, PI). In cylindrical coordinates we have:

$$\frac{\partial C_{H_2O}^{PI}}{\partial t} = \frac{1}{r} \frac{\partial}{\partial r} \left( r D_{H_2O}^{PI} \frac{\partial C_{H_2O}^{PI}}{\partial r} \right) \quad \text{Eq. 385}$$

Where  $C_{H_2O}^{PI}$  is the concentration of water molecules in the PI while  $D_{H_2O}^{PI}$  is the diffusivity of water molecules in PI. The boundary conditions are given by assigning the flux on the inner and outer radius of the coating:

$$J_{H_2O}(r_{ic}) = \left( D_{H_2O}^{PI} \frac{\partial C_{H_2O}^{PI}}{\partial r} \right)_{r=r_{ic}} = 0 \quad \text{Eq. 386}$$

$$J_{H_2O}(r_{ec}) = \left( D_{H_2O}^{PI} \frac{\partial C_{H_2O}^{PI}}{\partial r} \right)_{r=r_{ce}} = K(C_{H_2O}^{Air} - C_{H_2O}^{PI}) \quad \text{Eq. 387}$$

Where  $K$  is the global transfer coefficient vapor-solid and  $C_{H_2O}^{Air}$  is the concentration of water molecules in the external environment.  $C_{H_2O}^{Air}$  can be assumed as the absolute humidity in the air, Eq. 356:

$$C_{H_2O}^{Air} = H = \frac{m_v}{m_a + m_v} \quad \text{Eq. 388}$$

Through the Eq. 385, starting from the Bragg Shift readout, it's therefore possible to get the humidity  $H$  in the air environment, and consequently also the relative humidity  $RH$ , to be calculated knowing the air temperature and the pressure, using the known psychrometric data for the air, Figure 38:

$$RH = RH(C_{H_2O}^{Air}, T, p) \quad \text{Eq. 389}$$

In this way it could be possible to calculate in real time the Relative Humidity taking also into account the transitory temporal stages due to the diffusive mass transport phenomena. This could allow, for example, to employ larger thickness for the FBG Coating in order to increase the sensitivity and the resolution of the sensor, for future applications.

However it is worth to evidence that, at present, without taking into the transitory stages, since the minimum shift in the Bragg wavelength which can be detected is 1pm, 10  $\mu\text{m}$  thickness for the coating assure anyway a relative humidity resolutions of about 1% RH, as evidenced in [30].

## 5.7. RADIATION HARDNESS CAPABILITY OF THE PI COATED FBG RH SENSORS

In the work of G.Berruti et al. [30], the prototyped RH FBG sensors demonstrated a very good radiation hardness after a deep experimental campaign carried out in the laboratories of CERN. In fact, as clearly evidenced [30], after a cumulated irradiation dose of 10 kGy, the FBGs were perfectly working while, conversely, the traditional electronic based RH sensors resulted definitively damaged, presenting, as expected, very low resistance to the irradiation. Moreover, after the irradiation, the presence of a small change of the Bragg reference wavelength due to the irradiation was observed. The observed wavelength

---

shift resulted of 20 pm and 16 pm (picometers), respectively for a coating thickness of 22.5  $\mu\text{m}$  and 9  $\mu\text{m}$ , comporting therefore a mean radiation sensitivity of 2pm/kGy and 1.6pm/kGy. These values agree perfectly, being also slightly higher, with FBG sensitivities to radiation dose, up to 160 pm for the Bragg Wavelength Shift after 100 kGy, observed by previous published studies, as for example discussed in [62].

Our research group decided therefore to carry out further irradiation tests by using a  $\text{Co}^{60}$  radioactive source, in order to investigate the influence of higher levels of irradiations on the sensors (see A. Makovec et al. [31]). Multiple campaigns were performed on both the uncovered Temperature FBG sensors and the PI coated FBG, providing a total adsorbed dose varying from of 10 to 210 kGy. The tests were conducted in the PH-DT test facility at CERN.

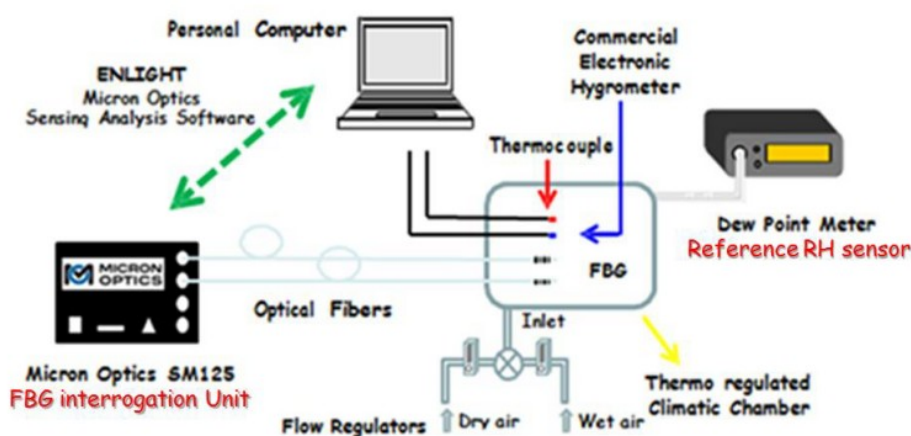


Figure 44 – Experimental Set-Up

For this purpose, a climatic chamber was provided with a thermo-regulation circuit for temperature monitoring, while a precise control of the relative humidity was ensured by using a valve system. The tests covered the range of RH from 0% to 90% and the temperature range from  $-20^{\circ}\text{C}$  to  $+30^{\circ}\text{C}$ . A schematic illustration of the set-up is shown in the Figure 44. The FBG FOS Sensors were installed in the chamber and interrogated by a state-of-the-art Optical Interrogator (Micron Optic sm125) with 1 pm wavelength resolution. As a reference sensor, a high performance Chilled Mirror Dew Point Hygrometer was used for

measuring the RH. As reference temperature sensors, calibrated resistance thermometers (PT-100) were placed close to the FBGs.

These tests confirmed the excellent radiation hardness capability of the FBGs. The tests also confirmed the small wavelength shift due to irradiation, even if the effect tends toward saturation for higher level of absorbed dose. Details of the results of tests performed are reported in the following sections.

### **5.7.1. IRRADIATION TESTS ON THE TEMPERATURE FBG SENSORS**

Six irradiation campaigns were performed on the uncovered commercial Temperature FBGs, providing a total adsorbed dose of 10, 20, 50, 90, 150 and 210 kGy in each intermediate step. This experimental campaign evidenced a low radiation-induced wavelength shift. Moreover, the shift derivative resulted decreasing with respect the absorbed dose. In particular, after an adsorbed dose of 150 kGy, it was lower than 0.15 pm/kGy. Conversely the sensors sensitivities resulted substantially unchanged after all the performed campaigns, as the Figure 45 shows. Furthermore, considering that the estimated absorbed dose of most of the sensors to be placed in the CMS Tracker is about 12 kGy during the RUN2 period, the corresponding wavelength shift due to irradiation is 1.8 pm, comporting an induced error in terms of temperature of about 0.18 °C. This suggested to perform a pre-irradiation step of the sensors at a dose higher than 150 kGy in order to bring them in the low  $\gamma$ -radiation sensitivity zone for their employment in the CMS experiment.

---

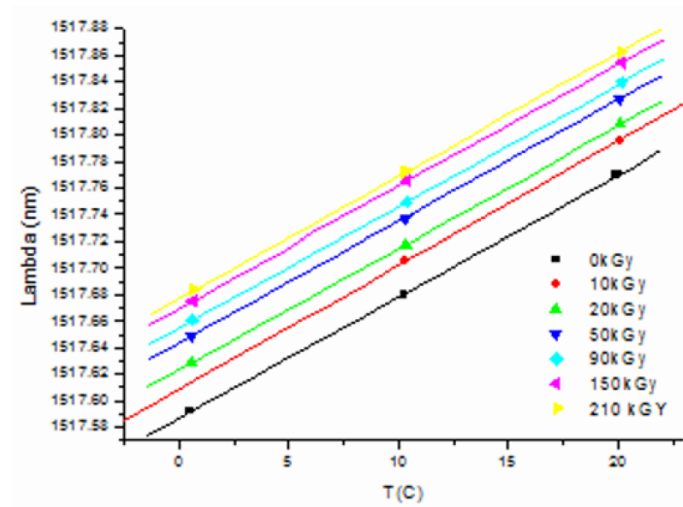


Figure 45 – Commercial Temperature FBG response after the irradiations campaigns

### 5.7.2. IRRADIATION TESTS ON THE PI COATED RH FBG SENSORS

Three irradiation campaigns were performed on the PI Coated RH FBG Sensors, providing a total adsorbed dose respectively of 10, 50 and 90 kGy in each intermediate step. The mean Relative Humidity Sensitivity  $S_{RH}$  was found to be 1.42 pm/%RH. The sensors were characterized at CERN after each campaign, performing RH tests at constant T changing the relative humidity in the range [0 – 50] %. The obtained results are reported in the Figure 46. The figure shows that the  $S_T$  and  $S_{RH}$  sensitivities variations are inside the measurement error and for this reason they can be considered negligible. Moreover, similarly to the T-Sensors, the RH-Sensors also show radiation induced wavelength shift. Also in this case, the tests carried out suggest that a pre-irradiation step helps decreasing the sensitivity for higher level of radiation.

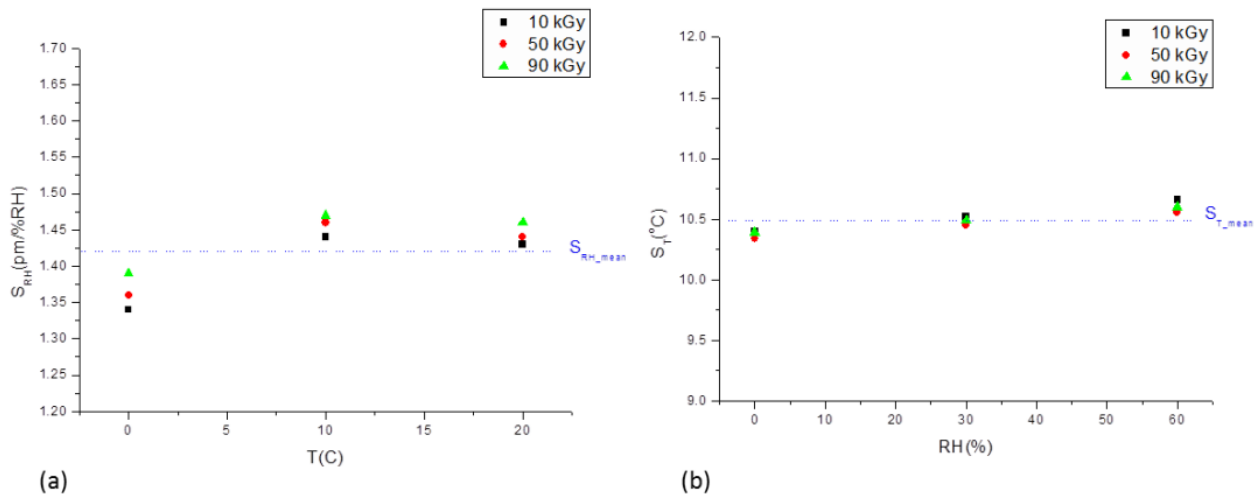


Figure 46 – Sensitivities of the PI Coated RH FBG sensor after the irradiation campaigns

## 5.8. PRELIMINARY STUDY ON EPOXY COATED RELATIVE HUMIDITY FBG SENSORS

It's well known that humidity affects the properties of epoxy resins. Even though considerable research has focused on the humidity effects on the water diffusion mode in epoxy resin, mechanisms are still not fully understood in this domain. This is mainly due to the complexity of the hygrothermal effects in epoxy. Two approaches have emerged that generally characterize the nature of water in epoxy. One is the free volume approach which presumes that water diffuses into epoxy resin and resides in the free volume of the material. The other approach is the interaction concept that suggests water molecules couple strongly with certain hydrophilic functional groups such as hydroxyl or amine in epoxy resin [34]-[47].

### 5.8.1. HYGROTHERMAL PROPERTIES OF EPOXY

Zhou and al. [48] assessed the nature of absorbed water and the related hygrothermal effects in epoxy resins. Morel et al. [49] studied the equilibrium water absorption for 23 epoxide-amine networks of various structure including di, tri, and tetra functional epoxides, and diamines, which were mainly of the dianiline type (more or less sterically hindered in some cases). The comparative study of these systems shows clearly

that the main hydrophilic loci are in the vicinity of tertiary amines, and that these latter groups play a concerted role with hydroxyl groups, in water bonding. Zheng et al. [50] studied the system of DGEBA cured with an amine-terminated poly propylene oxide, in particular they showed results from a study of a glassy epoxy subjected to isothermal RH-jumps. They obtained the volume recovery responses in different histories as intrinsic isopiestic (constant RH), memory effect, and the asymmetry of approach. Our results qualitatively support the hypothesis that water has an effect similar to that of temperature on the structure (volume, enthalpy) of the glass-forming material. Most important, Authors reported a swelling coefficient for their epoxy of the order of 200 ppm/%RH that happens to be the double of a typical polyimide [27].

Starting from these literature studies on the matter, our research group investigated the hygrothermal properties of three epoxy systems: DiGlycidyl ether of Bisphenol-A (DGEBA) with metaphenylene diamine (mPDA), TGDDM 4,40-diaminodiphenyl sulfone (DDS), and Fiberite 934 epoxy resin. Water sorption was achieved by immersing the materials in distilled water at constant temperature of 45, 60, 75 and 90 °C for 1530 h. Water absorption and desorption profiles were analyzed to determine the diffusion parameters. These tests, performed at the laboratories of the Institute for Composite and Biomedical Materials of the National Research Council (CNR-IMCB, Italy), showed that the system with DGEBA-mPDA, presented the highest diffusivity. For this reason, further tests on FBG manufactured by recoating with DGEBA-mPDA epoxy resin were performed. Details on both the Coating method and the obtained sensitivities of the manufactured FBGs are discussed in the following sections.

### **5.8.2. COATING METHOD**

Mainly based on the work of Zhou [15] that indicates the diamine as the curing agent producing the highest water swelling material, a commercial system composed by the DGEBA (Elantas Camattini, EC 170) with a diamine (Elantas Camattini, IG 824 K24) was chosen to prepare the humidity sensor in the CNR – IMCB laboratories. The procedure to manufacture the thermo hygrometer was based on the dip coating technique. (Figure 47 shows a Dip Coater). The fiber containing the FBG was cleaved at one end to facilitate the use of

---

the dip coating and then was mounted onto the dip coater arm. The resin DGEBA was extracted from the vessel and put into a beaker. The diamine in the ratio of 1:4 in weight was added to the beaker. After manual stirring, the beaker has put in a vacuum planetary mixer (Thinky). The beaker has been immediately put on the dip coater plate.



*Figure 47 –Dip Coater*

The fiber containing the grating was dipped into the solution. After the resin was coated onto the grating, the sensor was dried in the oven at 120°C for 5min. Variable thickness coating was obtained by repeating the dipping and dry procedure. A postcuring at 120° C completed the process. The coating thickness, measured through optically micrography, resulted 2.5  $\mu\text{m}$ .

### **5.8.3. EPOXY COATED FBG SENSITIVITY**

In order to assess the relative humidity sensitivity, a specific test on one Epoxy Coated FBG prototype was then performed in CNR - IMCB laboratories in Portici, Italy. The apparatus consisted of a bubbler where a

---

controlled dry air flux circulated at different flow velocity to obtain variable relative humidity at room temperature. Reference thermo hygrometer (Vaisala mod.HMP233) was employed in the testing chamber.

The performed test confirmed the possibility of using epoxy matrix cured by diamine hardener as swelling coating for FBG based thermo hygrometer. At room temperature, indeed, the test evidenced a relative humidity FBG sensitivity of 0.27 pm/%RH for the manufactured prototype having 2.5  $\mu\text{m}$  epoxy/diamine coating thickness. This sensitivity value agrees perfectly with the literature data indicating a swelling coefficient for epoxy/diamine materials double than that of polyimide. Therefore the test suggested the efficiency of the proposed material to be employed as alternative Active Coating of FBG thermo hygrometer, for next generation production, presenting a double swelling coefficient with respect to that of PI Coated FBG. In this way, it's possible to obtain a better RH resolution without increasing the coating thickness, which, as evidenced, comports a slower response of the FBG.

## 5.9. CONCLUSIONS

In conclusions RH FBG based optical sensor represent an excellent solution to overcome all the serious drawback that traditional electronic sensor present for application in the High Energy Physics, in hostile environment for the presence of high levels of radiations, presenting nevertheless a very good agreement with RH measurements provided by commercial electrical hygrometers. Irradiations tests up to 200kGy have demonstrated their excellent radiation hardness capability. Moreover, as also demonstrated, such kind of PI coated-FBG RH sensors have the capability to work also at negative temperatures requested for the safe operation of the CMS Tracker, from  $-15^{\circ}\text{C}$  to  $20^{\circ}\text{C}$ , showing a linearity in the response in this temperature range. For future applications, in order to increase the Coated FBG resolution by employing a thicker coating, a numerical procedure has been proposed to evaluate in real time the transitory stage due to the water molecules diffusion phenomena inside the Coating. Alternatively, for the same purpose, different materials with an higher swelling coefficient should be employed. For this reason, preliminary tests on an Epoxy Coated FBG have been performed, in order to evaluate the possible development, in a later stage, of

---

the Epoxy based FBG RH sensor for High Physics applications. The results obtained through the preliminary test on a prototyped Epoxy Coated FBG RH sensor evidenced a double sensitivity with respect to the PI Coated FBG.

---

## CONCLUSIONS

High Energy Physics Experiment equipments at the laboratories of the European Organization for Nuclear Research (CERN) in Geneva need an efficient monitoring system to secure operations and to prevent damages. In particular it's fundamental a granular control of several parameters such as temperature, stress/strain due the intense magnetic field, humidity and so on. Traditional sensing system based on electrical sensors present serious drawbacks in such kind of environmental conditions, in particular for the high levels of noise generated by the very intense electromagnetic fields and for the concomitant presence of very high level of irradiations, causing often non reversible failures. FBG optical sensors offer an excellent solution to these issues presenting indeed immunity toward electromagnetic fields, radiations hardness capability, compactness, intrinsic multiplexing, reduction of instrumentation and improvement of the workplace safety. This technology is expanding year by year its field of applications. In the present thesis, in the suitability of new Active Coated FBG sensors for Cryogenic Temperature measures in the LHC and Active Coated FBG sensors for Relative Humidity measures in the CMS experiment are discussed and demonstrated. The mechanical behavior the Active Coated FBGs has been analyzed by developing a mathematical model to correlate the FBG wavelength shift with the external forcing factors causing non-elastic strain inside the coating zone. This model has been used as baseline for sensor manufacturing both in Optosmart firm and in CNR - IMCB laboratories in Portici, Italy. Measurement results from manufactured sensors perfectly agree with the predicted behavior from mathematical model. Moreover a Correlated Fluctuation Analysis has been proposed to overcome the drawbacks in employment of the direct derivative method to evaluate the thermal expansion coefficient, in the Deybe temperature range (4-10 K), of the polymers used for the coating of the prototyped FBG sensors for Cryogenic measures. Indeed, the new Cryogenic FBGs prototyped have been manufactured by recoating the grating with two polymeric materials, PMMA and EPOXY. Both have demonstrated stable behavior in the wide temperature range from 4K to 300K. The sensitivity they have showed allows their employment for Cryogenic temperature measures in the

---

temperature range from 30K up to room temperature, therefore they are suitable for the LHC Cryo Power Lines temperature operative conditions. At lower T range (4-30K) their sensitivity is significantly reduced.

On the other hand, RH FBG based optical sensor represent an excellent solution to overcome all the serious drawback that traditional electronic sensor present for application in the High Energy Physics, in hostile environment for the presence of high levels of radiations, causing non reversible failures to the traditional electronic based RH sensors. Polyimide (PI) coated-FBG RH sensors demonstrated the capability to work also at the negative temperatures demanded for the safe operation of the CMS Tracker, from  $-15^{\circ}\text{C}$  to  $20^{\circ}\text{C}$ . In order to increase the sensitivity for future applications, further studies on alternative materials with an higher swelling coefficient (EPOXY) have been be tested as FBG coating. The obtained results on a prototype Epoxy Coated FBG RH sensor evidenced a double sensitivity with respect to the PI Coated FBG. Their manufacturing at present its possible with dip coating technique.

In conclusion, Fiber Optical Sensors project in CMS started in 2009 and at present several hundred of FBG sensors are running in different locations of the detector without any problem 24/24h in a very hostile environment, demonstrating an impressive stable and reliable behavior. Optical Fiber Sensor Technology is becoming a new reference standard for High Energy Physics applications. Moreover it represents a great example of interdisciplinary collaboration between academic and industrial partners.

---



**BIBLIOGRAPHY**

- [1] Marco Esposito, Salvatore Buontempo, Angelo Petriccione, Mauro Zarrelli, Giovanni Breglio, Andrea Saccomanno, Zoltan Szillasi, Alajos Makovec, Andrea Cusano, Antonella Chiuchiolo, Marta Bajko, Michele Giordano - Fiber Bragg Grating sensors to measure the coefficient of thermal expansion of polymers at cryogenic temperatures – *Sensors and Actuators A:Physical* 189 (2013) 195–203
  - [2] CERN - European Organization for Nuclear Research
  - [3] Stephen Myers – The Large Hadron Collider 2008-2013 – *International Journal of Modern Physics A* 28 (25): 1330035–1–1330035–65.
  - [4] A. O.M. Iorio – Measurement of single top t-channel production cross section through the  $t \rightarrow Wb \rightarrow \mu\nu b$  decay in 7 TeV proton-proton collisions with the Compact Muon Solenoid detector at the Large Hadron Collider – PhD Thesis
  - [5] Timoshenko and Goodier – *Theory of Elasticity* – McGraw Hill, 1951
  - [6] G. Breglio, S. Buontempo, A. Buosciolo, M. Consales, A. Cusano, A. Cutolo, M. Giordano, A. Irace, P. Petagna – FOS in CMS detector at CERN – The Compact Muon Solenoid Experiment Conference Report, CMS CR -2010/100
  - [7] LHC commissioning with beam, CERN – 2009
  - [8] LHC Machine Lyndon Evans and Philip Bryant (editors) 2008 JINST 3
-

---

S08001, doi: 10.1088/1748-0221/3/08/S08001

- [9] Compact Muon Solenoid Experiment at CERN's LHC – Official website
- [10] P.Mégret, S.Bette, C.Crunelle, C.Caucheteur – Fiber Bragg Gratings: fundamentals and applications – 2007
- [11] Richard Syms John Cozens - Optical Guided Waves And Devices - Mcgraw-Hill (1992)
- [12] X.Chu, R.Huang, H.Yang, Z.Wu, J.Lu, Y. Zhou, L. Li – The cryogenic thermal expansion and mechanical properties of plasma modified ZrW<sub>2</sub>O<sub>8</sub> reinforced epoxy - Materials Science and Engineering A 528 (2011) 3367–3374
- [13] P. Ifju, D. Myers, W. Schulz - Residual stress and thermal expansion of graphite epoxy laminates subjected to cryogenic temperatures – Composites Science and Technology 66 (2006) 2449 –2455
- [14] J.B. Schutz - Properties of composite materials for cryogenic applications -Cryogenics 38 (1998) 3-12
- [15] J. Yang, G. Yang, G. Xu, S. Fu - Cryogenic mechanical behaviors of MMT/epoxy nanocomposites - Composites Science and Technology 67 (2007) 2934–2940
- [16] R.S. Praveen, S. Jacob, C.R.L. Murthy, P. Balachandran, Y.V.K.S. Rao - Hybridization of carbon–glass epoxy composites: An approach to achieve low coefficient of thermal expansion at cryogenic temperatures - Cryogenics 51 (2011) 95–104
- [17] U.Escher - Thermal expansion of epoxy resins with different cross-link densities at low temperatures - Cryogenics 35 (1995) 775-778
- [18] G.Schwarz - Thermal expansion of polymers from 4.9. K to room temperature - Cryogenics 28
-

(1988) 248-254

- [19] R. Rajinikumar, M. Süßer, K.G. Narayankhedkar, G. Krieg , M.D. Atrey - Design parameter evaluation of a metal recoated Fiber Bragg Grating sensors for measurement of cryogenic temperature or stress in superconducting devices - *Cryogenics* 49 (2009) 202–209
- [20] T. Mizunami, H. Tatehata and H. Kawashima - High-sensitivity cryogenic fibre-Bragg-grating temperature sensors using Teflon substrates - *Meas. Sci. Technol.* 12 (2001) 914–917
- [21] S. W. James, R. P. Tatam, A. Twin, M. Morgan, and P. Noonan – Strain response of fibre Bragg grating sensors at cryogenic temperatures - *Meas. Sci. Technol.* 13 (2002) 1535–1539
- [22] T. Habisreuther, E. Hailemichael, W. Ecke, I. Latka, K. Schröder, C. Chojetzki, K. Schuster, M. Rothhardt, and R. Willsch - Ormocer Coated Fiber Optic Bragg Grating Sensors at Cryogenic Temperatures - *Ieee Sensor Journal* 12(1) (2012) 13-16
- [23] Y. Tanaka, M. Ogata, K. Nagashima, H. Agawa, S. Matsuura, Y. Kumagai - Experimental investigation of optical fiber temperature sensors at cryogenic temperature and in high magnetic fields -*Physica C* 470 (2010) 1890–1894
- [24] I. Latka, W. Ecke, B. Höfer, T. Habisreuther, R. Willsch - Fiber-optic Bragg gratings as magnetic field-insensitive strain sensors for the surveillance of cryogenic devices - *Cryogenics* 49 (2009) 490–496
- [25] T. Takeda, Y. Shindo, F. Narita - Three-dimensional thermoelastic analysis of cracked plain weave glass/epoxy composites at cryogenic temperatures – *Composites Science and Technology* 64 (2004) 2353–2362
- [26] G.Hartwing - Polymer properties at room and cryogenic temperatures - Edited by G. Hartwig,
-

Plenum Publishing Corporation, New York, 1994.

- [27] T.L. Yeo, T.Sun, K.T.V. Grattan, D. Parry, R. Lade, B. D. Powell – Characterization of a polymer-coated fibre Bragg grating sensor for relative humidity sensing – *Sensors and Actuators B Chemical* 110 (2005) 148-155
- [28] T. L. Yeo, T. Sun, K. T. V. Grattan, D. Parry, R. Lade and B. D. Powell, Polymer – Coated Fiber Bragg Grating for Relative Humidity Sensing – *IEEE Sensors Journal* 5 (2005) 1082-1089.
- [29] T. L. Yeo, T. Sun, K.T.V. Grattan - Fibre-optic sensor technologies for humidity and moisture measurement – *Sensors and Actuators A* 144 (2008) 280–295.
- [30] G. Berruti, M. Consales, M. Giordano, L. Sansone, P. Petagna, S. Buontempo, G. Breglio, A. Cusano – Radiation hard humidity sensors for high energy physics applications using polyimide-coated fiber Bragg gratings sensors – *Sensors and Actuators B: Chemical* 177 (2013) 94–102
- [31] A. Makovec, G. Berruti, M. Consales, M. Giordano, P. Petagna, S. Buontempo, G. Breglio, Z. Szillasi, N. Beni and A. Cusano – Radiation hard polyimide-coated FBG optical sensors for relative humidity monitoring in the CMS experiment – *Journal of Instrumentation*, (2013) In press
- [32] P. Kronenberg, P.K. Rastogi, P. Giaccari, H.G. Limberger, Relative humidity sensor with optical fiber Bragg grating, *Opt. Lett.* 27 (2002) 1385–1387.
- [33] F. Berghmans et al - Fiber Bragg Grating Sensors: Recent Advancements, Industrial Applications and Market Exploitation, Bentham Science Publishers, 12 (2011) 218-237
-

- [34] Loos AC, Springer GS. In: Springer GS, editor. Environmental effects on composite materials, Westport: Technomic Publishing Co, 1981, pp. 34
- [35] DeNeve D, Shanahan MER. *Polymer* 1993;34:5099
- [36] Imaz JJ, Rodriguez JL, Rubio A, Mondragon I. *J Mater Sci Lett* 1991;10:662
- [37] Biro DA, Pleizier G, Deslandes Y. *Composites Sci and Tech* 1993;46:293
- [38] Lee MC, Peppas NA. *J Applied Polymer Science* 1993;47:1349
- [39] Zhou J, Lucas JP. *Composites Sci and Tech* 1995;53:57
- [40] Adamson MJ. *J Mater Sci* 1980;15:1736
- [41] Woo M, Piggott M. *J Composite Technology Research* 1987;9:101
- [42] Gupta VB, Drzal LT. *J Applied Polymer Science* 1985;30:4467
- [43] Moy P, Karasz FE. *Polymer Engineering and Science* 1980;20: 315
- [44] Bellenger V, Verdu J. *J Mater Sci* 1989;24:63
- [45] Apicella A, Nicolais L, de Cataldis C. *J of Membrane Sci* 1985;18:211
- [46] Jelinski LW, Dumais JJ, Cholli AL, Ellis TS, Karasz FE. *Macromolecules* 1985;18:1091
- [47] Marsh LL, Lasky R, Seraphim DP, Springer GS. In: Springer GS, editor. Environmental effects on composite materials, 3. Westport: Technomic Publishing Co, 1988. pp. 51
- [48] Jiming Zhou, James P. Lucas Hygrothermal effects of epoxy resin. Part I: the nature of water in epoxy, *Polymer* 40 (1999) 5505–5512
-

- [49] E. Morel, V. Bellenger and J. Verdu, Structure-water absorption relationships for amine-cured epoxy resins, *Polymer* 1985, pp. 1719-1724
- [50] Y. Zheng and G. B. McKenna, Structural Recovery in a Model Epoxy: Comparison of Responses after temperature and Relative Humidity Jumps, *Macromolecules* 2003, 36, 2387-2396
- [51] A. Fernandez Fernandez, B. Brichard, S. O’Keeffe, C. Fitzpatrick, E. Lewis, J.-R. Vaille, L. Dusseau, D.A. Jackson, F. Ravotti, M. Glaser, H. El-Rabii - Real-time fibre optic radiation dosimeters for nuclear environment monitoring around thermonuclear reactors - *Fusion Engineering and Design* 83 (2008) 50–59
- [52] A.L. Huston, B.I. Justus, P.L. Falkenstein, R.W. Miller, H. Ning, R. Altemus – Remote optical fiber dosimetry – *Nuclear Instruments and Methods in Physics Research B* (2001)
- [53] H. Henschel, M. Körfer, K. Wittenburg, F. Wulf - Fiber Optic Radiation Sensing Systems for TESLA - TESLA Report No. 2000-26 September 2000
- [54] H. Henschel, M. Körfer, J. Kuhnenn, U. Weinand, F. Wulf - Fibre optic radiation sensor systems for particle accelerators - *Nuclear Instruments and Methods in Physics Research A* 526 (2004) 537–550
- [55] S. Girard, Y. Ouerdane, C. Marcandella, A. Boukenter, S. Quenard, N. Authier - Feasibility of radiation dosimetry with phosphorus-doped optical fibers in the ultraviolet and visible domain - *Journal of Non-Crystalline Solids*
- [56] M.C. Paul, R. Sen, S.K. Bhadra, M. Pal, P.P. Giri, K. Dasgupta, T.K. Bandyopadhyay, D. Bohra, P.K. Bhatnagar - Gamma ray radiation induced absorption in Ti doped single mode optical fibres at low dose levels - *Optical Materials* 29 (2007) 738–745
-

- [57] Dan Sporea, Adelina Sporea, Constantin Oproiu - Effects of hydrogen loading on optical attenuation of gamma-irradiated UV fibers - Journal of Nuclear Materials
- [58] O’Keeffe, S.; Fernandez Fernandez, A.; Fitzpatrick, C.; Brichard, B. & Lewis, E. (2007). Real-time gamma dosimetry using PMMA optical fibres for applications in the sterilization industry, Meas. Sci. Technol., Vol. 18, No. 10, (2007), (3171-3176)
- [59] O’Keeffe, S. & Lewis, E. (2009). Polymer optical fibre for in situ monitoring of gamma radiation processes, Intl. J. Smart Sensing and Intelligent Systems, VOL. 2, No. 3, (September 2009), (490-502)
- [60] Rishi Pal Chahal, Suman Mahendia, A.K. Tomar, Shyam Kumar- Gamma-Irradiated PVA/Ag nanocomposite films: Materials for optical applications - Journal of Alloys and Compounds
- [61] O. Kongwut, A. Kornduangkeaw, N. Jangsawang, Satreerat K. Hodak - Influence of gamma irradiation on the refractive index of Fe-doped barium titanate thin films - Thin Solid Films
- [62] Henning Henschel, Stefan K. Hoeffgen, Member, IEEE, Katerina Krebber, Jochen Kuhnhenh, Udo Weinand - Influence of Fiber Composition and Grating Fabrication on the Radiation Sensitivity of Fiber Bragg Gratings
- [63] Radiation sensitivity of Bragg gratings written with femtosecond IR lasers - Dan Grobnica, Henning Henschel, Stefan K. Hoeffgen, Jochen Kuhnhenh, Stephen J. Mihailov, Udo Weinand
- [64] Katerina Krebber, Henning Henschel, Udo Weinand - Fibre Bragg gratings as high dose radiation sensors?
- [65] H. Schonbacher, M. Tavlet - Radiation Effects on Structural Materials for High Energy Particle Accelerator and Detectors
-

- [66] S.J. Zinkle, R.L. Sindelar, Journal of Nuclear Materials 155–157 (1988) 1196
- [67] Agrawal, R. Bajpai & S. C. Datt Hardening Induced by Gamma Irradiation in Poly(methyl methacrylate): Poly(chlorotrifluoroethylene) BlendsP
- [68] Y. Tabata, Y. Katsumura - Fast neutron irradiation effects on polymers - polyethylene, ethylene propylene rubber and tetrafluoroethylene propylene copolymer - Journal of Nuclear Materials 133&134 (1985) 781-784
- [69] Nicolaie Moldovan - Deformation and stress in PMMA during hard X-ray exposure for deep lithography
- [70] H.N. Subrahmanyam, S.V. Subramanyam - Thermal expansion of irradiated poly(methyl methacrylate) - Polymer Volume 28, Issue 8, July 1987, Pages 1331–1333
-